**US Army Corps
of Engineers**
Waterways Experiment
Station

MAC3D: Numerical Model for Reservoir Hydrodynamics with Application to Bubble Diffusers

by Robert S. Bernard

Approved For Public Release; Distribution Is Unlimited

19980901 007

Prepared for U.S. Army Engineer District, Chicago

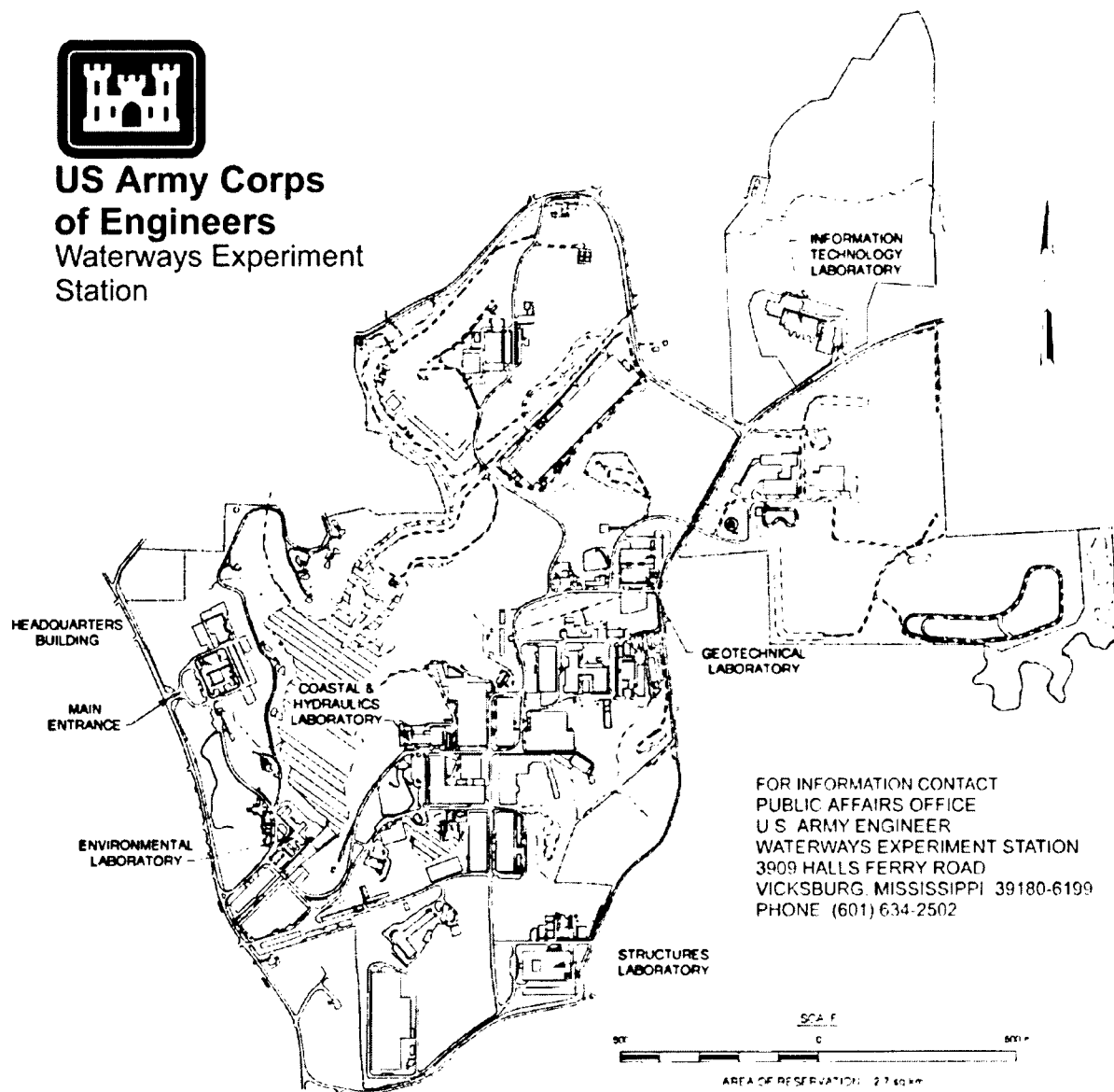# MAC3D: Numerical Model for Reservoir Hydrodynamics with Application to Bubble Diffusers

by Robert S. Bernard

U.S. Army Corps of Engineers
Waterways Experiment Station
3909 Halls Ferry Road
Vicksburg, MS 39180-6199

Final report

Prepared for U.S. Army Engineer District, Chicago
Chicago, IL 60606-7206

US Army Corps
of Engineers
Waterways Experiment
Station

HEADQUARTERS
BUILDING

MAIN
ENTRANCE

COASTAL &
HYDRAULICS
LABORATORY

ENVIRONMENTAL
LABORATORY

INFORMATION
TECHNOLOGY
LABORATORY

GEOTECHNICAL
LABORATORY

STRUCTURES
LABORATORY

FOR INFORMATION CONTACT
PUBLIC AFFAIRS OFFICE
U S ARMY ENGINEER
WATERWAYS EXPERIMENT STATION
3909 HALLS FERRY ROAD
VICKSBURG. MISSISSIPPI 39180-6199
PHONE (601) 634-2502

SCALE

AREA OF RESERVATION 2 7 sq km

Contents

Preface

The report herein discusses research and development conducted from October 1994 through March 1998 by personnel of the Fisheries and Reservoir Hydrodynamics Branch (FRHB), Rivers and Structures Division (RSD), Coastal and Hydraulics Laboratory (CHL), U.S. Army Engineer Waterways Experiment Station (WES). Funding was provided by the U.S. Army Engineer District, Chicago.

Dr. Robert S. Bernard, FRHB, prepared this report under the general supervision of Dr. James R. Houston, Director, CHL; Dr. Phil G. Combs, Chief, RSD; and Mr. John F. George, Chief, FRHB. Technical counsel was provided by Messrs. Michael L. Schneider and Steven C. Wilhelms, FRHB; by Professor Dr. John S. Gulliver, University of Minnesota; and by Dr. Henry T. Falvey, Conifer, CO. Technical assistance was provided by Ms. Laurin I. Yates and Mr. Calvin Buie, Jr., FRHB; and by Mr. Charles W. Downer, Watershed Systems Group, CHL.

Technical monitors for the Chicago District were Mr. Tom Fogarty and Mrs. Linda Sorn. At the time of publication of this report, Dr. Robert W. Whalin was Director of WES, and COL Robin R. Cababa, EN, was Commander.

Conversion Factors, Non-SI to SI Units of Measurement

Non-SI units of measurement used in this report can be converted to SI units as follows:

Multiply	By	To Obtain
cubic feet	0.02832	cubic meters
feet	0.30480	meters
square feet	0.09290	square meters

1 Introduction

Background

This report should be regarded as companion and sequel to an earlier report (Bernard 1995),[1] which documents the preliminary development of the MAC3D numerical model. The latter embodies a general-purpose, three-dimensional (3-D), numerical flow-solver for incompressible fluids with fixed boundaries. Small changes in density are allowed in response to temperature variations, but only insofar as they affect buoyancy. Otherwise, the flow is assumed to be mechanically incompressible, and density is unaffected by pressure. Geometric flexibility is achieved by finite-volume discretion on structured, multiblock, curvilinear grids.

Initially the purpose of MAC3D was only to simulate incompressible flow in situations where vertical acceleration might be strong enough to invalidate the hydrostatic assumption commonly used for pressure in shallow water. Unlike hydrostatic flow models, MAC3D solves a Poisson equation (derived from the mass- and momentum-conservation equations) for the deviation of the pressure from its hydrostatic value. With the help of a k-ϵ turbulence model (Launder and Spalding 1974), the original MAC3D code did a fair job of reproducing subcritical flow in open channels and confined flow inside hydraulic structures (Bernard 1996).

During its preliminary validation, MAC3D exhibited two practical short-comings, owing to its reliance on a MacCormack scheme (MacCormack 1969; Bernard 1992, 1995) for solving the incompressible flow equations. First, the explicit nature of the scheme severely limited the allowable size of the discrete time-step for a developing flow. Second, the MacCormack scheme proved unstable for grids with disparate spacing and very large grid-cell aspect ratios (cell length divided by cell width or depth). Since disparate spacing and large aspect ratios are unavoidable for broad reservoirs, it was necessary to incorporate a more robust numerical algorithm for the flow solution. Accordingly, the explicit MacCormack scheme was replaced with an implicit upwind scheme that improves stability overall, while reducing execution time by a factor of 5 to 10.

---

[1] This report, WES Technical Report HL-95-9, will henceforth be referred to as "the 1995 report."

With regard to modeling bubble diffusers, the impetus for extending the MAC3D code beyond its original capabilities was provided by the sponsoring agency. In support of its effort to design an aeration system for the proposed McCook Reservoir, the Chicago District needed a practical capability for numerically simulating the influence of submerged diffusers on reservoir flow and aeration. This demanded that bub! plumes be incorporated into the vertical equation of motion in MAC3D and that new equations be added for the transfer and transport of dissolved gas. The end result was a numerical hydro-dynamic model that reliably predicts diffuser-driven velocities (within a factor of two) for unstratified or weakly stratified water with airflow rates up to 50 cu ft per minute (cfm)[1] and depths up to 40 ft. Dissolved-oxygen transport rates are well predicted for experiments in small tanks, in which mixing is so rapid that the concentration is nearly uniform. Transport rates are also well predicted for elapsed times of a few hours in large reservoirs with weak stratification, but not with strong stratification. Validation of the predicted long-term transport rates in weakly stratified reservoirs awaits further experiments conducted for much longer times.

Purpose and Scope

This report documents the extension and validation of the MAC3D numerical flow model for application to reservoirs with submerged bubble diffusers. Chapter 2 discusses the updated numerical solution scheme, the reformulation of the boundary conditions, and the major differences between present and previous numerical algorithms. Chapter 3 outlines modifications made to account for the buoyancy created by a bubble plume, the rate of dissolved-gas transfer from the bubbles to the surrounding water, and the rate of transport of the dissolved gas by the flow itself. Chapter 4 compares MAC3D predictions for velocity and gas transfer with experimental data taken for unstratified conditions with coarse- and fine-bubble diffusers in a cylindrical tank, 25 ft in diameter and 10 to 31 ft deep. Chapter 5 compares a priori velocity predictions with data obtained for coarse-bubble diffusers in a weakly stratified, flooded rock quarry, 40 ft deep and 800 ft wide. Chapter 6 compares a posteriori gas-transfer predictions for the same quarry with data taken for both weakly and strongly stratified conditions, and Chapter 7 offers conclusions and recommendations for further work.

---

[1] A table of factors for converting non-SI units of measurements to SI units is presented on page vi.

2 Numerical Considerations

Background

The original MAC3D code (Bernard 1995) and its two-dimensional (2-D) predecessor, the STREMR code (Bernard 1993), employed an explicit predictor-corrector scheme developed by MacCormack (1969) to compute the transport of mass and momentum due to advection. Details are given for 3-D curvilinear grids in the 1995 report, but a one-dimensional (1-D) example will serve for discussion here. Consider the following 1-D equation for transport by advection:

$$\frac{\partial \phi}{\partial t} + V \frac{\partial \phi}{\partial \eta} = 0 \tag{1}$$

where

ϕ = any transported quantity

t = time

V = transporting velocity in the η-direction

Let the time and space increments be Δt and $\Delta \eta$, respectively; and let the integer subscript j indicate discrete values ϕ_j defined at stations $j-1, j, j+1$, etc., along the η-axis. Furthermore, let the integer superscript n indicate discrete values of ϕ at time levels $n-1, n, n+1$, etc. In the predictor step of the MacCormack scheme, a provisional time-increment $\Delta\phi^*$ might be computed using a forward difference approximation for the spatial derivative; i.e.,

$$\Delta\phi_j^* + C\,[\,\phi_{j+1}^n - \phi_j^n\,] = 0 \tag{2}$$

with the Courant number C given by

$$C = V \frac{\Delta t}{\Delta \eta} \tag{3}$$

This would yield a provisional new value for ϕ_j,

$$\phi_j^{\cdot} = \phi_j^{n} + \Delta\phi_j^{\cdot} \qquad (4)$$

In the corrector step of the MacCormack scheme, a second provisional time-increment $\Delta\phi^{\cdot\cdot}$ would then be computed using a backward difference approximation for the spatial derivative:

$$\Delta\phi_j^{\cdot\cdot} + C[\phi_j^{\cdot} - \phi_{j-1}^{\cdot}] = 0 \qquad (5)$$

The final increment $\Delta\phi^{n}$ would be taken as the average of the two provisional increments,

$$\Delta\phi_j^{n} = \frac{1}{2}[\Delta\phi_j^{\cdot} + \Delta\phi_j^{\cdot\cdot}] \qquad (6)$$

with the new value for ϕ then given by

$$\phi_j^{n+1} = \phi_j^{n} + \Delta\phi_j^{n} \qquad (7)$$

This scheme is accurate for $C \le 1$ and stable for $0 \le C \le 1$, but it exhibits numerical oscillations when $C \ll 1$. For the Euler momentum equation, in which C is a function of ϕ, these oscillations can lead to instability. To use the MacCormack scheme for numerical flow simulation in general, one must avoid situations in which $C \ll 1$, unless there is sufficient viscosity to limit the growth of spurious oscillations.

Explicit Upwind Scheme

Reservoir flow simulations often involve grids with disparate spacing and large grid-cell aspect ratios, for which regions with $C \ll 1$ are unavoidable. To eliminate the need for artificially adding viscosity to the govern'·ng equations, the MacCormack scheme for advection has been directly replaced b. a three-point upwind scheme in MAC3D. Using the upwind scheme in the 1-D example, the increment of ϕ, for $C > 0$, would be computed from

$$\Delta\phi_j^{\cdot} - \frac{C}{2}[3\phi_j^{n} - 4\phi_{j-1} + \phi_{j-2}^{n}] = 0 \qquad (8)$$

and otherwise, for $C < 0$, from

$$\Delta\phi_j{}^n - \frac{C}{2}[\phi_{j+2}{}^n - 4\phi_{j+1}{}^n + 3\phi_j{}^n] = 0 \tag{9}$$

The MacCormack scheme and the three-point scheme (as presented) are both explicit schemes, because they compute the spatial derivative of ϕ from information existing at time level n, but not at time level $n+1$. In contrast, an implicit scheme would use information from two (or more) time levels for computing spatial derivatives. Although better behaved than the MacCormack scheme for $C \ll 1$, the three-point scheme is always unstable for $C > 2/3$ and sometimes unstable even at lesser Courant numbers. To extend the Courant limit and to ensure stability within that limit, one must include an implicit contribution (from time level $n+1$) in the equation for $\Delta\phi$.

Implicit Upwind Scheme

Viscosity helps to stabilize explicit flow simulations when $C \ll 1$, but it can also hamper progress by reducing the allowable size of the time-step. Consider, for example, the 1-D advection-diffusion equation (ADE):

$$\frac{\partial\phi}{\partial t} + V\frac{\partial\phi}{\partial\eta} = \nu\frac{\partial^2\phi}{\partial\eta^2} \tag{10}$$

Here ν represents the kinematic viscosity (or diffusivity), and the other quantities are the same as in the 1-D advection equation. Using three-point upwinding (with $V > 0$) for the advective term and central differencing for the viscous term, the explicit ADE for $\Delta\phi^n$ becomes

$$\Delta\phi_j{}^n + \frac{C}{2}[3\phi_j{}^n - 4\phi_{j-1}{}^n + \phi_{j-2}{}^n] = \Gamma[\phi_{j+1}{}^n - 2\phi_j{}^n + \phi_{j-1}{}^n] \tag{11}$$

where C is the Courant number as before, and Γ is the nondimensional viscosity, defined by

$$\Gamma = \frac{\nu\,\Delta t}{\Delta\eta^2} \tag{12}$$

As a rough rule of thumb, one can expect the explicit ADE to be stable as long as

$$\frac{3}{2}C + 2\Gamma < 1 \tag{13}$$

This ADE stability rule depends on both C and Γ, but the advective contribution is inversely proportional to $\Delta\eta$, while the viscous contribution is inversely proportional to $\Delta\eta^2$. In other words, the time-step allowed by the advective term decreases with the grid spacing, but the time-step allowed by the viscous term decreases with the square of the grid spacing. For turbulent flow simulations, where diffusion can dominate advection (locally) by an order of magnitude or more, the viscous time-step limit may be far more confining than the advective (Courant) limit. Thus, in a numerical flow model like MAC3D, it is wise to include im·licit contributions from both the viscous and advective terms. For MAC3D >articular, this is done by mixing the two time levels, n and $n+1$, with a coupling parameter $0 \le \lambda \le 1$. With this two-level coupling, the implicit form of the example ADE becomes

$$\frac{\partial\phi}{\partial t} + V\left(\lambda\frac{\partial\phi^{n \cdot 1}}{\partial\eta} + (1-\lambda)\frac{\partial\phi^{n}}{\partial\eta}\right) = \nu\left(\lambda\frac{\partial^2\phi^{n \cdot 1}}{\partial\eta^2} + (1-\lambda)\frac{\partial^2\phi^{n}}{\partial\eta^2}\right) \qquad (14)$$

Expressed in Δ-form, the same two-level implicit ADE is given by

$$\frac{\Delta\phi}{\Delta t} + V\left(\lambda\frac{\partial}{\partial\eta}\Delta\phi + \frac{\partial\phi^{n}}{\partial\eta}\right) = \nu\left(\lambda\frac{\partial^2}{\partial\eta^2}\Delta\phi + \frac{\partial^2\phi^{n}}{\partial\eta^2}\right) \qquad (15)$$

which can be rewritten as

$$\Delta\phi + \lambda\Delta t\left(V\frac{\partial}{\partial\eta} - \nu\frac{\partial^2}{\partial\eta^2}\right)\Delta\phi = \Delta\phi^{n} \qquad (16)$$

where $\Delta\phi^{n}$ is the increment of ϕ obtained from the explicit ADE given by Equation 11. On the left side of the implicit ADE, the second derivative $\partial^2(\Delta\phi)/\partial\eta^2$ is discretized with central differencing, just like $\partial^2\phi^{n}/\partial\eta^2$ in the explicit ADE. For convenience and economy in MAC3D, however, the first derivative $\partial(\Delta\phi)/\partial\eta$ is discretized with two-point upwinding instead of three-point upwinding. As pointed out by MacCormack (1982), the explicit right-hand side ($\Delta\phi^{n}$) embodies all the physics, and the steady-state solution ($\Delta\phi \cdot 0$) should be independent of the approximations used for derivatives of $\Delta\phi$ on the left-hand side. Moreover, as long as $\lambda \ll 1$, the transient solution can be adequately represented as well. A default value $\lambda = 0.1$ is now used in MAC3D, which tolerates Courant numbers in the range $0 \le C \le 2$ and nondimensional viscosities roughly in the range $0 \le \Gamma \le 10$.

The explicit upwind scheme computes $\Delta\phi^{n}$ in a single step, and the implicit scheme then uses this quantity as an initial guess, upon which it iterates to obtain $\Delta\phi$. Since iteration can involve considerable extra work, and since the aim here is only to achieve numerical stability, it is expedient to use the simplest viable iteration procedure, with as few iterations as possible. For the time being,

MAC3D employs Jacobi iteration (Roache 1972) for the implicit solver, with a default limit of 10 iterations per time-step. Although this more than doubles the total work per time-step, the increase in size of the allowable time-step can result in computational speed-up factors of 5 to 10 over the explicit scheme.

Velocity Interpolation on MAC Grids

The MAC3D acronym comes not from the previously used MacCormack scheme, but from the so-called marker-and-cell (MAC) grids that are employed for discretizing the flow and transport equations. With MAC grids, discrete scalar quantities like pressure and temperature are formally defined only at the cell centers, while discrete velocity components are formally defined only on the cell faces. Moreover, only one velocity component normal to each face is defined on that face. The most convenient locations for computing velocity increments are the cell centers; but this demands additional closure relations that define cell-centered components in terms of face-centered components and face-centered increments in terms of cell-centered increments. The following 1-D example illustrates the closure relations now used in MAC3D.

Let the integer locations $j-1$, j, $j+1$ represent cell faces along the η-axis, and let the half-integer locations $j-\frac{1}{2}$, $j+\frac{1}{2}$ represent cell centers. The discrete velocities v_j are formally defined only on cell faces; but when they are needed at the cell centers, they are computed by simple averaging:

$$v_{j\pm1/2} = \frac{1}{2}[v_j + v_{j\pm1}] \tag{17}$$

Velocity increments $\Delta v_{j\pm\frac{1}{2}}$ are formally defined only at the cell centers, but they are projected onto the cell faces by fourth-order interpolation:

$$\Delta v_j = \frac{1}{16}[9\Delta v_{j+1/2} - \Delta v_{j+3/2} + 9\Delta v_{j-1/2} - \Delta v_{j-3/2}] \tag{18}$$

These interpolated increments are the ones that are used to advance the face-centered velocities from one time-step to the next.

Application of the Pressure Gradient

In the same manner discussed in the 1995 report, the updated pressure gradient is omitted from the explicit (cell-centered) momentum equation, only to be computed and imposed after the new (cell-centered) velocity increments have been projected onto the cell faces. In effect, the pressure gradient lags the velocity by one time-step, and its application has to be modified slightly for the

implicit flow-solver. For discussion, consider the 1-D Euler equation with unit density,

$$\frac{\partial v}{\partial t} + v\frac{\partial v}{\partial \eta} + \frac{\partial p}{\partial \eta} = 0 \tag{19}$$

in which p represents the kinematic pressure (i.e., pressure divided by density), and the remaining quantities are the same as before. Expressed in linearized Δ-form for velocity, the implicit Euler equation becomes

$$\frac{\Delta v}{\Delta t} + v^n\frac{\partial}{\partial \eta}[v^n + \lambda\Delta v] + \frac{\partial p}{\partial \eta} = 0 \tag{20}$$

Introducing the new variable,

$$\Delta v^{\cdot} = \Delta v + \frac{\partial p}{\partial \eta}\Delta t \tag{21}$$

it follows that

$$\frac{\Delta v}{\Delta t} + v^n\frac{\partial}{\partial \eta}\left(v^n - \lambda\Delta t\frac{\partial p}{\partial \eta} + \lambda\Delta v^{\cdot}\right) = 0 \tag{22}$$

Now setting $p \approx p^{n-1}$, the approximate Δ-form for the implicit Euler equation can be written as

$$\frac{\Delta v^{\cdot}}{\Delta t} + \lambda v^n\frac{\partial}{\partial \eta}\Delta v^{\cdot} \approx -v^n\frac{\partial}{\partial \eta}\left(v^n - \lambda\Delta t\frac{\partial p^{n-1}}{\partial \eta}\right) \tag{23}$$

This allows the old pressure p^{n-1} from the previous time level to be used in the iterative solution for $\Delta v^{\cdot}$, after which a new pressure p^n can be found that yields the mass-conserving velocity increment Δv from the relation,

$$\Delta v = \Delta v^{\cdot} - \frac{\partial p^n}{\partial \eta}\Delta t \tag{24}$$

For incompressible flow in two or three dimensions, the pressure p^n has to be obtained from the iterative solution of a discrete Poisson equation, which is discussed in detail in the 1995 report.

Rough-Wall Shear Stress

MAC3D still offers the Manning coefficient as an optional parameter for adjusting shear stress on no-slip (sidewall and bottom) boundaries, but the default shear stress is now taken to be that given by the conventional Law of the Wall for rough walls. That is, for a fluid of unit density, the shear stress τ_{wall} along a no-slip boundary is defined as

$$\tau_{wall} = u_*^2 \tag{25}$$

and the friction velocity u_* is obtained from the relation,

$$u_* = \frac{\kappa u(\delta)}{ln\left(\dfrac{E u_* \delta}{v_0}\right)} \tag{26}$$

where

$u(\delta)$ = tangential velocity u at a normal distance δ from wall

$\kappa \approx 0.418$ = Von Karman's constant

v_0 = molecular viscosity

Note that the coefficient E is given approximately by $E \approx 9.96$ for smooth walls and by $E \approx 0.72$ for rough walls (Kirkgöz 1989).

Turbulence Model

Unless directed otherwise, MAC3D uses the standard k-ϵ turbulence model of Launder and Spalding (1974) by default.[1] This requires the numerical solution of production-and-transport equations for the turbulence energy k and its dissipation rate ϵ. In contrast with other flow variables, the code uses two-point upwinding in the implicit and explicit solutions for k and ϵ. The latter quantities are used to compute the eddy viscosity,

$$v = C_v \frac{k^2}{\epsilon} \tag{27}$$

---

[1] The adjustment for low velocity and high strain rate, which was proposed in the 1995 report as a remedy for turbulence overproduction in recirculating flow, is now optional.

with the standard coefficient $C_v = 0.09$.

Along slip and no-slip walls, the original MAC3D code imposed vanishing normal derivatives for k and ϵ, such that

$$\frac{\partial k}{\partial \delta} = \frac{\partial \epsilon}{\partial \delta} \equiv 0 \tag{28}$$

In the present code, however, the vanishing normal derivative for ϵ is no longer used as a boundary condition for no-slip walls. Instead, for all grid cells adjacent to no-slip walls, the cell-averaged value of ϵ is now defined by the equilibrium relation between k and ϵ,

$$\epsilon = \frac{C_v^{3/4} k^{3/2}}{\kappa \delta_C} \tag{29}$$

where δ_C is the cell thickness (grid spacing) normal to the wall.

3 Bubble Plumes and Gas Transfer

Background

One might suppose that numerical models should simulate physical processes by solving only equations derived from basic principles such as those for conservation of mass, momentum, and energy (in its various forms). In practice, however, these equations are often so complex as to render modeling efforts intractable without empirical simplification. The flow associated with a bubble diffuser is a case in point. Calculating the turbulent flow about a single rising bubble is a problem that taxes the capabilities of existing computers. For the myriad bubbles released by a typical diffuser/aerator, the fully coupled flow problem is effectively insoluble at the bubble scale. A practical alternative is to parameterize the interaction between the bubbles and the water and then resolve the flow and transport on a scale much larger than the bubble diameter.

The approach taken here is to treat a bubble plume as a cylindrical column of water in which there is an upward buoyant force (created by the bubbles) and a transfer of dissolved gas directly from the bubbles to the water (or vice versa). When these two mechanisms are incorporated into a numerical flow model and validated with gas-transfer data for small tanks, the numerical model should then be able to predict diffuser performance in much larger volumes of water.

Bubble-Plume Buoyancy

A bubble plume is idealized here as a vertical cylindrical column in which rising bubbles displace surrounding water to create an upward acceleration and ultimately a recirculating flow. This buoyant acceleration is the local ratio of bubble volume to water volume in the plume, multiplied by the acceleration g due to gravity (32.2 ft^2/sec). Its magnitude is given by

$$g_{plume} = \frac{g\,Q_{air}}{A_{plume}\,w_{rise}\left(1 + \dfrac{h}{h_{atm}}\right)}$$

(30)

where

Q_{air} = airflow rate through diffuser (under standard conditions)

A_{plume} = cross-sectional area of bubble plume

w_{rise} = absolute rise velocity of the bubbles

h = vertical distance from surface

h_{atm} = depth of water equivalent to one atmosphere (33.9 ft)

The quantity $1 + h/h_{atm}$ accounts for the local (compressive) reduction in bubble volume with increasing depth.

The absolute rise velocity is the sum of the vertical flow velocity w and the relative rise velocity of the bubbles, w_{rel}. The latter is taken to be 0.82 fps, which is a median value (between 0.49 and 1.15 fps) for individual bubbles from 1 to 25 mm in diameter (Clift, Grace, and Weber 1978). Note that the ratio of the relative rise velocity, w_{rel}, to the average flow velocity, w_{ave}, influences the exponent in the scaling relation between local flow velocity and airflow rate. Thus, from numerical experiments one finds that if $w_{rel} <<< w_{ave}$, then the flow velocity increases with $Q_{air}^{1/3}$, but if $w_{rel} >>> w_{ave}$, then the flow velocity increases with $Q_{air}^{1/2}$. For airflow rates up to 60 standard cubic feet per minute (scfm) and depths up to 50 ft, however, w_{rel} and w_{ave} are close enough in magnitude that the exponent is roughly 2/5.

Computed velocities are sufficiently insensitive to the cross-sectional area of the bubble plume that a factor-of-three change in A_{plume} produces less than a 10-percent change in velocity. This is fortunate, because A_{plume} is hard to estimate with accuracy better than a factor of two. The most important quantity appears to be the total force imposed by the plume, not its precise distribution.

Gas Transfer and Transport

Inside a bubble plume, the rate of transfer of dissolved gas to or from the water is proportional to the difference between the local concentration C and its local saturation value C_{sat}, in units of mass/volume. When this is combined with transport by the flow (advection and diffusion), the governing equation for the dissolved gas becomes

$$\frac{\partial C}{\partial t} + \boldsymbol{u}\cdot\nabla C = \frac{K_{plume}}{A_{plume}}[C_{sat} - C] - D_{gas} + \nabla\cdot[\nu_D\nabla C] \qquad (31)$$

where

t = time

∇ = gradient operator

K_{plume} = depth-averaged transfer coefficient for plume (in units of area/time)

A_{plume} = assumed cross-sectional area of cylindrical bubble column

D_{gas} = dissolved-gas depletion rate (chemical or biological demand)

ν_D = turbulent diffusion coefficient for dissolved gas (proportional to eddy viscosity ν)

Note that K_{plume} has to be inferred directly from experiments for a given bubble diffuser, but A_{plume} need only approximate the average cross section of a real plume within a factor of three or so. In any case, K_{plume} is nonzero inside the bubble plume and zero elsewhere.

Gas flux through the free surface into the water is given by $K_{LS}[C_{sat} - C]$. The coefficient K_{LS} has units of length/time, and it is computed in MAC3D via the relation,

$$K_{LS} \approx K_{surf}|u| \qquad (32)$$

where u is the horizontal flow velocity along the surface, and the empirical coefficient $K_{surf} \approx 0.00185$ was chosen to match computed surface-exchange rates with those observed in tank experiments conducted by Wilhelms and Martin (1992). The linear dependence on velocity was suggested by J. Gulliver[1] based on the work of Broecker, Petermann, and Siems (1978).

---

[1] Personal Communication, February 1996, John S. Gulliver, University of Minnesota, Minneapolis, MN.

4 Model Predictions for a Cylindrical Tank

Background

In 1995, laboratory experiments[1,2] were conducted by engineers and technicians from the U.S. Army Engineer Waterways Experiment Station (WES) and the U.S. Geological Survey (USGS) to test the capabilities of two bubble diffusers. One of these was a fine diffuser, capable of delivering an airflow rate of 6.5 scfm; and the other, a coarse diffuser, capable of delivering 60 scfm. The experiments were conducted in a 25-ft-diam cylindrical tank with water depths ranging from 10 to 31.3 ft. The aims were first, to determine gas-transfer coefficients for each diffuser, and second, to measure diffuser-driven flow velocities.

Velocity measurements were made with an acoustic doppler velocimeter (ADV) at the rate of one per second. These revealed the flow to be unsteady but quasi-periodic over intervals of several seconds, as shown by Figure 1 (prepared by USGS). This unsteadiness may arise from bubble-to-bubble interactions in the plume or perhaps from the intermittency with which the diffuser releases individual bubbles. Whatever the case, for comparison with steady-state model predictions, the ADV data were time-averaged over the entire measurement interval of several minutes.

The numerical simulations were all started from rest (no initial flow), using a cylindrical grid (Figure 2) with a radial spacing of 0.5 ft and a circumferential spacing of 15 deg. Vertical spacing varied between 0.5 and 1.0 ft, depending on the total water depth. In the experiments, the bubble diffusers were placed at the center of the tank, 3 ft from the bottom. In the MAC3D simulations, the model

---

[1] Unpublished gas-transfer measurements provided by Charles W. Downer, Laurin I. Yates, and Calvin Buie, Jr., September 1995, U.S. Army Engineer Waterways Experiment Station, Vicksburg, MS.

[2] Unpublished velocity measurements provided by Gary P. Johnson, November 1995, U.S. Geological Survey (USGS), U.S. Department of the Interior, Urbana, IL.

bubble column extended vertically from this location to the water surface, with a fixed diameter of 3.0 ft. The standard k-ϵ turbulence model was activated in all cases, and the tank bottom and sidewalls were treated as no-slip boundaries. The parameters w_{rel} and K_{surf} uniformly retained their previously assigned values, but a constant of proportionality had to be inferred for K_{plume} from one of the gas-transfer experiments. Thereafter, its value was set in proportion to the diffuser airflow rate Q_{air}. Computed velocities reached steady state within 10 to 15 min (real-time), but the ever-rising dissolved-gas concentrations took at least twice as long to homogenize within ±0.25 mg/L about the instantaneous mean.

Velocity Predictions for 10-ft Depth

Figure 3 shows grid detail and data stations for experiments conducted with a total water depth of 10 ft in the 25-ft tank. (Here the number assigned to each station represents the radial distance from the center of the tank.) Computed velocity vectors are presented in Figure 4 for a MAC3D simulation executed with Q_{air} = 35.5 scfm. Subsequent figures (5 through 8) compare predicted velocity magnitudes with coarse-diffuser data for 35.5 scfm and with rescaled fine-diffuser data for 0.88 scfm. The latter were scaled up to 35.5 scfm by assuming that velocity increases with the 2/5 power of Q_{air}. Except for Station 11, the agreement between simulation and experiment is fairly good.

Velocity Predictions for 31-ft Depth

Figure 9 shows grid detail and data stations for experiments conducted with a total water depth of 31.3 ft in the 25-ft tank. (Again the number assigned to each station represents the radial distance from the center of the tank.) Computed velocity vectors are presented in Figure 10 for a MAC3D simulation executed with Q_{air} = 30.5 scfm. Subsequent figures (11 through 19) compare predicted velocity magnitudes with coarse-diffuser data for 30.5 scfm, with rescaled coarse-diffuser data for 13.7 scfm, and with rescaled fine-diffuser data for 1.2 and 6.5 scfm. As before, experimental data were scaled up to 30.5 scfm by assuming that velocity increases with the 2/5 power of Q_{air}.

The overall agreement between simulation and experiment is not quite as good for this depth as it was for the 10-ft case. At Stations 3 and 5, the correlation between the two is very good, but the disparity at the other stations may reach a factor of two or more. For the most part, however, the accuracy of prediction is a factor of two or better.

Gas-Transfer Predictions

Figure 20 compares predicted and observed K_LA values for the coarse-diffuser gas-transfer experiments, where K_LA is the total exchange coefficient for dissolved oxygen, defined by

$$K_L A = -\frac{1}{t} \ln\left(\frac{C_{eq} - C}{C_{eq} - C_i} \right)$$ (33)

and

C_{eq} = equilibrium concentration

C_i = initial concentration

t = elapsed time

The experiments were conducted for three depths and four airflow rates. One of these (11-ft total depth and 60-scfm airflow) was used as a benchmark for assigning a value to K_{plume}, after which all the remaining experiments were simulated with K_{plume} proportional to Q_{air}. The initial concentration was zero in each case, and $K_L A$ was computed using the volume-averaged concentration after 1 hr. The entire volume was fully mixed within 1 hr in all cases, at which time the computed variation in C was less than ± 0.25 mg/L throughout the tank. Figure 21 compares predicted and observed equilibrium concentrations with the saturation concentration at the bottom of the tank.

The agreement between predicted and observed values for $K_L A$ does not confirm the intended ability of MAC3D to forecast dissolved-gas transfer and transport in reservoirs. It does lend support, however, for the proposed linear relation between flow velocity and surface transfer. Other plausible surface-transfer formulas (e.g., square-root and quadratic relations) produced erroneous variations of $K_L A$ with Q_{air} and total depth.

5   Model Predictions for a Flooded Quarry

Background

In 1996, field tests were conducted with the (previously described) coarse diffuser at Egan Quarry, Illinois, by engineers and technicians from USGS.[1] Egan Quarry is a flooded, abandoned rock quarry, roughly 1,100 ft long and 800 ft wide. With a nominal water depth of about 40 ft, it offered sufficient volume for determining the breadth and intensity of flow created by configurations of one, two, and four diffusers in an extended body of water. By the same token, it provided a challenging setting in which to test the predictions of the MAC3D numerical model.

The diffusers were placed near the middle of the quarry, 2 ft off the bottom, and allowed to run long enough to break up most of the stratification in the near field. They were then turned off long enough for all diffuser-induced motion to die out, after which they were restarted and allowed to run for several hours. At various times and data stations, ADV velocity measurements were made at the rate of one per second. These were time-averaged over the entire measurement interval for comparison with MAC3D predictions. Except for one series of single-diffuser tests with 23.9 scfm, all the experiments were conducted with airflow rates of 46 scfm.

In the numerical simulations, no attempt was made to reproduce the entire volume of the quarry or even its gently varying bottom topography. Instead, the computational grids were all generated with uniform depths of 40 ft and with far-field boundaries 250 ft from the diffusers. This produced computational regions large enough that the far boundaries had negligible influence on the flow created by the diffusers.

The a priori numerical simulations discussed in this chapter were all started from rest, assuming no stratification and no initial dissolved oxygen. The

---

[1] Unpublished velocity measurements provided by Nancy J. Hornewer, April 1997, U.S. Geological Survey (USGS), U.S. Department of the Interior, Urbana, IL.

vertical grid spacing was 1.0 ft everywhere, but the horizontal spacing varied with position, generally becoming coarser with increasing distance from the diffusers. The model bubble column was assigned a uniform diameter of 3.0 ft, extending all the way to the surface from a position 2 ft above the bottom. The standard k-ϵ turbulence model was activated in all cases, with the bottom treated as a no-slip boundary, and the far-field wall as a slip boundary. The parameters w_{rel} and K_{surf} retained their previously assigned values, and the same constant of proportionality was used for K_{plume} as in the WES tank simulations discussed in Chapter 4, with the value of K_{plume} fixed in proportion to the diffuser airflow rate Q_{air}. Each numerical simulation was executed for 3 hr (real-time), and computed results were stored at 1-hr intervals for velocity and dissolved oxygen. Since initial conditions used for the latter were completely (and unrealistically) anaerobic, the a priori predictions for gas transfer can be regarded only as rough indicators of diffuser performance under field conditions.

Single Diffuser

Figure 22 (prepared by USGS) shows the layout of experimental data stations for the single-diffuser tests, which were conducted with airflow rates of 23.9 and 46 scfm. Here the numerical labels indicate only the order in which the ADV measurements were taken, and they have nothing to do with distance from the diffuser. A cylindrical grid with a diameter of 500 ft was used for the MAC3D simulations. Figure 23 offers a plan view of the entire grid, while Figure 24 presents a closer, quarter-plane view showing computational data stations and grid detail near the diffuser itself.

Figures 25 through 28 compare MAC3D predictions for velocity magnitude with experimental data for 46 scfm and with rescaled data for 23.9 scfm (using the 2/5 power of the airflow rate). Figure 29 offers a plot of background velocities measured under quiescent conditions with no airflow through the diffuser. The relative agreement between computed and observed velocities is comparable here with that for the 31-ft-deep tank (Chapter 4). In the far field (Stations 3, 6), the diffuser-driven velocities hardly exceed the background velocities at all. The same can be said for the lower 20 ft at the intermediate location (Stations 2, 5). Only in the near field (Stations 1, 4, and 7) do the predicted and observed velocities rise well above background over the entire water depth.

Figure 30 compares gray-scale maps of predicted dissolved-oxygen concentration at elapsed intervals of 1, 2 , and 3 hr. Since the initial concentration was assumed to be zero everywhere, with no oxygen demand imposed, these results constitute predictions of the maximum achievable increase in local concentration for an airflow rate of 46 scfm. They also indicate how poorly distributed the dissolved oxygen might be with a single diffuser operating for only a short time in an initially anaerobic reservoir.

Two Diffusers, 15 ft Apart

Figure 31 (prepared by USGS) shows the layout of data stations for experiments with two diffusers separated by a distance of 15 ft. As before, the numerical labels indicate only the order in which the ADV measurements were taken. To reduce the computer memory and CPU time used in the numerical simulation, symmetry was invoked, and a computational grid was employed that covered only one-half of the region of influence. Figure 32 offers a plan view of the entire grid, while Figure 33 presents a closer, quarter-plane view showing computational data stations and grid detail near the diffuser.

Figures 34 through 38 compare MAC3D predictions for velocity magnitude with experimental data for an airflow rate of 46 scfm. Figure 39 offers a plot of background velocities measured under quiescent conditions with no airflow through the diffuser. The relative agreement between computed and observed velocities is about the same as that for the single diffuser. In the far field (Stations 4, 8), the diffuser-driven velocities hardly exceed the background velocities at all. The same is true for the lower 20 ft at the intermediate location (Stations 3,7). Only in the near field (Stations 1, 2, 5, and 6) do the predicted and observed velocities rise significantly above the background level for the entire depth.

Figure 40 compares gray-scale maps of predicted dissolved-oxygen concentration at elapsed intervals of 1, 2, and 3 hr. This elevation view shows the west half of the east-west plane of symmetry that connects the two diffusers, with the far-field boundary on the left and with the north-south plane of symmetry (between the diffusers) on the right.

Two Diffusers, 40 ft Apart

Figure 41 (prepared by USGS) shows the layout of data stations for experiments with two diffusers separated by a distance of 40 ft. Once again, the numerical labels indicate only the order in which the ADV measurements were taken. As before, to reduce the computer memory and CPU time used in the numerical simulation, symmetry was invoked, and a computational grid was employed that covered only one-half of the region of influence. Figure 42 offers a plan view of the entire grid, while Figure 43 presents a closer, quarter-plane view showing computational data stations and grid detail near the diffuser.

Figures 44 through 47 compare MAC3D predictions for velocity magnitude with experimental data for an airflow rate of 46 scfm. Figure 48 offers a plot of background velocities measured under quiescent conditions with no airflow through the diffuser. The relative agreement between computed and observed velocities is about the same as that for the previous comparisons. In the far field (Stations 4, 8), the diffuser-driven velocities hardly exceed the background velocities at all. The same is true for the lower 20 ft at the intermediate location (Stations 3, 7). Only in the near field (Stations 1, 2, 5, and 6) do the predicted

and observed velocities rise significantly above the background level for the entire depth.

Figure 49 compares gray-scale maps of predicted dissolved-oxygen concentration at elapsed intervals of 1, 2 , and 3 hr. As in the previous two-diffuser case, this elevation view shows the west half of the east-west plane of symmetry that connects the two diffusers, with the far-field boundary on the left and with the north-south plane of symmetry (between the diffusers) on the right.

Four Diffusers, 40 × 65 ft Apart

Figure 50 (prepared by USGS) shows the layout of data stations for experiments with four diffusers separated by an east-west distance of 40 ft and a north-south distance of 65 ft. Once again the numerical labels indicate only the order in which the ADV measurements were taken. As before, to reduce the computer memory and CPU time used in the numerical simulation, symmetry was invoked, but this time a computational grid was employed that covered only one-quarter of the region of influence. Figure 51 offers a plan view of the entire grid, while Figure 52 presents a closer view showing computational data stations and grid detail near the one diffuser that was included in the grid.

Figures 53 through 58 compare MAC3D predictions for velocity magnitude with experimental data for an airflow rate of 46 scfm. Figure 59 offers a plot of background velocities measured under quiescent conditions with no airflow through the diffusers. Except for Station 6, where the model consistently under-predicts the measurements by more than a factor of two, the relative agreement between computed and observed velocities is about the same as that for the previous cases. In the far field (Stations 3, 8), the predicted velocities are of the same magnitude as the background velocities.

Figures 60 and 61 present gray-scale maps of predicted dissolved-oxygen concentration at elapsed intervals of 1, 2 , and 3 hr. Figure 60 shows the west half of the east-west plane of symmetry, with the far-field boundary on the left and with the north-south plane of symmetry on the right. Figure 61 shows the north-half of the north-south plane of symmetry, with the far-field boundary on the right and with the east-west plane of symmetry on the left.

6 Model Predictions for a Flooded Quarry with Stratification

Background

The flow and transport simulations discussed in Chapter 5 were done a priori; i.e., they were executed before experimental data were available for velocity, temperature, and dissolved-oxygen in Egan Quarry. Only the diffuser airflow rates and the nominal water depth were known in advance, and no attempt was made to adjust the model predictions after the fact. Since the initial temperatures and dissolved-oxygen concentrations were unknown at the time these computations were made, the quarry was assumed initially to be isothermal and uniformly anaerobic. The latter condition is unlikely to exist in actual reservoirs, and the dissolved-oxygen predictions in Chapter 5 should be regarded as indicators of gas-transfer performance for the worst case possible without biological or chemical demand.

After all the Egan Quarry data were reduced by USGS and communicated to WES, the single and multiple diffuser simulations of Chapter 5 were repeated with MAC3D, this time with the observed initial profiles of temperature and dissolved oxygen as input for the numerical model. Two sets of initial conditions were used. The strongly stratified case represents the condition existing before the diffusers were turned on at all, while the weakly stratified case embodies the condition existing after the diffusers had been run long enough to break up most of the existing local stratification. Once the latter was accomplished, the diffusers were turned off until all diffuser-induced motion abated, and then they were restarted to test diffuser performance under weakly stratified conditions.

With weak initial stratification, the computed velocities differed only slightly from those presented in Chapter 5, and the overall agreement between prediction and experiment was essentially unchanged. The other condition, with strong initial stratification, entailed two weakly stratified layers separated by a sharp thermocline. In this case, the computed velocities (not shown here) were grossly

different from those observed, indicating that the MAC3D model in its present form is not applicable for diffusers operating in the presence of a sharp density gradient. The error arises from the tendency of the idealized bubble plume to draw too much cold water from the bottom toward the surface. Once this colder (heavier) water leaves the plume, there are no bubbles to sustain its buoyancy, and it plummets back toward the bottom. The end result is a predicted mixing action that is considerably stronger than that observed near the plume.

The temperature and dissolved-oxygen predictions given in this chapter were made a posteriori (after the fact) with the diffusion coefficient set at 20 percent of the eddy viscosity ($v_D = 0.2\, v$). For weak initial stratification, ratios v_D / v much larger than 0.2 produced excessive turbulent (diffusive) mixing, while ratios much smaller than 0.2 had the opposite effect. For strong initial stratification, however, adjusting the diffusion coefficient (alone) proved generally ineffective for reconciling prediction with experiment. All the results present .I in this chapter were obtained for an airflow rate of 46 scfm.

Gas Transfer for Weak Stratification

In practice, bubble diffusers are used not only for aerating reservoirs but for mixing them as well. The aim is to prevent the development of anaerobic or stratified conditions anywhere in an impoundment. If the latter goal is adequately achieved during normal (continuous or intermittent) operation, then an aeration system should encounter strong thermoclines only after extended periods of inoperation. Thus, with regard to the field tests conducted in Egan Quarry, the cases with weak initial stratification are the most representative for normal diffuser operation.

Figures 62 and 63 compare MAC3D predictions with single-diffuser experimental data for temperature and dissolved oxygen, respectively, after elapsed times of 15 and 120 min. The reported data station lies 10 ft from the diffuser, and the weakly stratified initial conditions (for both model and experiment) are indicated by a dotted curve. Initial gradients near the surface are eliminated within the first 15 min, and little change occurs in the vertical profiles during the next 2 hr. The near-surface reduction in temperature and dissolved oxygen occurs because the bubble plume draws colder, less oxygen-rich water from the bottom and forces it outward along the surface.

Figures 64 and 65 compare MAC3D predictions with experimental data for temperature and dissolved oxygen, respectively, for two diffusers set 15 ft apart. The reported data station lies halfway between the diffusers. Initial conditions for both model and experiment are indicated by a dashed curve in the figures, and the same qualitative trends are evident here as in the single-diffuser experiment. As before, the near-surface gradients are eliminated by the diffuser-induced flow; but in this case, all the observed values for dissolved oxygen decrease from their initial values. Since the decrease is roughly the same at all elevations, with no obvious physical or biological agent to account for such a

rapid change, this data shift may be attributable to some sort of experimental error.

Figures 66 and 67 compare MAC3D predictions with experimental data for temperature and dissolved oxygen, respectively, for two diffusers set 40 ft apart. The reported data station lies 10 ft east (right) of the west (left) diffuser shown in Figure 41, and initial values for both model and experiment are indicated by a dashed curve in Figures 66 and 67. With regard to temperature, the same trends are evident here as in the previous cases. For dissolved oxygen, however, the results are different. In the experimental data, the concentration remains weakly stratified after 2.5 hr. In contrast, the model predicts almost complete mixing, with the concentration becoming nearly uniform after 2.5 hr.

Figures 68 and 69 compare MAC3D predictions with experimental data for temperature and dissolved oxygen, respectively, for a rectangular array of four diffusers, 40 × 65 ft apart. The reported data station lies at the center of the four-diffuser array shown in Figure 50, and initial values for both model and experiment are indicated by a dashed curve in Figures 68 and 69. The model and the data both indicate nearly complete mixing at this station after an elapsed time of 2 hr.

In the Egan Quarry diffuser tests, the (elapsed) observation times of a few hours were too brief for the diffusers to add significantly to the existing dissolved-oxygen concentration in the water. In fact, the only discernible effect was local mixing (destratification) of the weakly stratified initial conditions. For the airflow rate used here (46 scfm), the greatest possible (predicted) increases in dissolved-oxygen concentration would be those computed for initially anaerobic water in Chapter 5, shown in Figures 30, 40, 49, 60, and 61.

The generally favorable comparison of MAC3D predictions with observed temperatures and dissolved-oxygen concentrations lends support for the model's usefulness in weakly stratified environments, but the elapsed times are too short to confirm its desired reliability over intervals of days or weeks. Experiments of the latter duration are crucial if the model is to be used for estimating the appropriate spacing between diffusers in multidiffuser aeration systems.

Gas Transfer for Strong Stratification

In the course of the Egan Quarry diffuser tests, temperature and dissolved-oxygen data were also collected for strongly stratified initial conditions. While the latter do not represent a typical operating environment for an aeration system, they do offer an extreme setting in which to challenge the numerical model's predictive capabilities.

Figures 70 and 71 compare MAC3D predictions with single-diffuser experimental data for temperature and dissolved oxygen, respectively, after elapsed times of 15, 60, and 180 min. The reported data station lies 10 ft from the diffuser, and the strongly stratified initial conditions (for both model and

experiment) are indicated by a dotted curve. Initial gradients are effectively eliminated in the upper 20 ft within 15 min, with little change occurring thereafter in either the predictions or the data. In the lower 20 ft, however, the observed gradients change hardly at all, while the predicted gradients change dramatically and continuously. In particular, the computed oxygen-rich region is forced prematurely downward by plunging colder water (drawn up from the bottom) as it flows out of the bubble plume and mixes with warmer water near the surface. The result is that the model overpredicts the rate at which the colder, oxygen-poor (bottom) region is warmed and aerated.

Figures 72 and 73 compare MAC3D predictions with experimental data for temperature and dissolved oxygen, respectively, for two diffusers set 15 ft apart. The reported data station lies halfway between the diffusers. Initial conditions for both model and experiment are indicated by a dashed curve in the figures, and the same qualitative trends are evident here as in the single-diffuser experiment. According to the data, the upper 23 ft are fully mixed within 2 hr, but the lower 17 ft are essentially unchanged. In contrast, the numerical model predicts the upper 30 ft to be fully mixed and the lower 10 ft to be partially mixed.

Figures 74 and 75 compare MAC3D predictions with experimental data for temperature and dissolved oxygen, respectively, for two diffusers set 40 ft apart. The reported data station lies 10 ft east (right) of the west (left) diffuser shown in Figure 41, and initial values for both model and experiment are indicated by a dashed curve in Figures 74 and 75. Here the experimental results (after 1.5 hr) are nearly identical with those shown for the previous case (after 2 hr) in Figures 72 and 73. The model, however, predicts less mixing for this configuration and station than for the other.

Figures 76 and 77 compare MAC3D predictions with experimental data for temperature and dissolved oxygen, respectively, for a rectangular array of four diffusers, 40 × 65 ft apart. The reported data station lies at the center of the four-diffuser array shown in Figure 50, and initial values for both model and experiment are indicated by a dashed curve in Figures 76 and 77. Unlike the previous comparisons for strong initial stratification, the model here predicts less mixing than that observed in the experiments for the upper 30 ft after an elapsed time of 2 hr. This tendency notwithstanding, the oxygen concentration (and the rate of mixing) is still overpredicted for the lower 10 ft.

The upshot of Figures 70-77 is that MAC3D, when employed in its present form for bubble-diffuser applications, will generally overpredict the initial rates of warming and aeration for cold, oxygen-poor layers near the bottoms of reservoirs with strong stratification. Until some way is found to eliminate this deficiency, the model should be used only for bubble diffusers operating in unstratified or weakly stratified environments.

7   Conclusion

The MAC3D numerical model has finally reached a state of maturity that warrants its judicious implementation for engineering flow problems in deep reservoirs and other circumstances where free-surface motion can be neglected. Although much remains that can still be done to improve its capabilities, the existing code now offers enough breadth and flexibility of application to serve as a useful complement, and occasionally as an alternative, to physical models and field tests alike. While it would be foolish to abandon experimentation completely in favor of numerical simulation, it would nevertheless be wise to use models like MAC3D as much as possible to eliminate redundant physical testing. The first question always to be answered is how best to obtain the information needed for the problem at hand. If numerical models can reduce the need for costly experiments, then not to use them would be poor engineering indeed. On the other hand, the misapplication of numerical models, especially with insufficient validation, inevitably begs for trouble.

Concerning validation for bubble diffusers, the comparisons presented in Chapters 4-6 offer support for at least one intended capability of MAC3D. Specifically, the model seems able to predict (within a factor of two) the time-averaged intensity of flow created at any location by one or more diffusers with a specified airflow rate, so long as the initial stratification is fairly weak. To reproduce all the rapidly varying details of the real flow, however, would require a numerical model far more complex than MAC3D.

Even to reproduce the slowest of the time-varying details for bubble plumes is difficult with a model of the present kind, which assumes the plume axis to be fixed in space. Real plumes wander in all directions, and simulation of this kind of behavior requires a model that tracks the motions of individual bubbles (Delnoij et al. 1997). While this does not require computing the flow about every bubble, it does entail more work than is practical for multiple plumes, because a separate equation of motion has to be solved for each of the thousands of bubbles.

In laboratory experiments conducted under otherwise controlled conditions, plume wander makes it difficult to achieve repeatability even for velocity data averaged over long periods of time (Milgram 1983). This was evident in the tank experiments conducted at WES, in which repeated (time-averaged) velocity measurements at the same locations (Figure 6) differed by as much as

50 percent. In the field tests conducted at Egan Quarry, repeatability was hindered even further by background motion (Figures 29, 39, 48, and 59), possibly arising from surface winds and lateral temperature gradients. Thus, in view of these uncertainties in the experimental results, it seems inappropriate (for now) to propose confidence limits for velocity predictions. The confidence limits eventually to be established should concern the model's ability to predict the rate of delivery of dissolved oxygen to locations remote from arrays of one or more bubble diffusers.

With reference to the latter issue, predicted gas-transfer rates agree well with observed rates for well-mixed volumes of water, as long as a constant of proportionality relating K_{plume} and Q_{air} can be determined in advance for the bubble plumes. Nevertheless, this does not guarantee accurate gas-transfer and dissolved-gas transport predictions for larger, less-well-mixed volumes of water, such as reservoirs. While the results obtained for Egan Quarry are encouraging in this regard, the reported observation times (several hours) were too short to validate the model's intended ability to predict aerator effectiveness over realistic operating times of days or weeks. Future experimental work should include efforts to gather suitable data to validate (or correct) MAC3D's long-term, full-scale predictions for gas transfer and transport in reservoirs.

References

Bernard, R. S. (1992). "A MacCormack scheme for incompressible flow," *Computers and Mathematics with Applications* 24(5/6), 151-168.

_____. (1993). "STREMR: Numerical model for depth-averaged incompressible flow," Technical Report REMR-HY-11, U.S. Army Engineer Waterways Experiment Station, Vicksburg, MS.

_____. (1995). "Preliminary development of a three-dimensional numerical model for reservoir hydrodynamics," Technical Report HL-95-9, U.S. Army Engineer Waterways Experiment Station, Vicksburg, MS.

_____. (1996). "Preliminary validation of the MAC3D numerical flow model," *Proceedings of the North American Water and Environment Congress*, American Society of Civil Engineers, New York.

Broecker, H. C., Petermann, J., and Siems, W. (1978). "The influence of wind on CO_2 exchange in a wind-wave tunnel including the effects of monolayers," *Journal of Marine Research* 36, 595.

Clift, R., Grace, J. R., and Weber, M. E. (1978). *Bubbles, drops, and particles.* Academic Press, New York,.

Delnoij, E., Lammers, F. A., Kuipers, J. A. M., and van Swaaij, W. P. M. (1997). "Dynamic simulation of dispersed gas-liquid two-phase flow using a discrete bubble model," *Chemical Engineering Science* 52(9), 1429-1458.

Kirkgöz, M. S. (1989). "Turbulent velocity profiles for smooth and rough open channel flow," *Journal of Hydraulic Engineering* 115(11), 1543-1561.

Launder, B. E., and Spalding, D. B. (1974). "The numerical calculation of turbulent flows," *Computer Methods in Applied Mechanics and Engineering* 3, 269-289.

MacCormack, R. W. (1969). "The effect of viscosity in hypervelocity impact cratering," AIAA Paper 69-354, American Institute of Aeronautics and Astronautics.

MacCormack, R. W. (1982). "A numerical method for solving the equations of compressible viscous flow," *AIAA Journal* 20(9), 1275-1281.

Milgram, J. H. (1983). "Mean flow in round bubble plumes," *Journal of Fluid Mechanics* 133, 345-376.

Roache, P. J. (1972). *Computational fluid dynamics*. Hermosa Publishers, Albuquerque, NM.

Wilhelms, S. C., and Martin, S. K. (1992). "Gas transfer in diffused bubble plumes," *Proceedings of the Hydraulic Engineering Sessions at Water Forum '92*, American Society of Civil Engineers, New York.
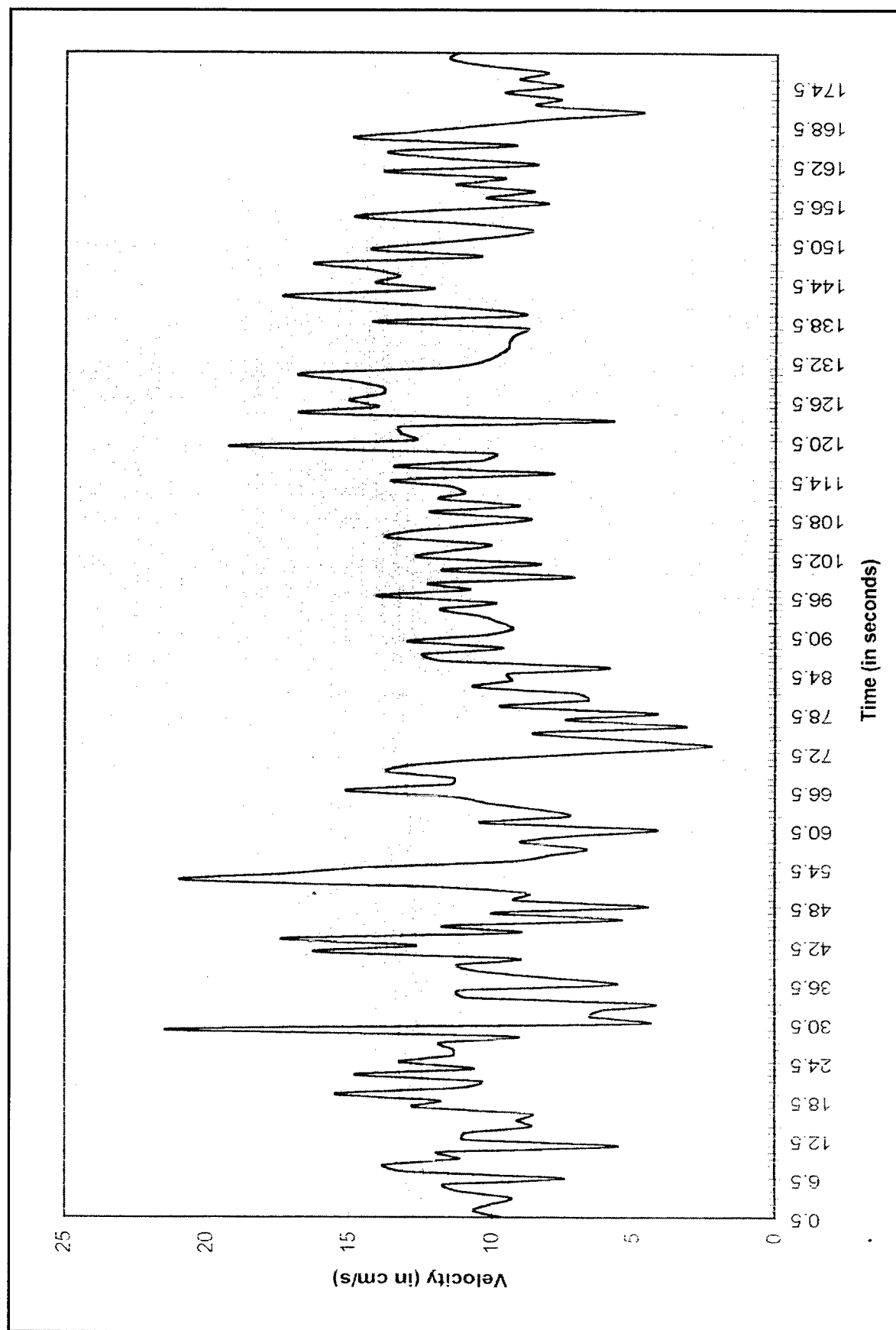
Figure 1. Unsteady velocity measurements for bubble diffuser in cylindrical tank
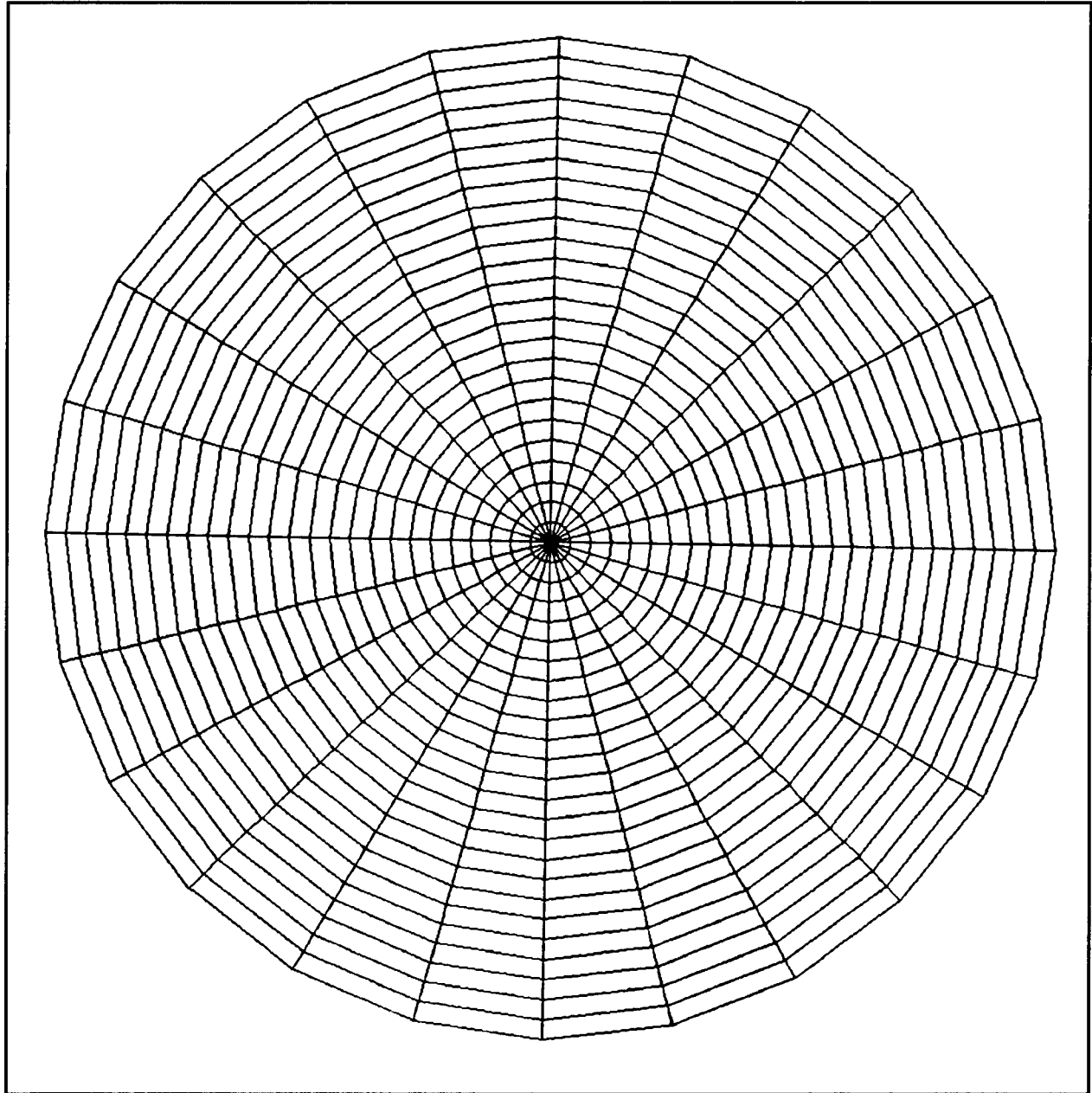
Figure 2.   Plan view of computational grid for simulations of single diffuser in 25-ft-diam cylindrical tank
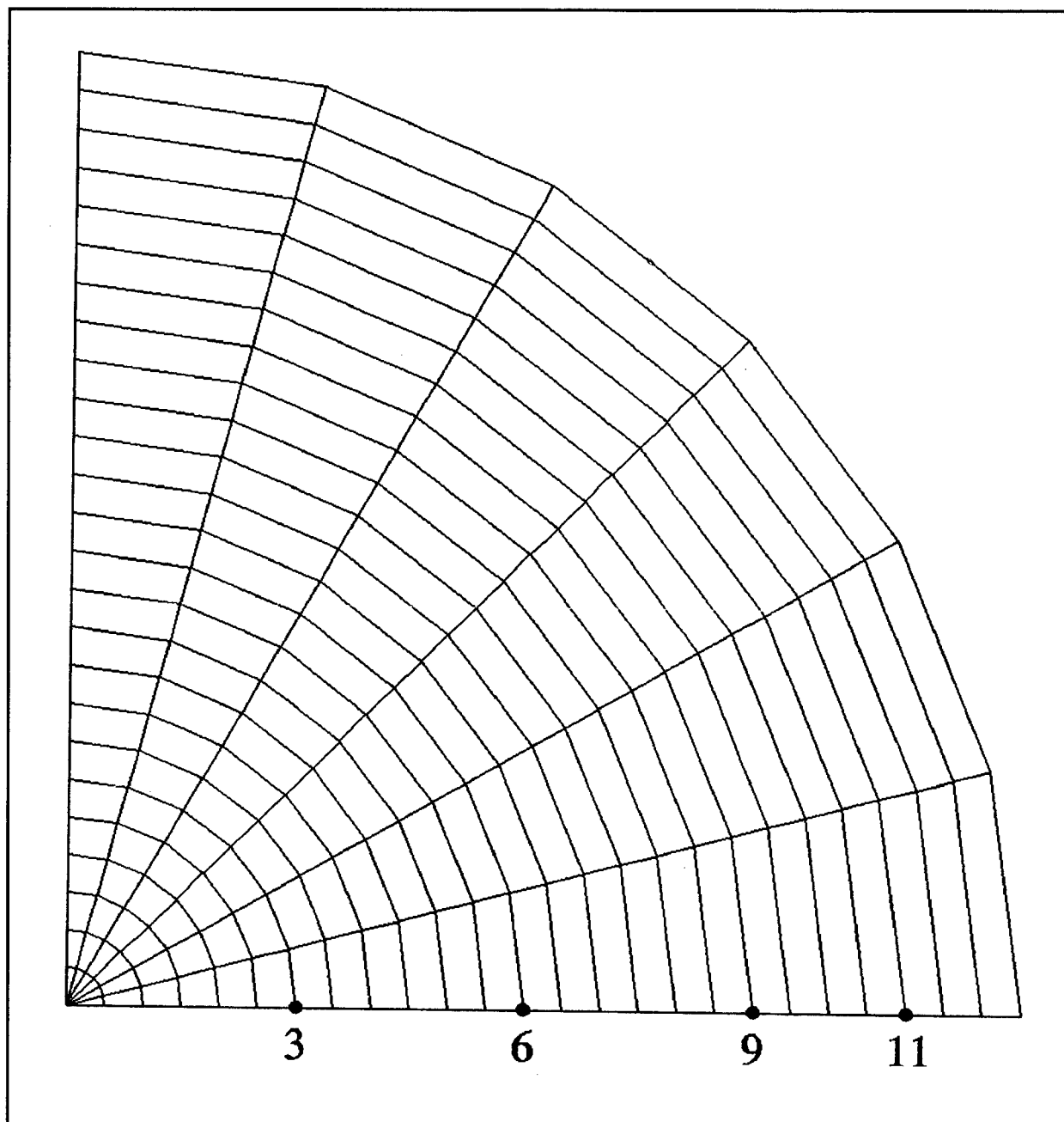
Figure 3.   Grid detail with computational data stations for single-diffuser tank simulation with 10-ft water depth
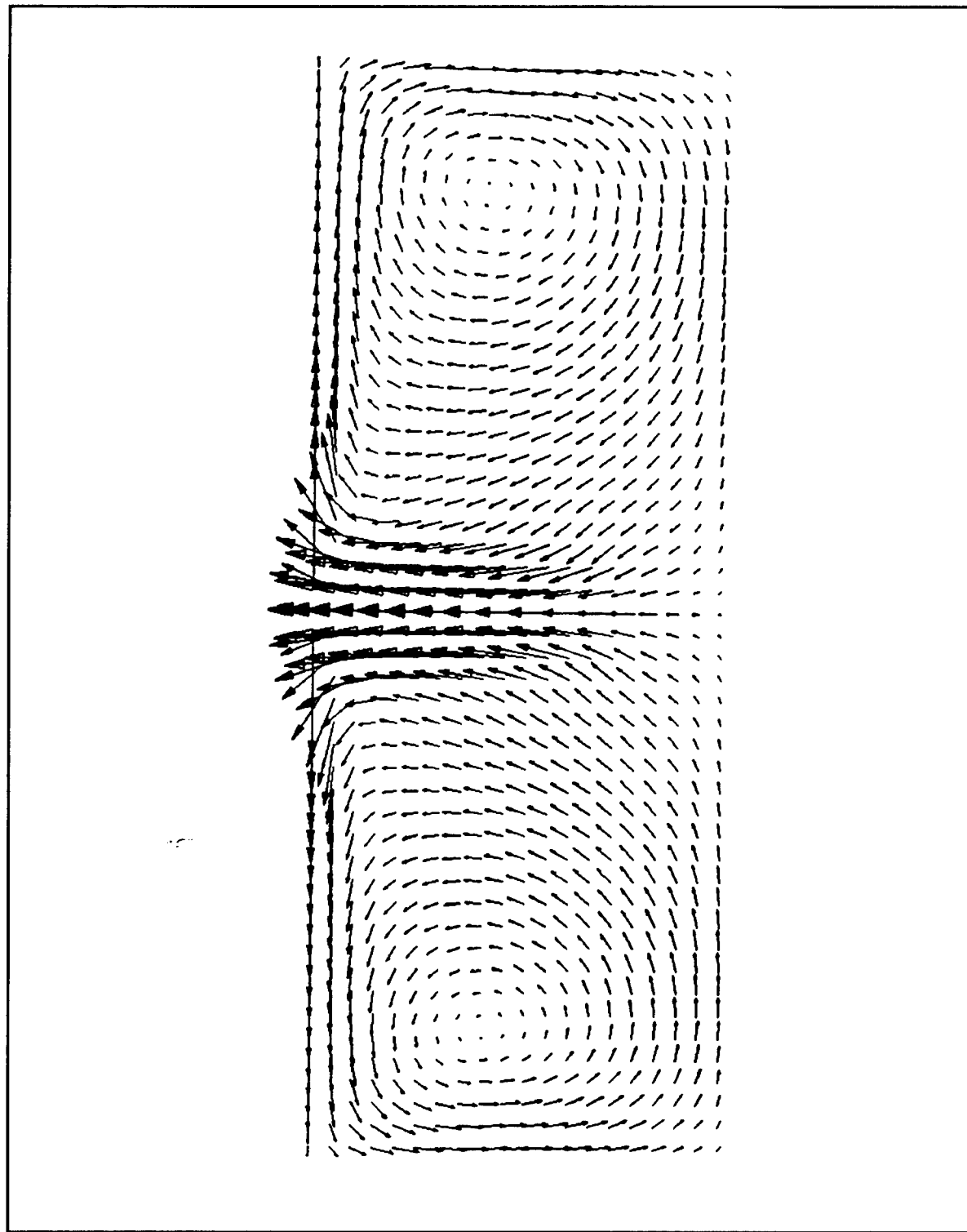
Figure 4. Elevation view of computed velocity vectors for single-diffuser tank simulation with 10-ft water depth
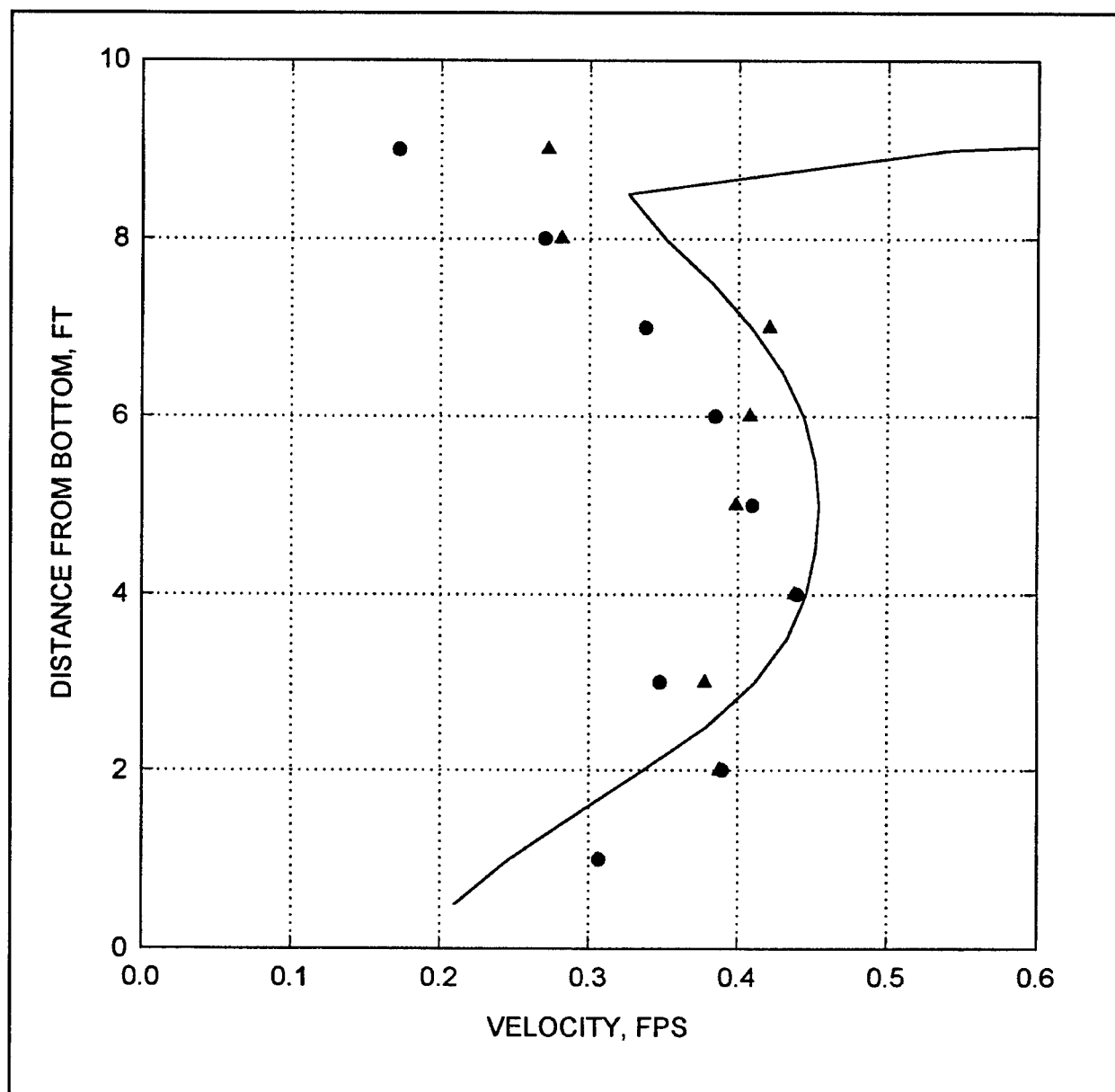
Figure 5. Predicted velocity magnitude (—), 35.5-scfm experimental data (●), and rescaled 0.88-scfm data (▲) for tank test, 10-ft depth, Station 3
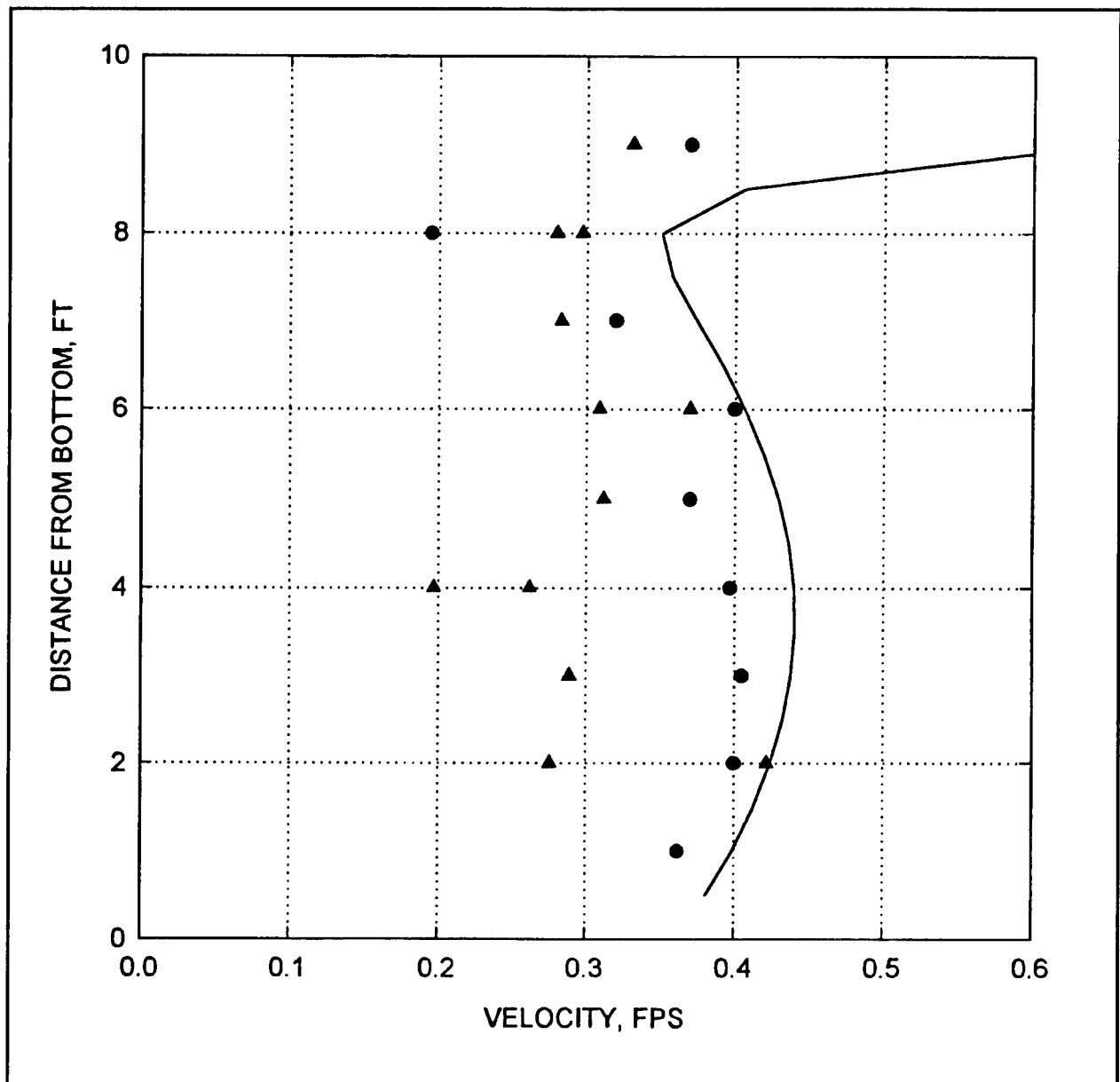
Figure 6.   Predicted velocity magnitude (—), 35.5-scfm experimental data (●), and rescaled 0.88-scfm data (▲) for tank test, 10-ft depth, Station 6
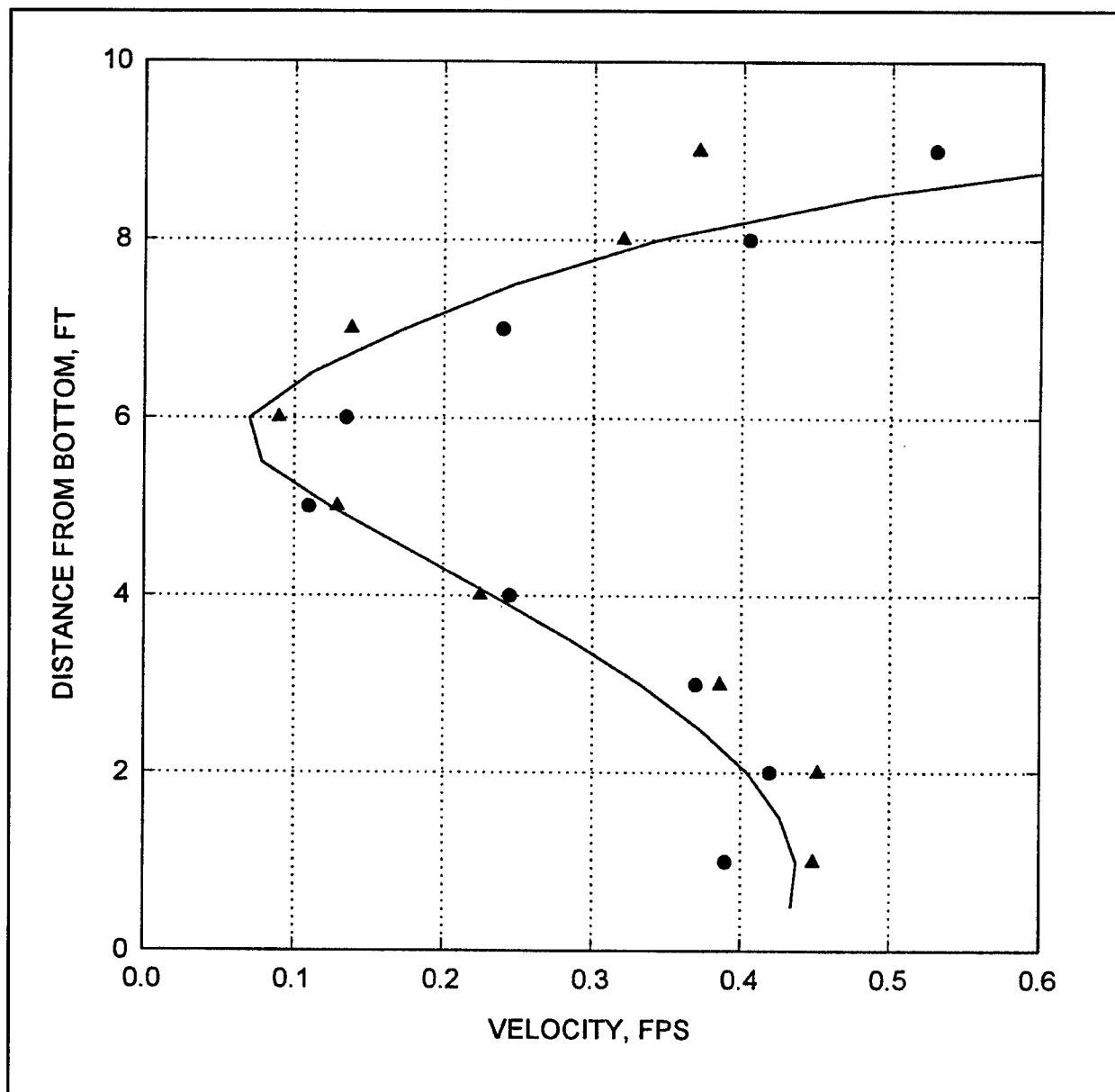
Figure 7.   Predicted velocity magnitude (—), 35.5-scfm experimental data (●), and rescaled 0.88-scfm data (▲) for tank test, 10-ft depth, Station 9
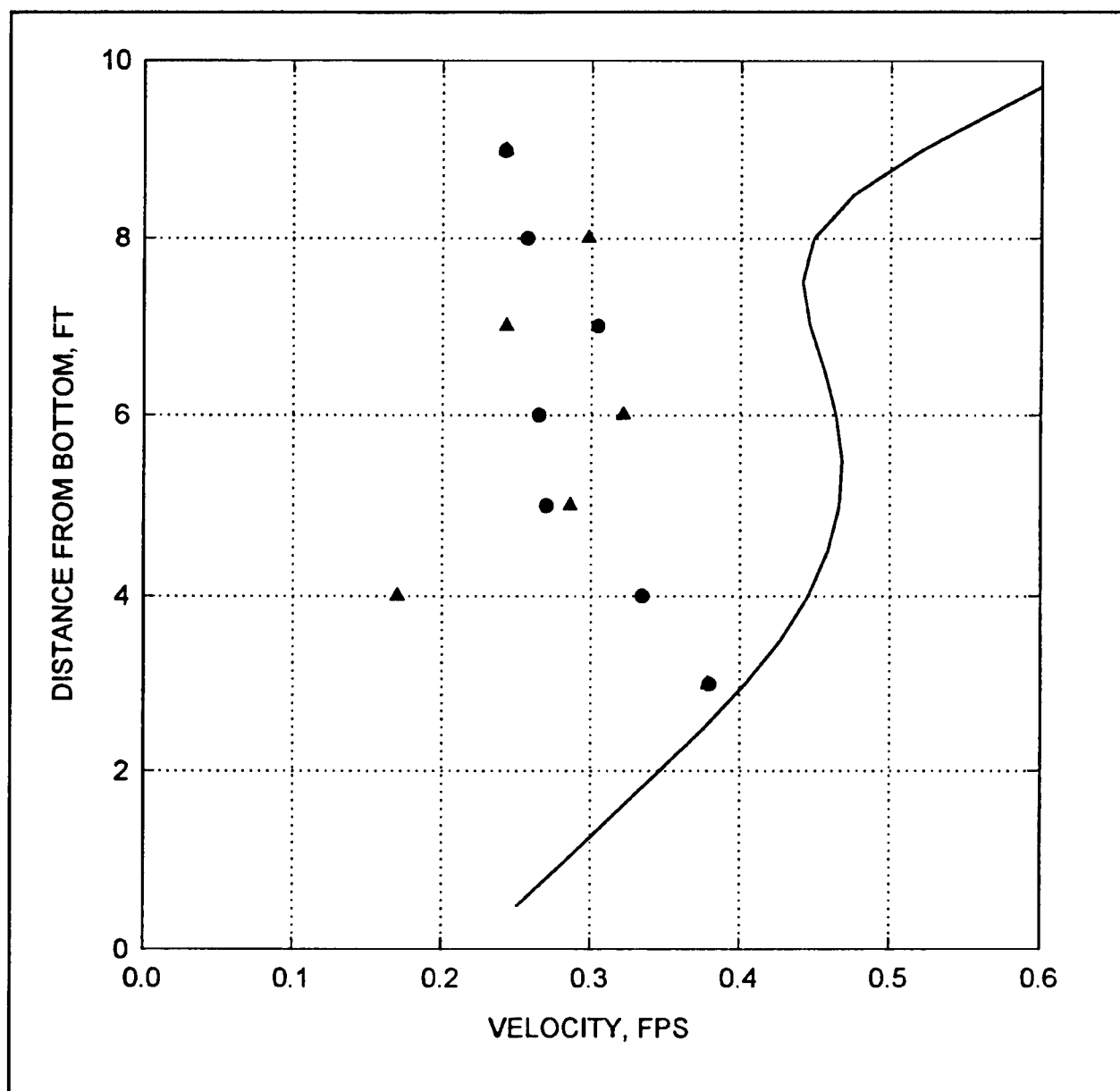
Figure 8.   Predicted velocity magnitude (—), 35.5-scfm experimental data (●), and rescaled 0.88-scfm data (▲) for tank test, 10-ft depth, Station 11
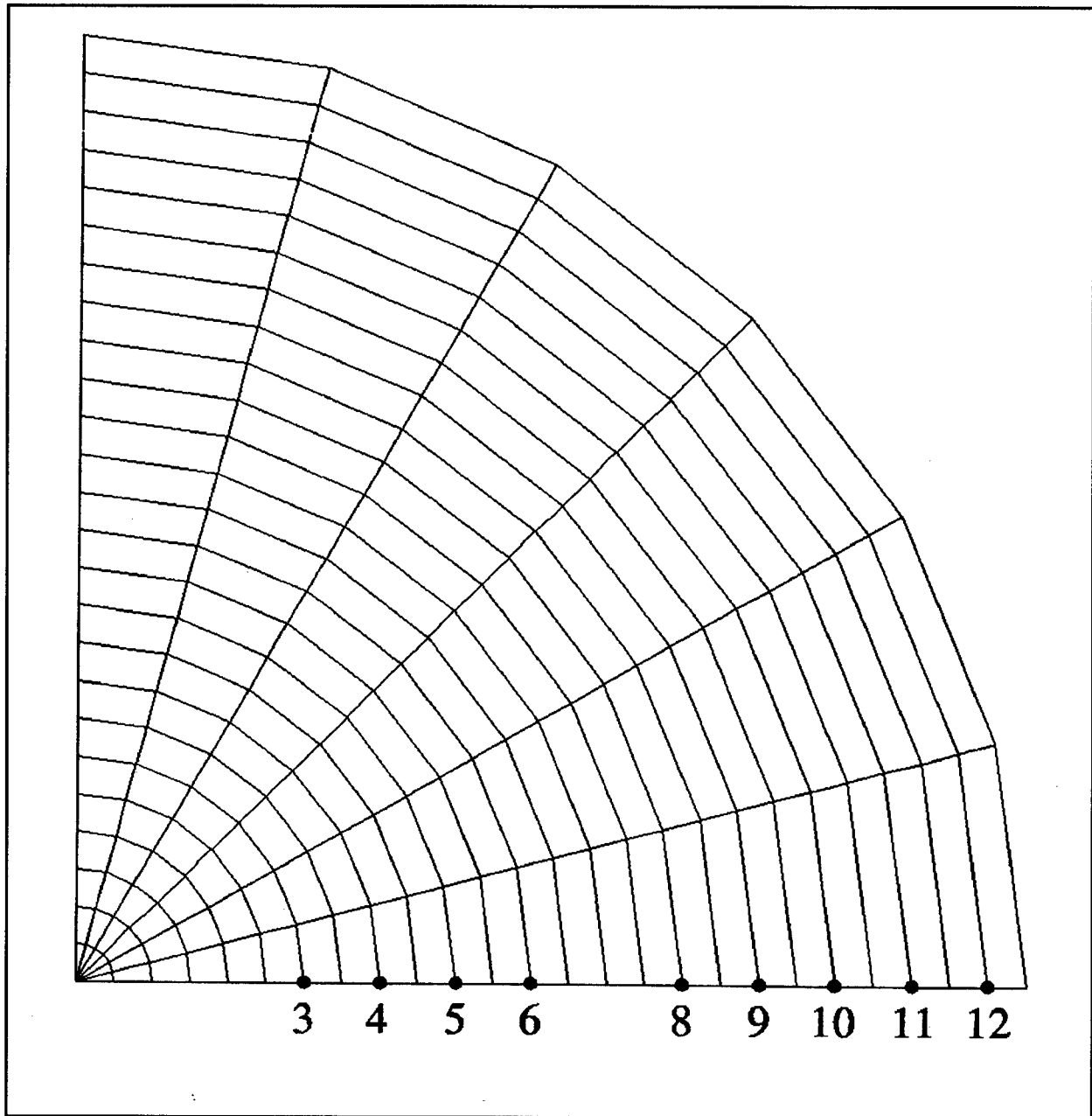
Figure 9. Grid detail with computational data stations for single-diffuser tank simulation with 31-ft water depth
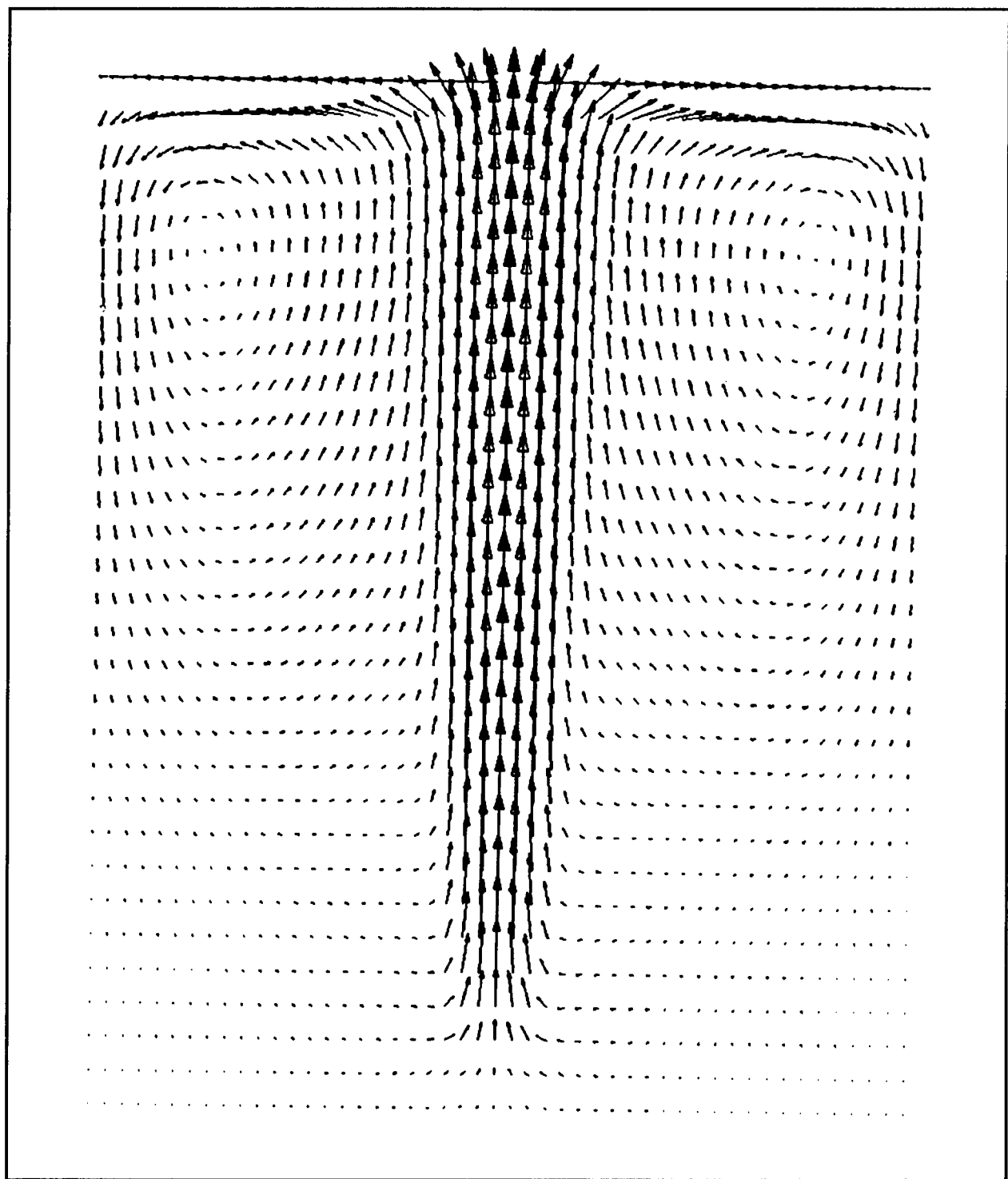
Figure 10. Elevation view of computed velocity vectors for single-diffuser tank simulation with 31-ft water depth
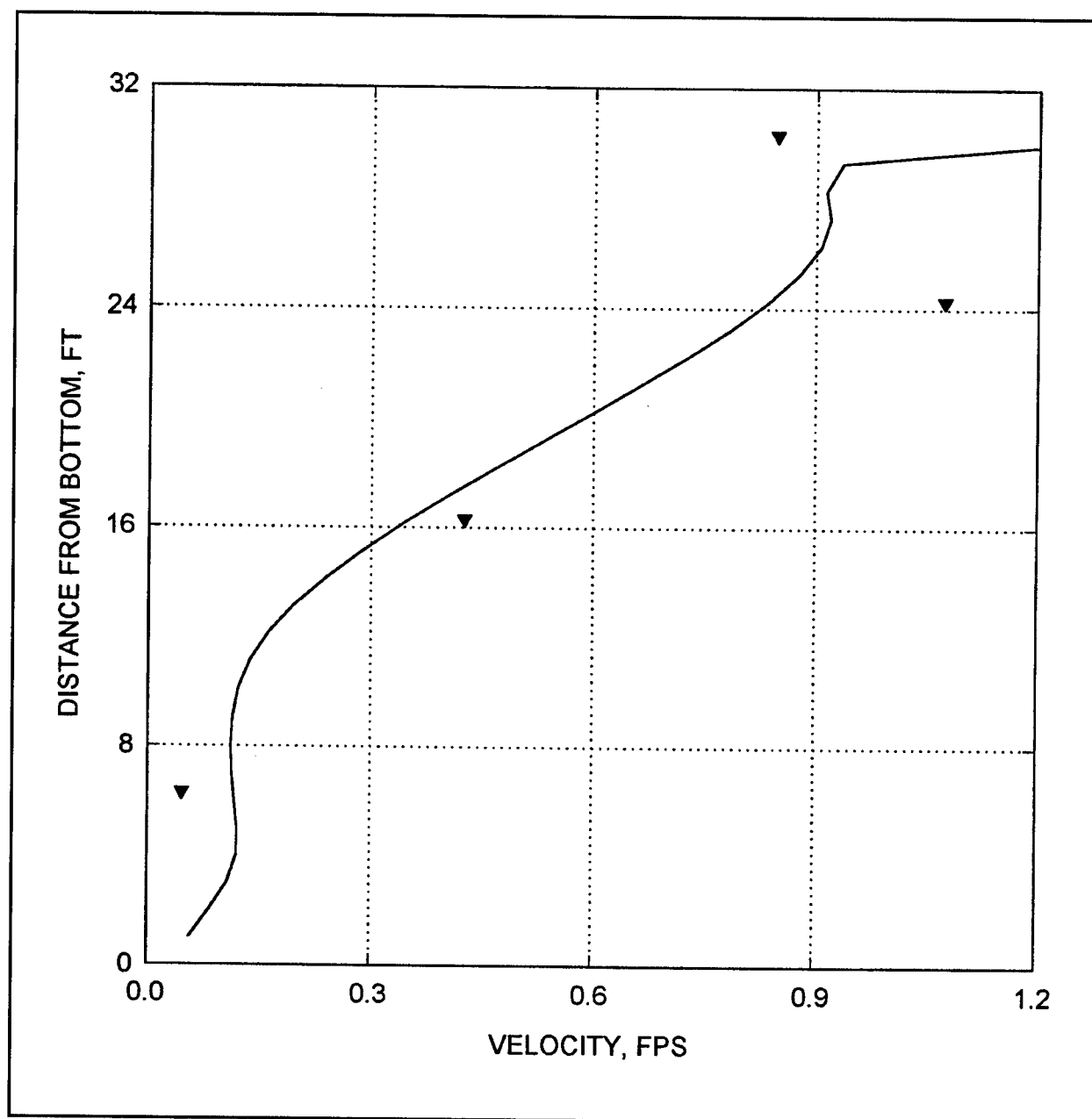
Figure 11. Predicted velocity magnitude (—), 30.5-scfm experimental data (●), and rescaled data 1.2-scfm (▲), 6.5 scfm (▼), and 13.7 scfm (■) for tank test, 31.3-ft depth, Station 3
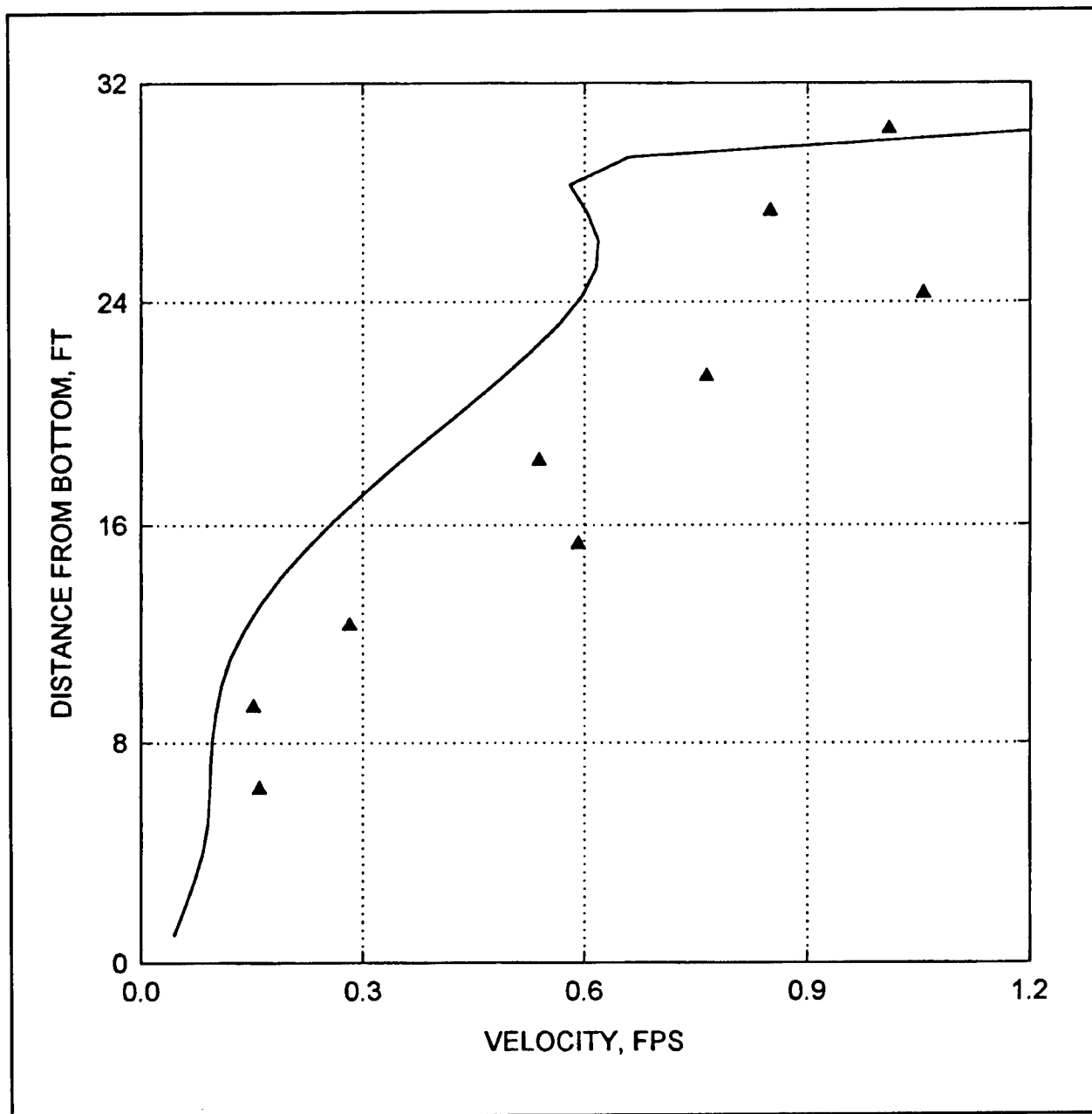
Figure 12. Predicted velocity magnitude (—), 30.5-scfm experimental data (●), and rescaled data
1.2-scfm (▲), 6.5 scfm (▼), and 13.7 scfm (■) for tank test, 31.3-ft depth, Station 4
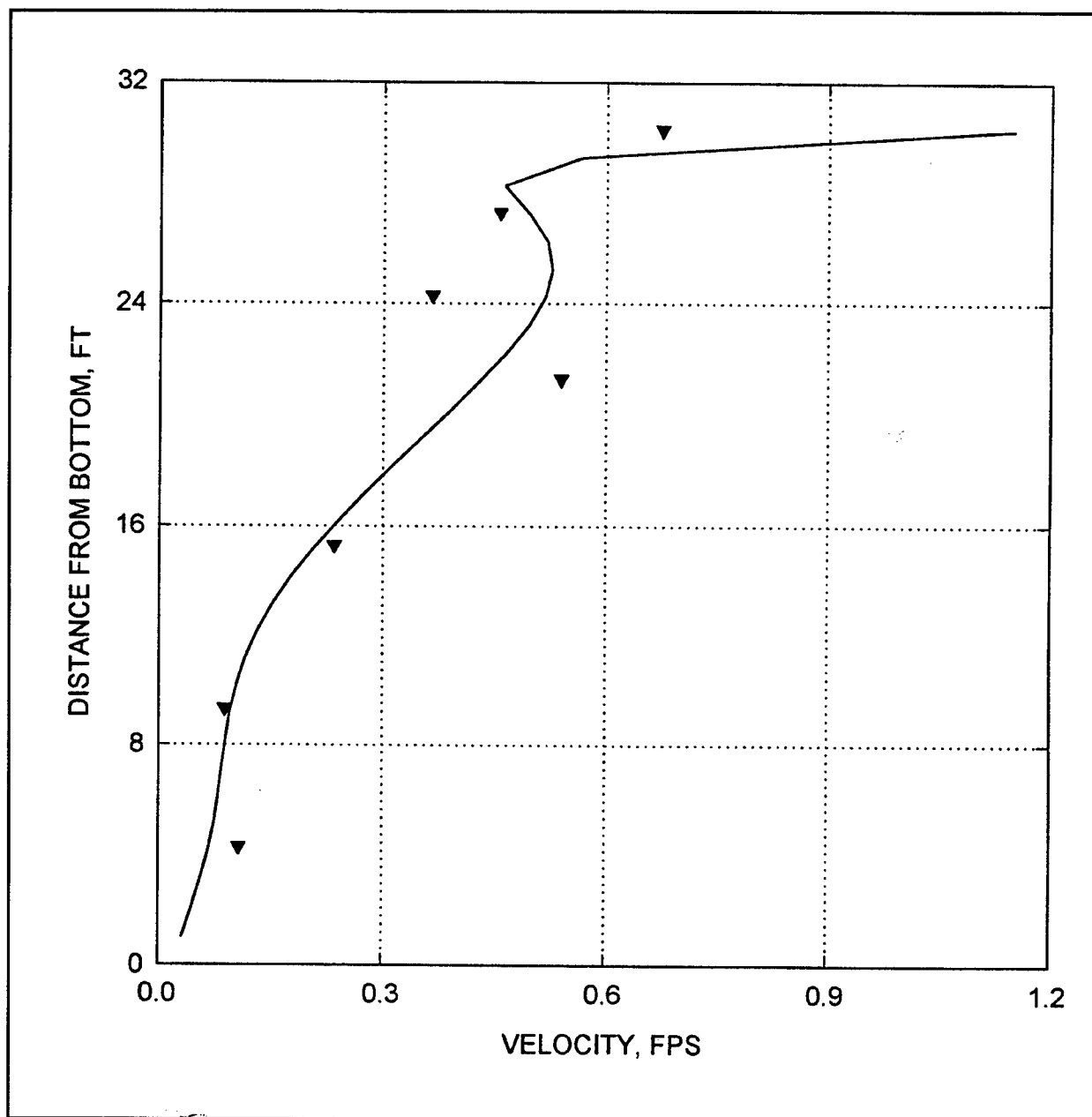
Figure 13. Predicted velocity magnitude (—), 30.5-scfm experimental data (●), and rescaled data 1.2-scfm (▲), 6.5 scfm (▼), and 13.7 scfm (■) for tank test, 31.3-ft depth, Station 5
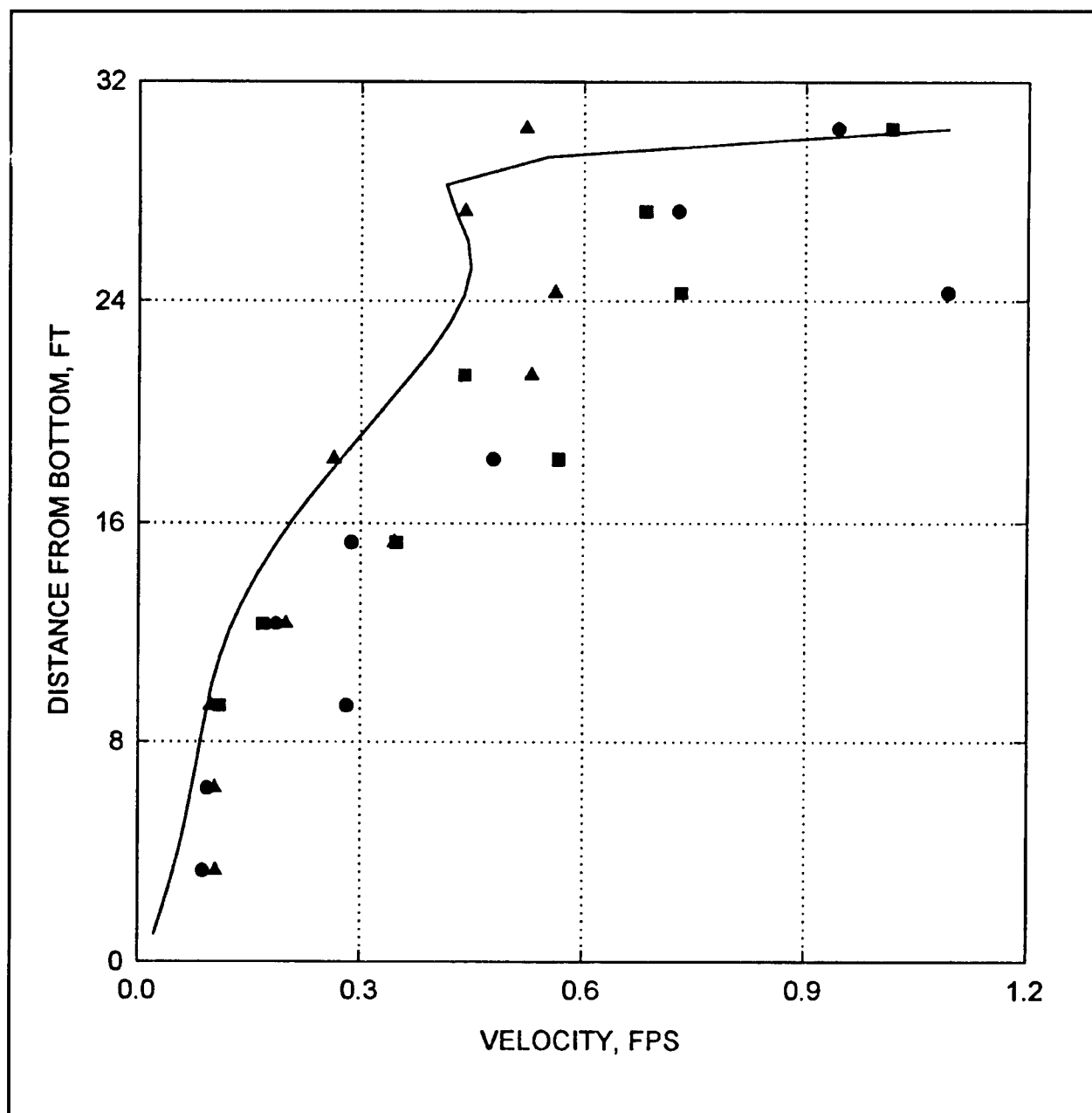
Figure 14. Predicted velocity magnitude (—), 30.5-scfm experimental data (●), and rescaled data
1.2-scfm (▲), 6.5 scfm (▼), and 13.7 scfm (■) for tank test, 31.3-ft depth, Station 6
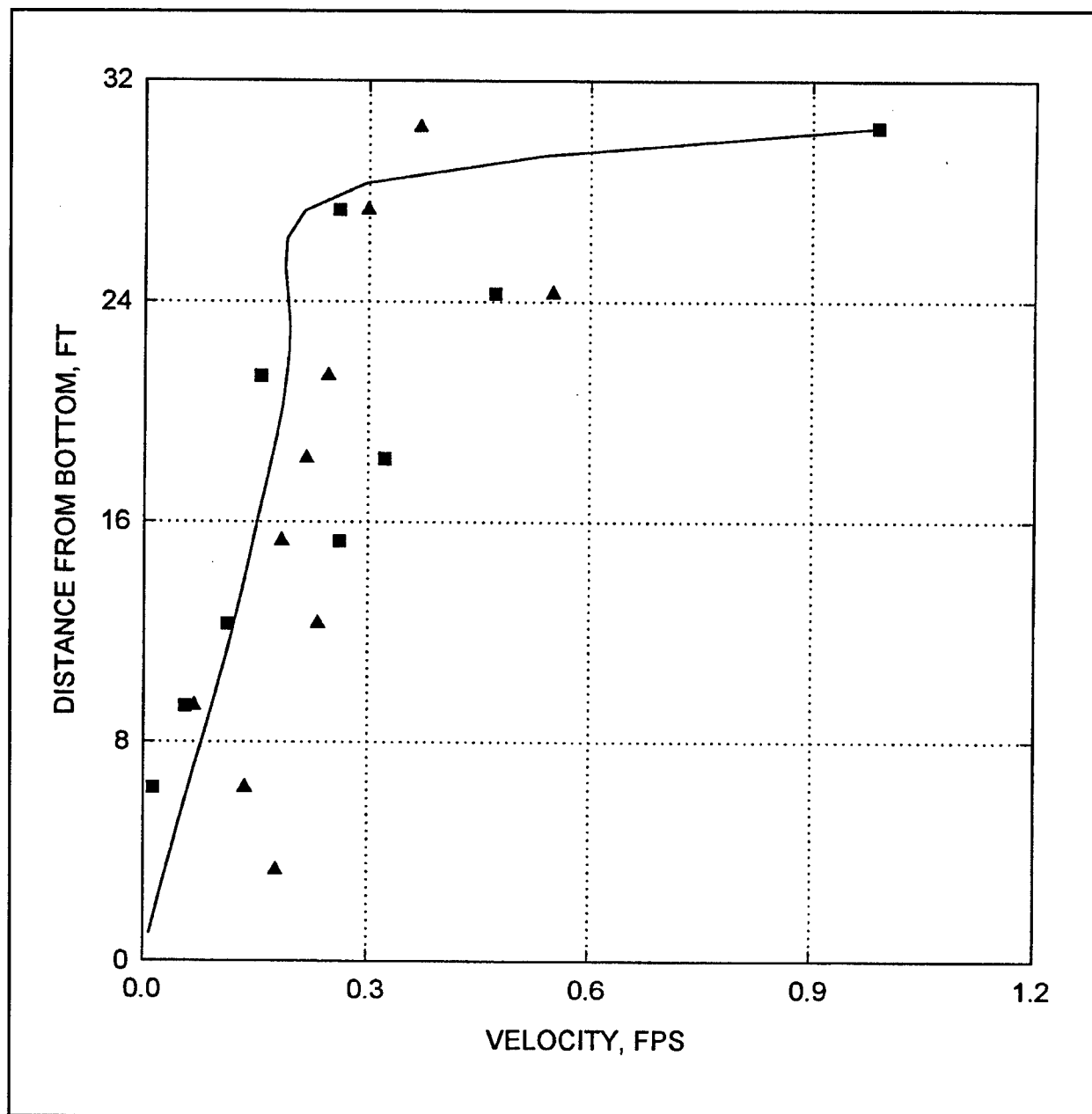
Figure 15.   Predicted velocity magnitude (—), 30.5-scfm experimental data (●), and rescaled data
1.2-scfm (▲), 6.5 scfm (▼), and 13.7 scfm (■) for tank test, 31.3-ft depth, Station 8
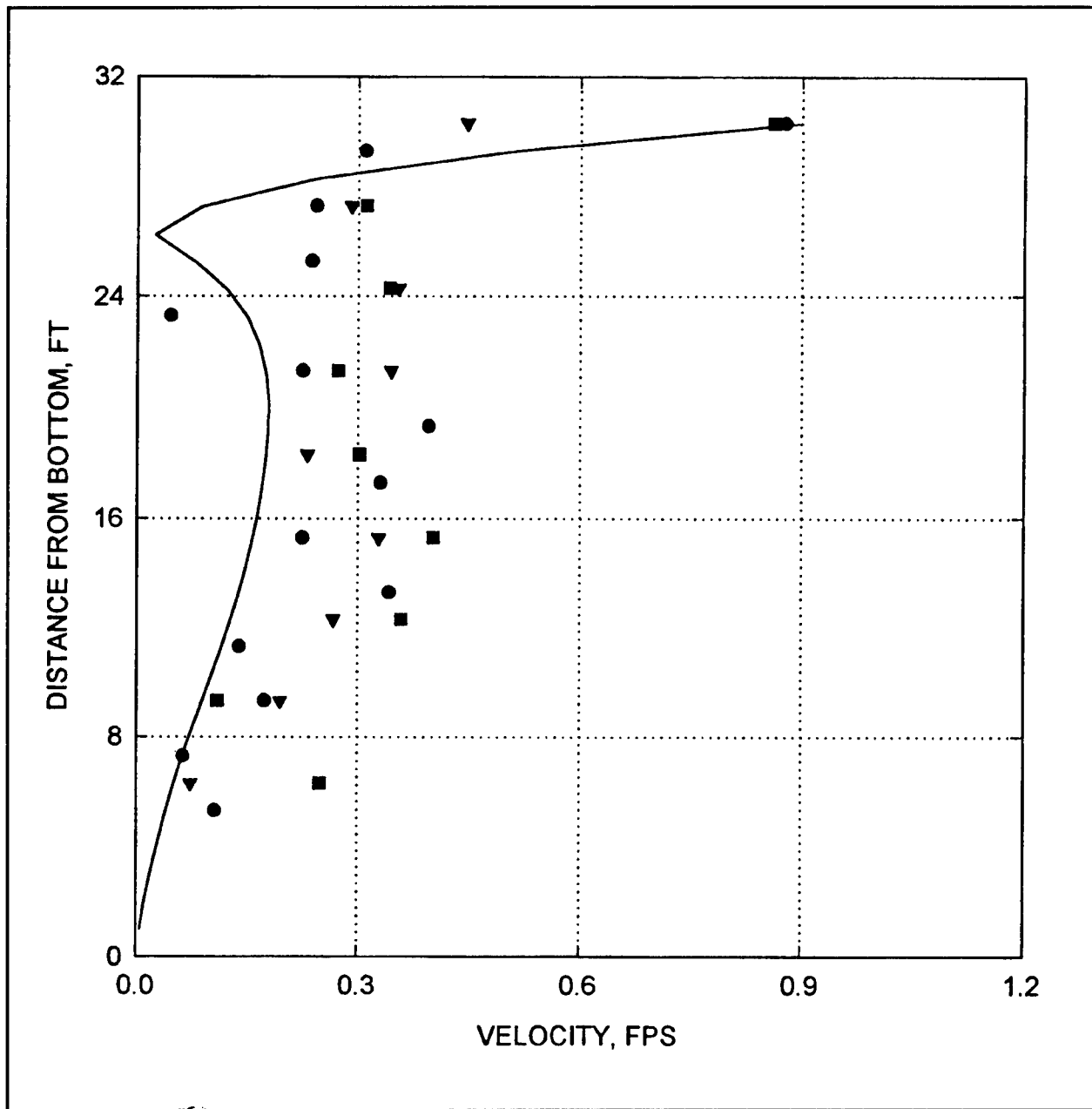
Figure 16. Predicted velocity magnitude (—), 30.5-scfm experimental data (●), and rescaled data
1.2-scfm (▲), 6.5 scfm (▼), and 13.7 scfm (■) for tank test, 31.3-ft depth, Station 9
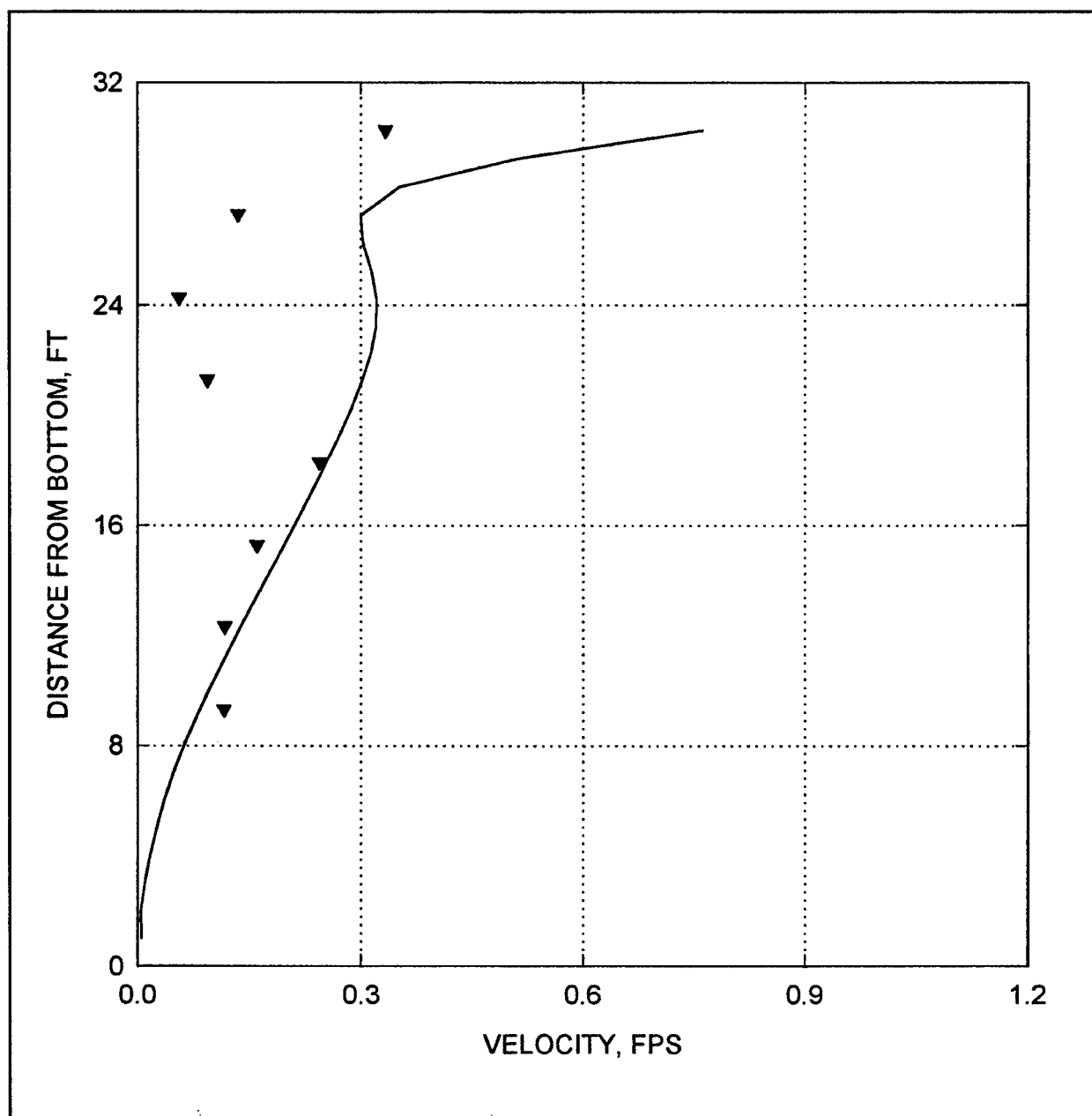
Figure 17. Predicted velocity magnitude (—), 30.5-scfm experimental data (●), and rescaled data 1.2-scfm (▲), 6.5 scfm (▼), and 13.7 scfm (■) for tank test, 31.3-ft depth, Station 10
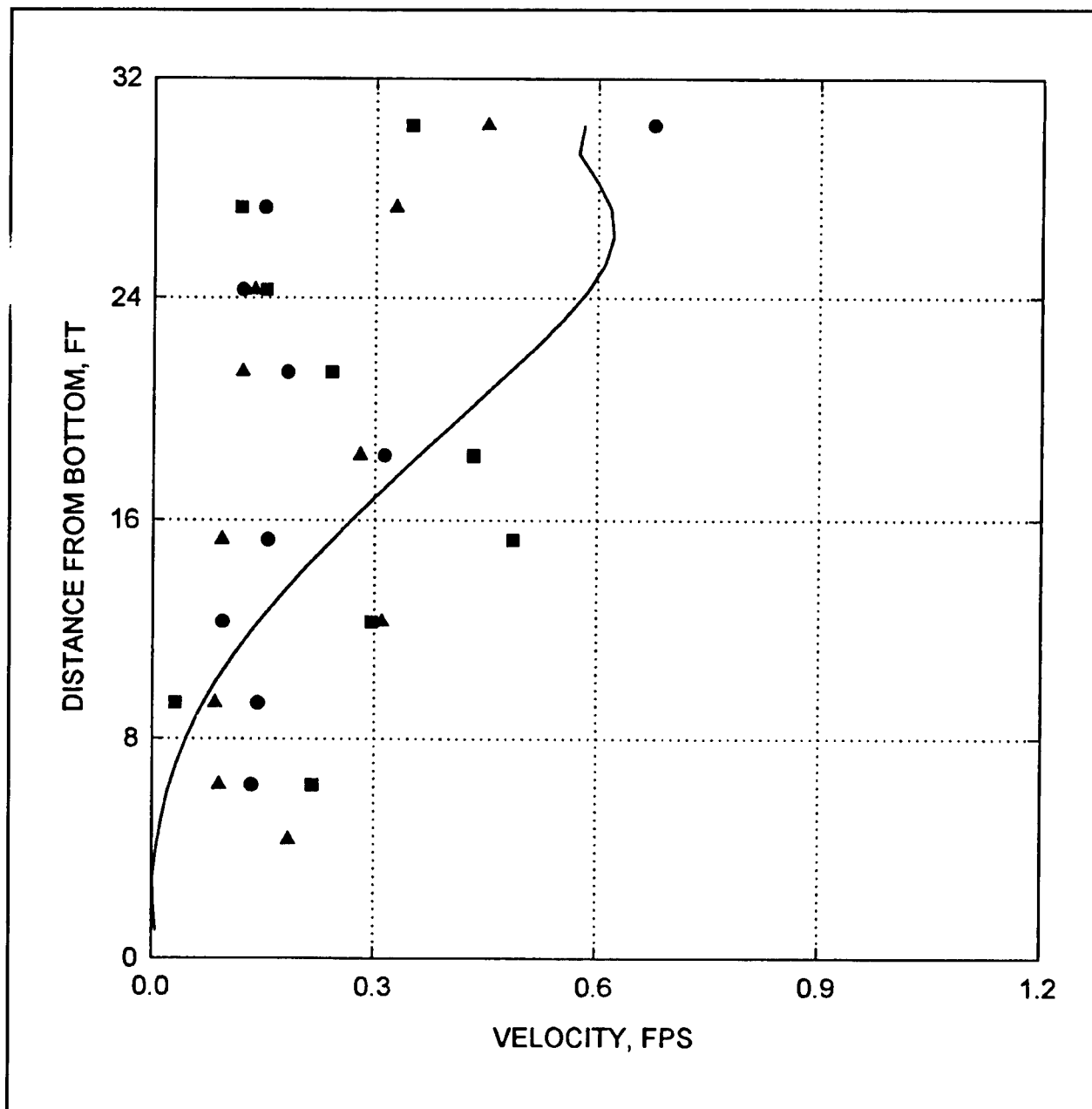
Figure 18. Predicted velocity magnitude (—), 30.5-scfm experimental data (●), and rescaled data
1.2-scfm (▲), 6.5 scfm (▼), and 13.7 scfm (■) for tank test, 31.3-ft depth, Station 11
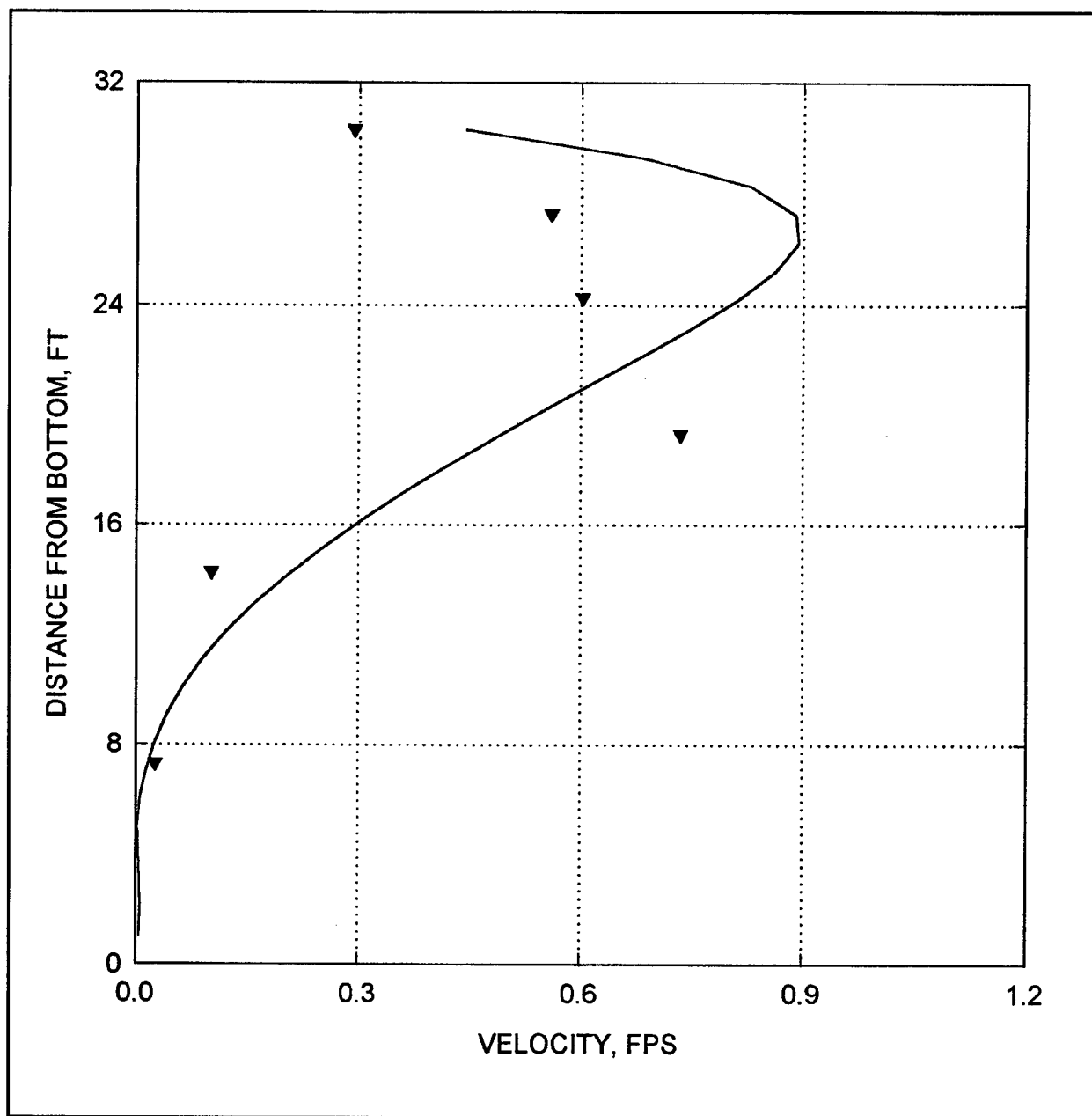
Figure 19. Predicted velocity magnitude (—), 30.5-scfm experimental data (●), and rescaled data 1.2-scfm (▲), 6.5 scfm (▼), and 13.7 scfm (■) for tank test, 31.3-ft depth, Station 12
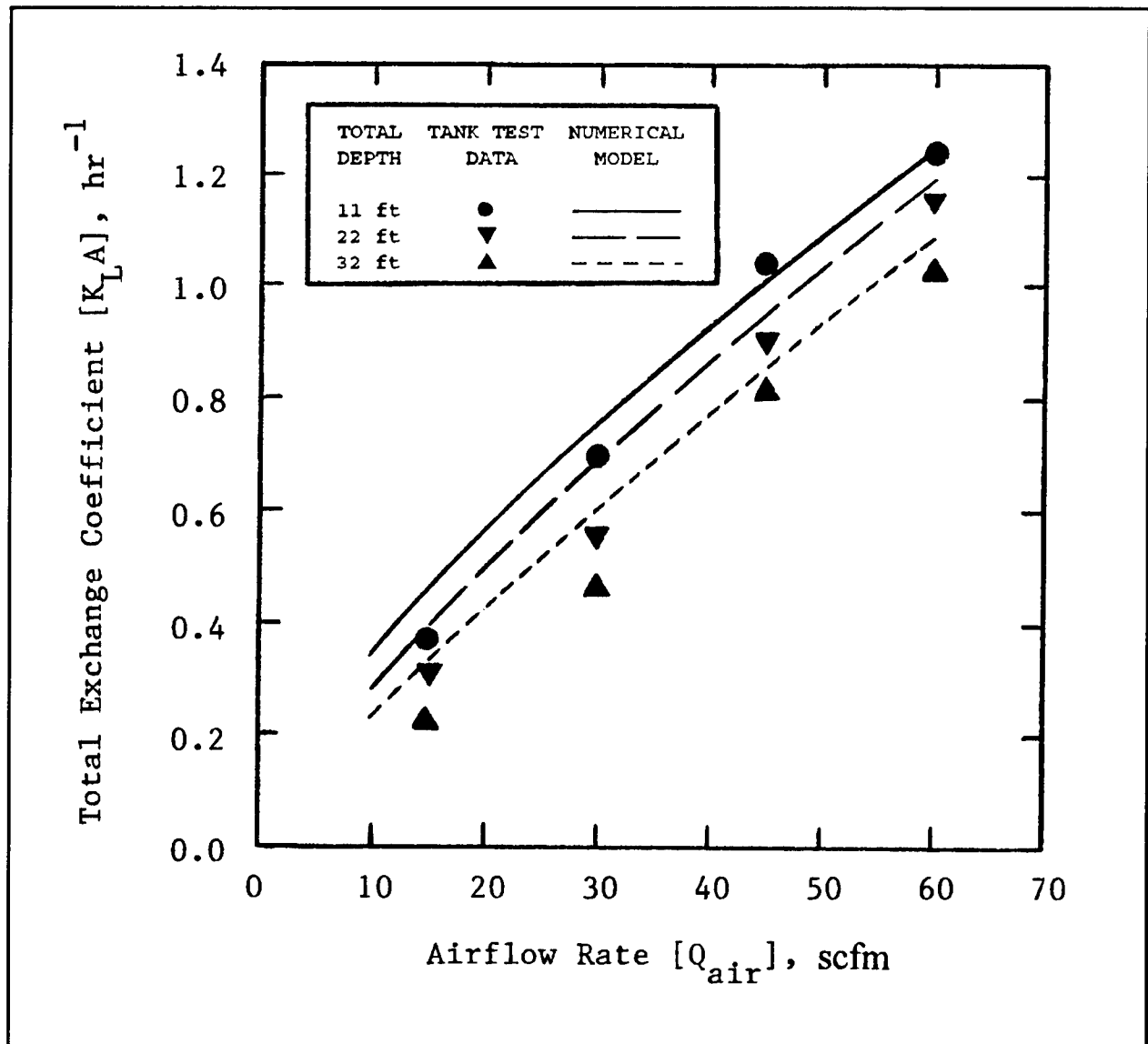
Figure 20.   Influence of airflow rate and total water depth of gas transfer in cylindrical tank
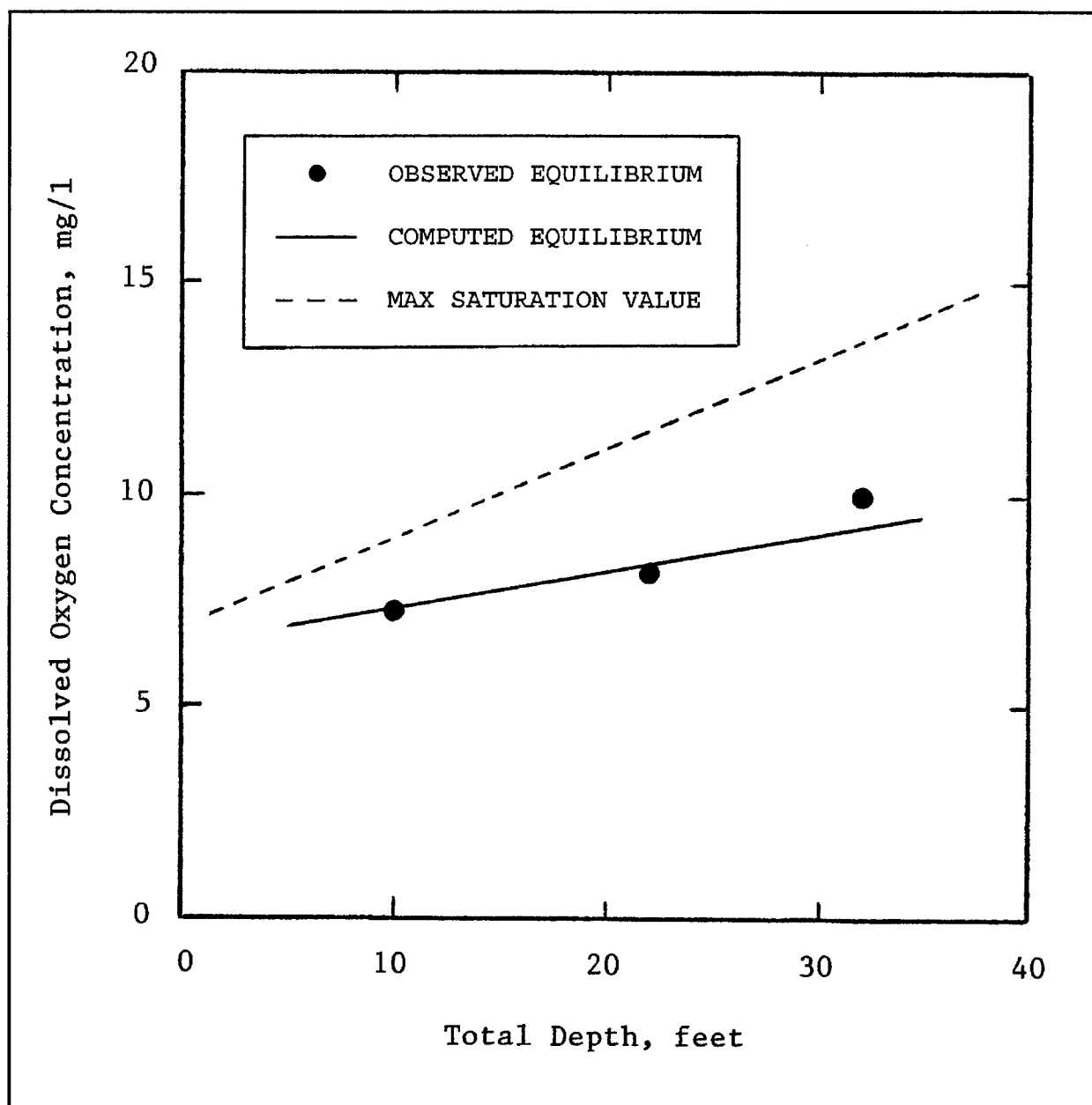
Figure 21. Variation of dissolved-oxygen concentration with total water depth in cylindrical tank
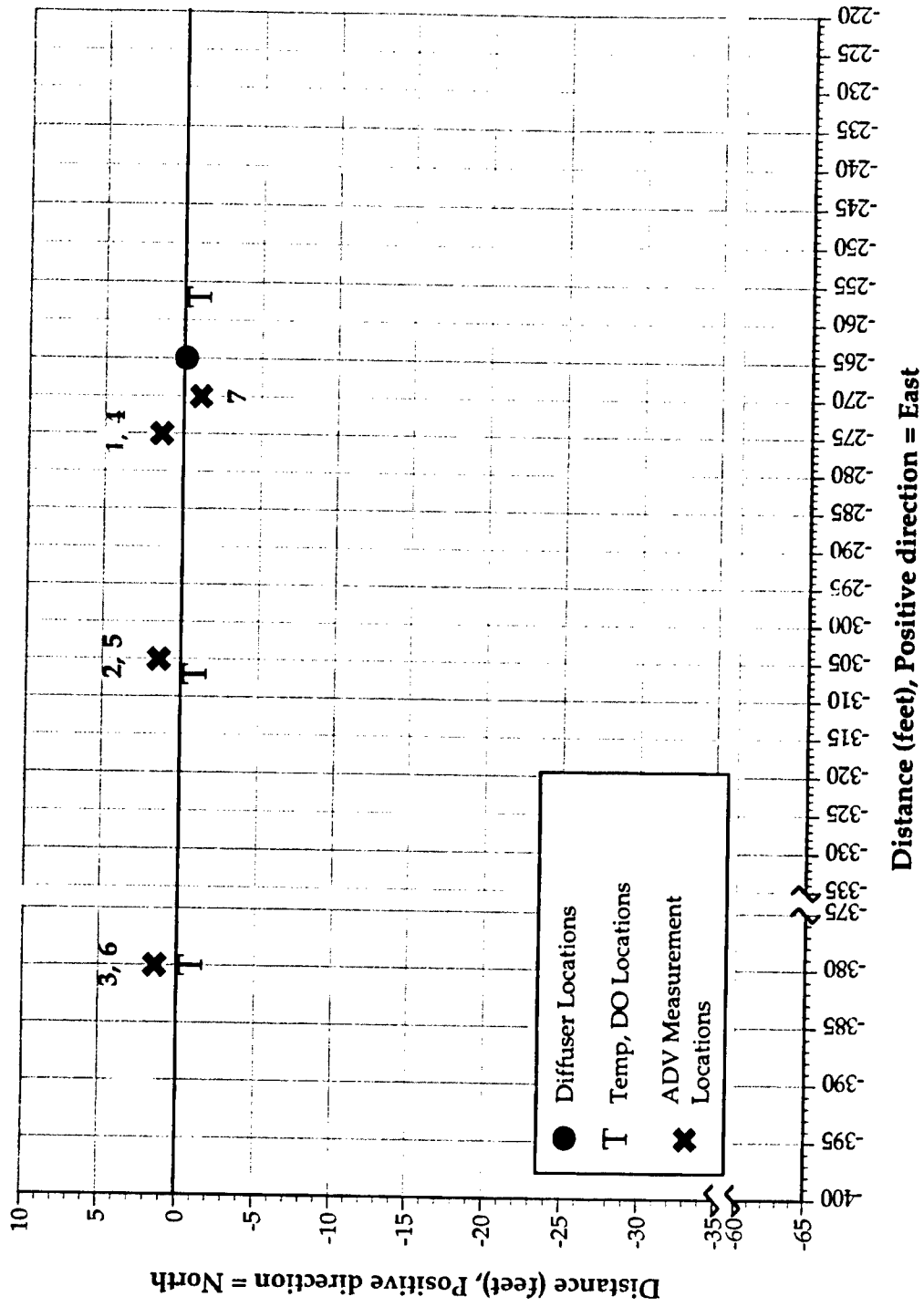
Figure 22. Experimental data stations for single-diffuser field test, Egan Quarry
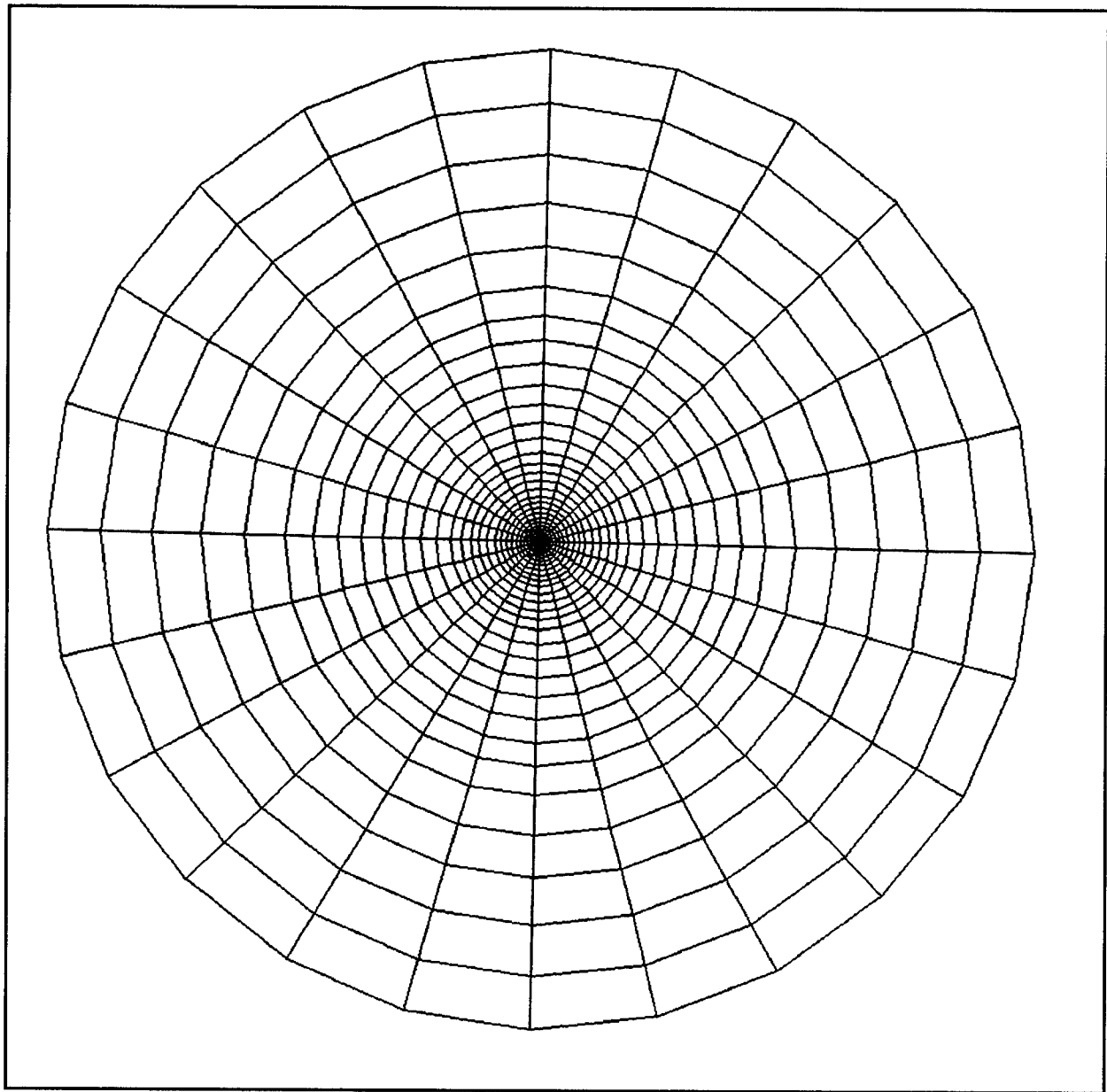
Figure 23. Full-plane computational grid for single-diffuser simulation, Egan Quarry
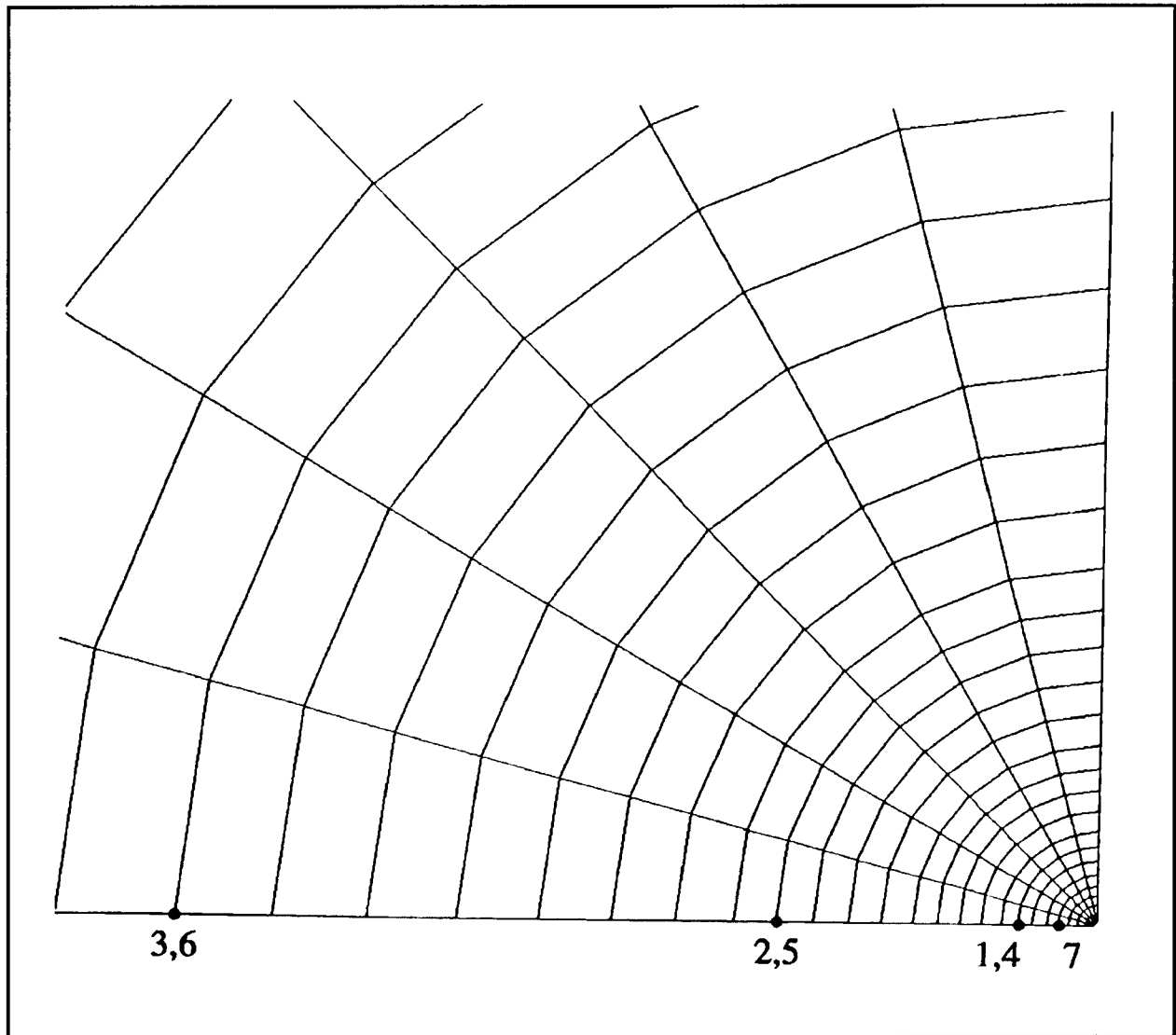
Figure 24. Grid detail with computational data stations for single-diffuser simulation
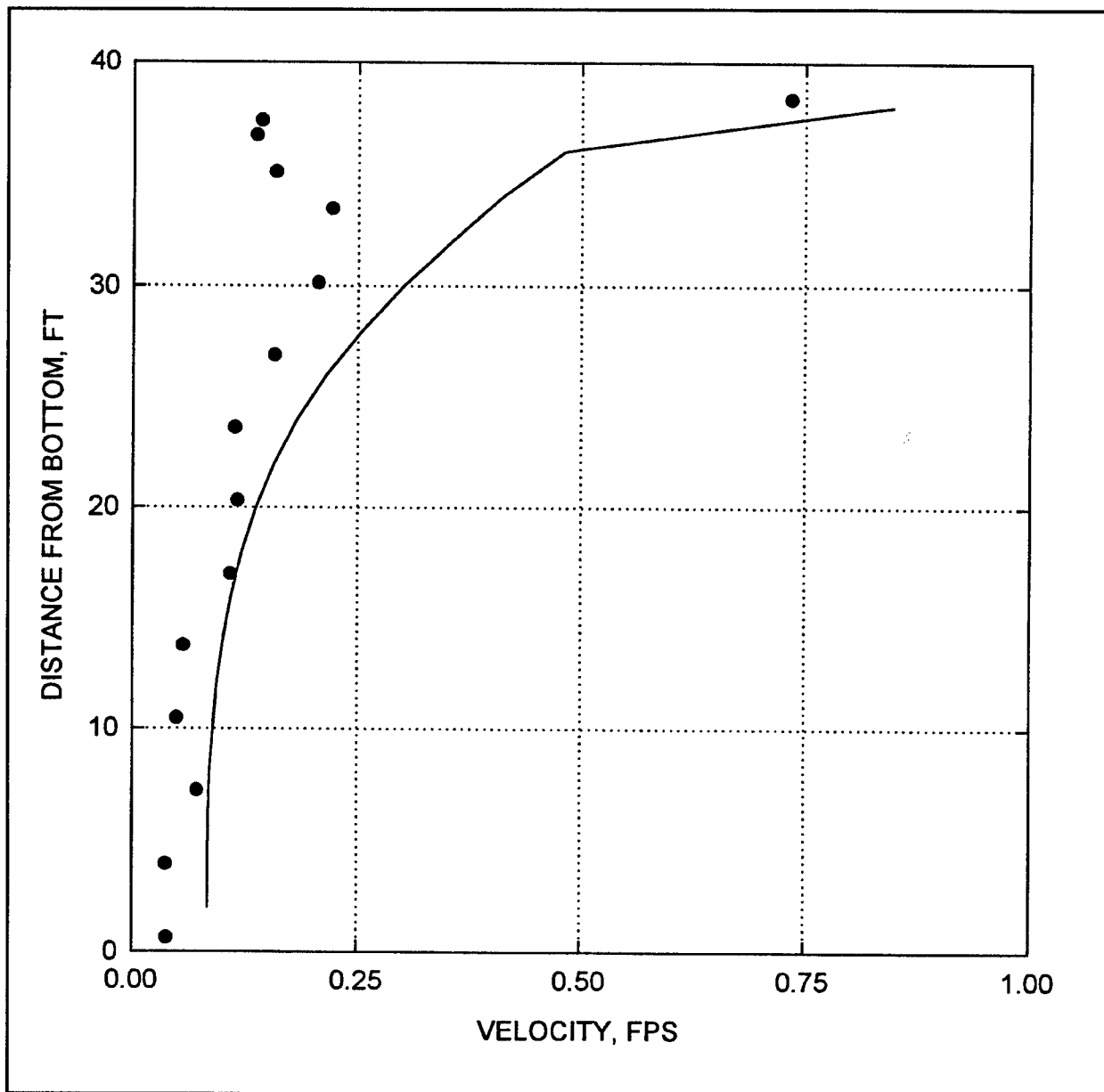
Figure 25. Predicted velocity magnitude (—) and 46-scfm experimental data (●) for single-diffuser test, Egan Quarry, Station 7
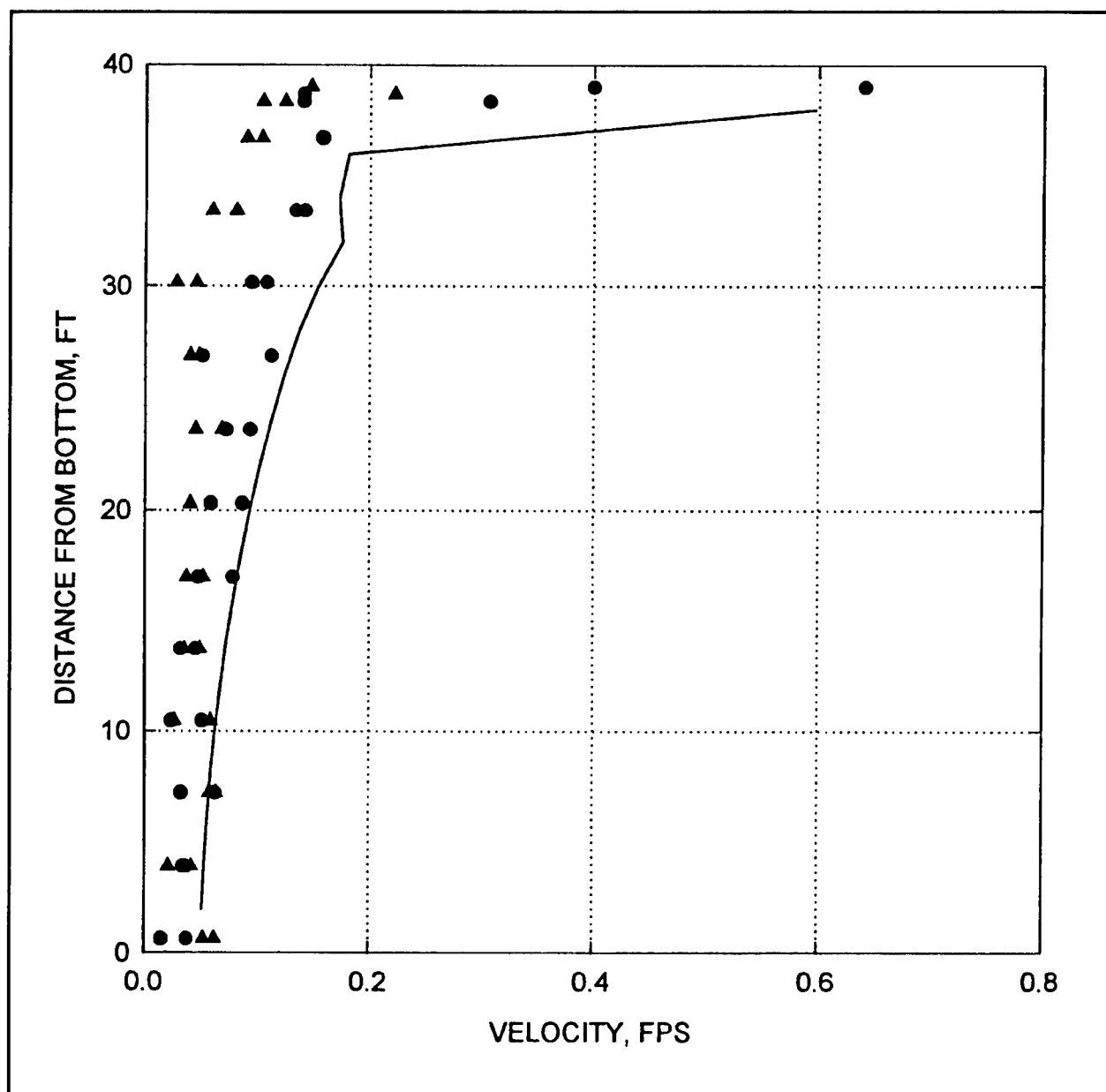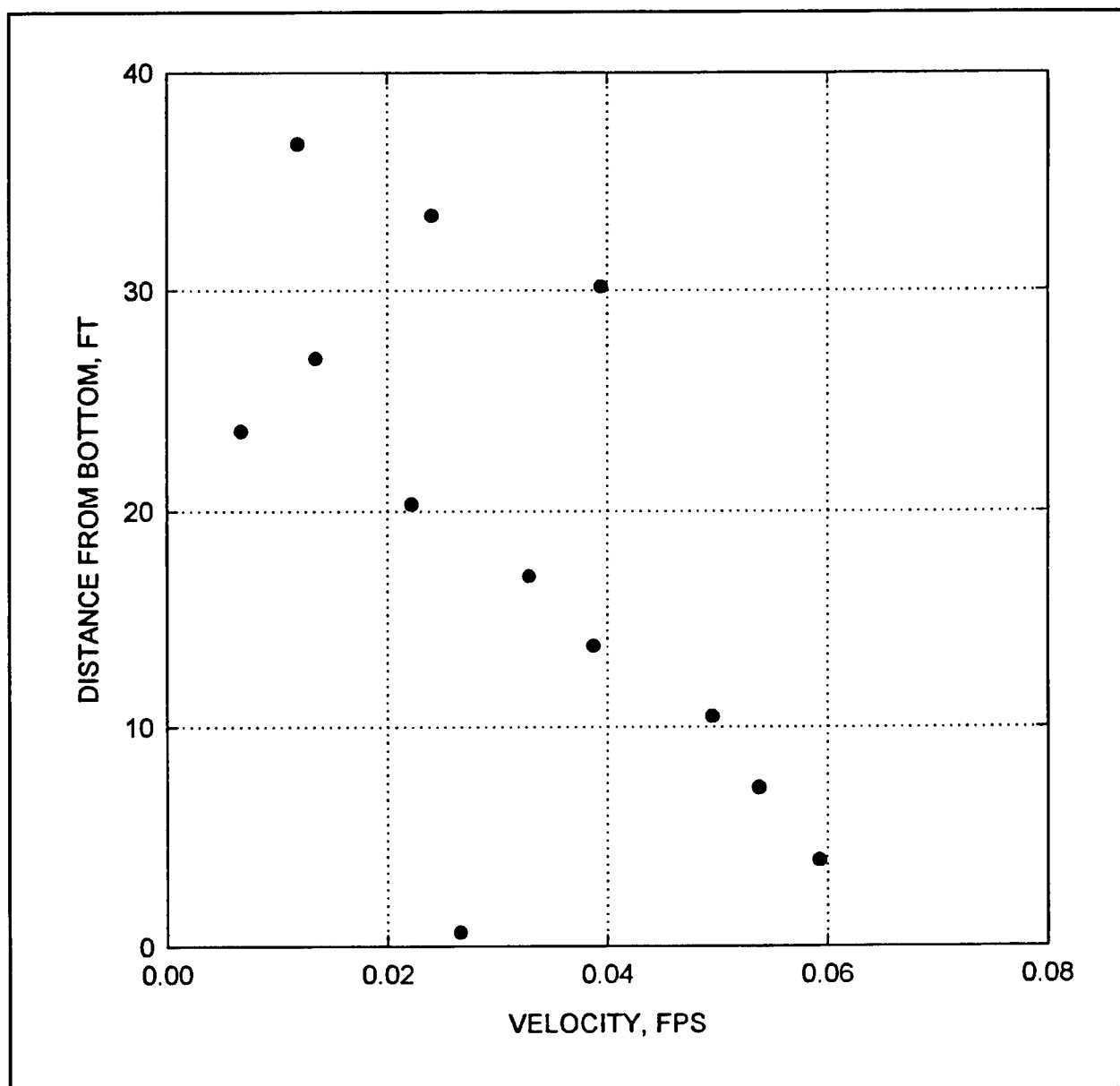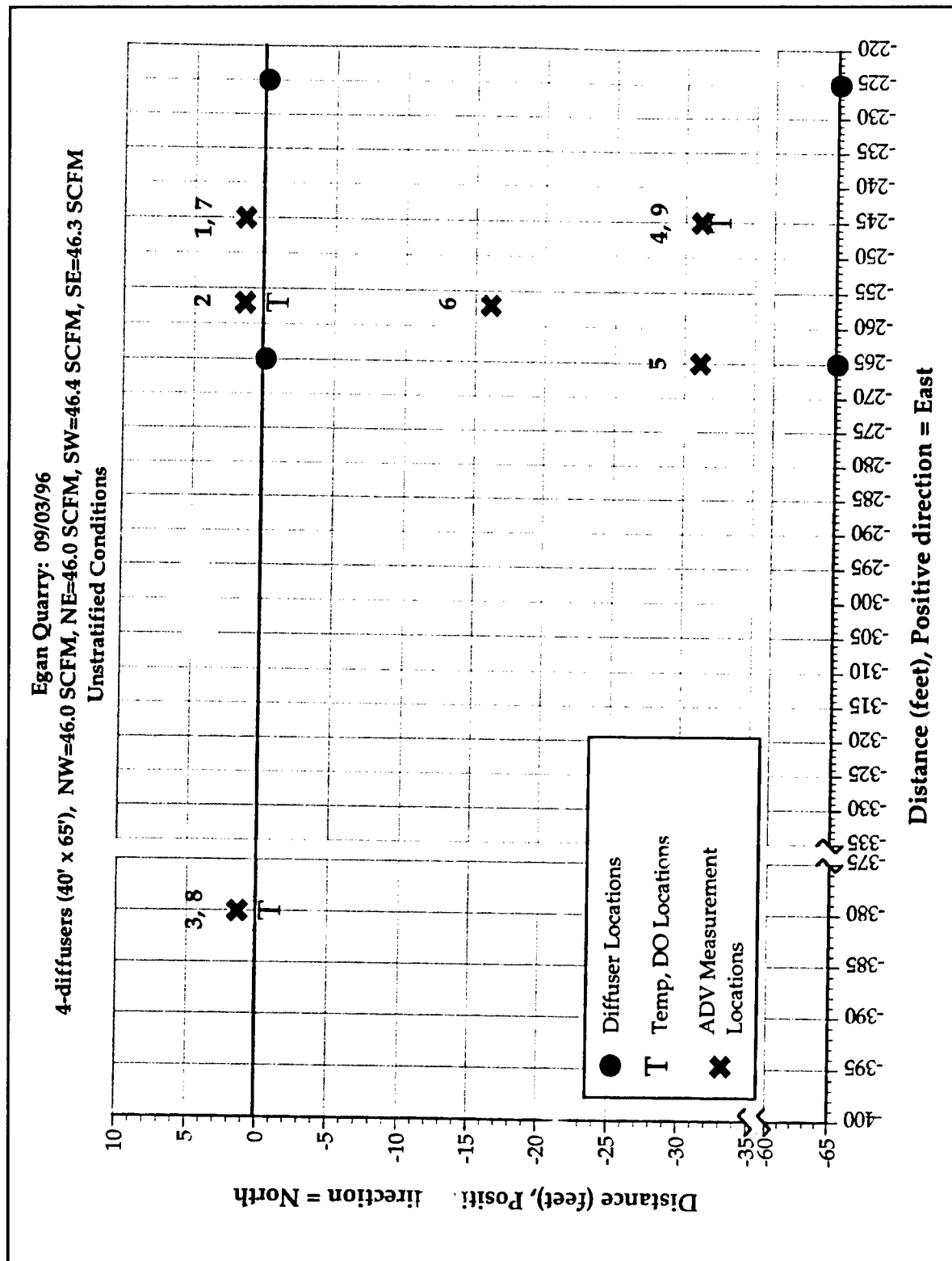
Figure 26. Predicted velocity magnitude (—), 46-scfm experimental data (●), and rescaled 23.9-scfm experimental data (▲) for single-diffuser-test, Egan Quarry, Stations 1, 4
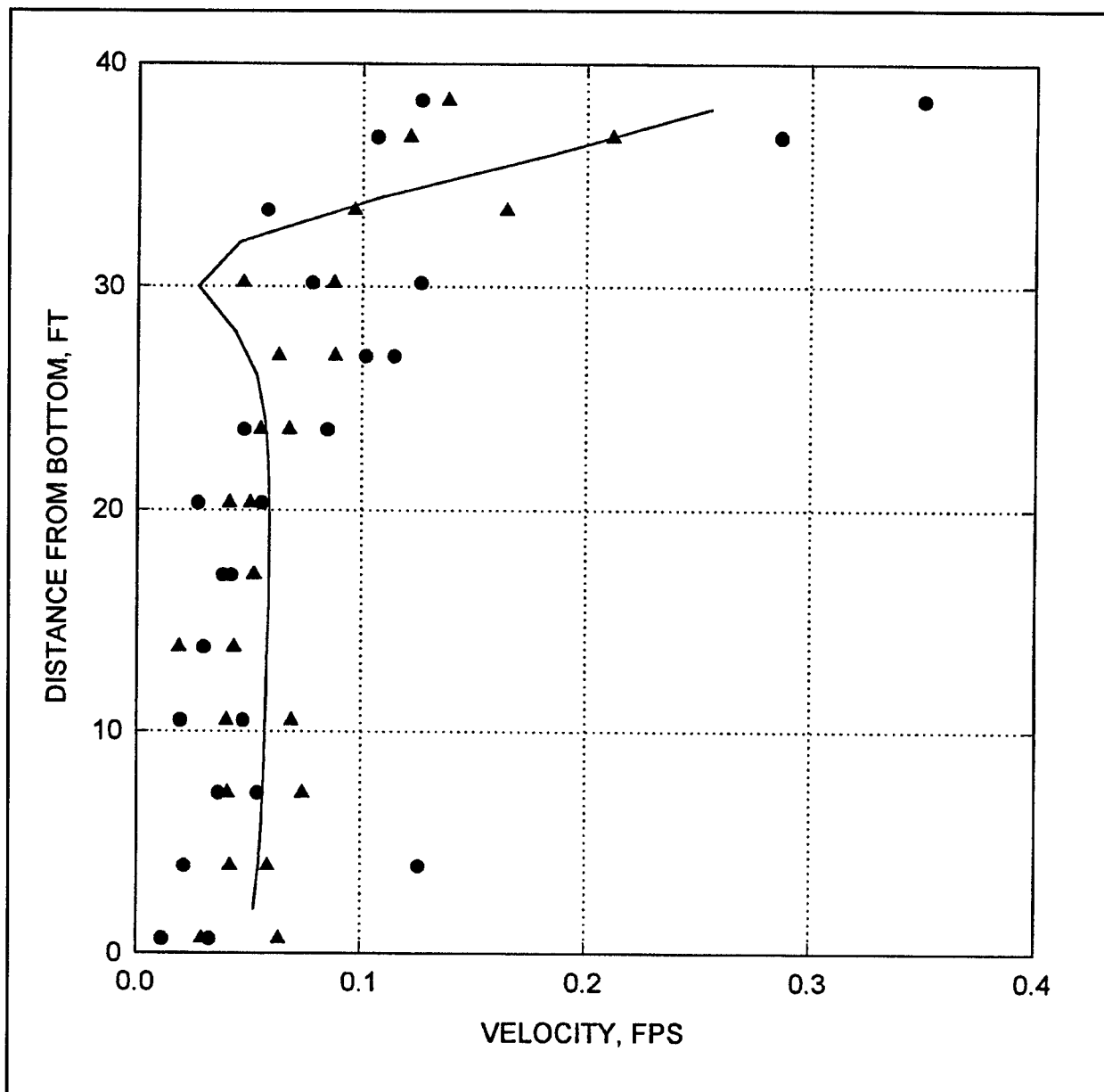
Figure 27. Predicted velocity magnitude (—), 46-scfm experimental data (●), and rescaled 23.9-scfm experimental data (▲) for single-diffuser-test, Egan Quarry, Stations 2, 5
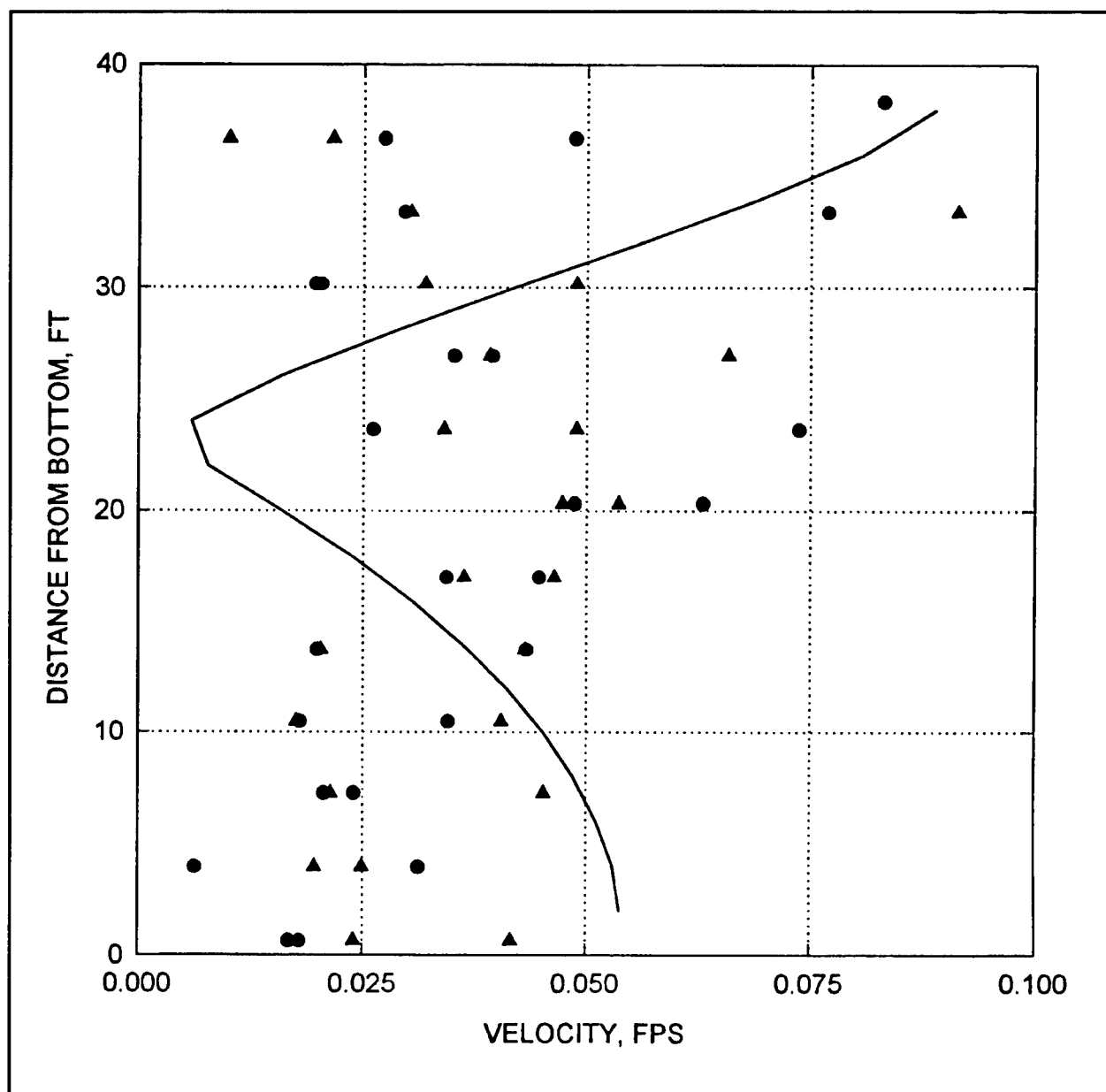
Figure 28.   Predicted velocity magnitude (—), 46-scfm experimental data (●), and rescaled 23.9-scfm experimental data (▲) for single-diffuser test, Egan Quarry, Stations 3, 6
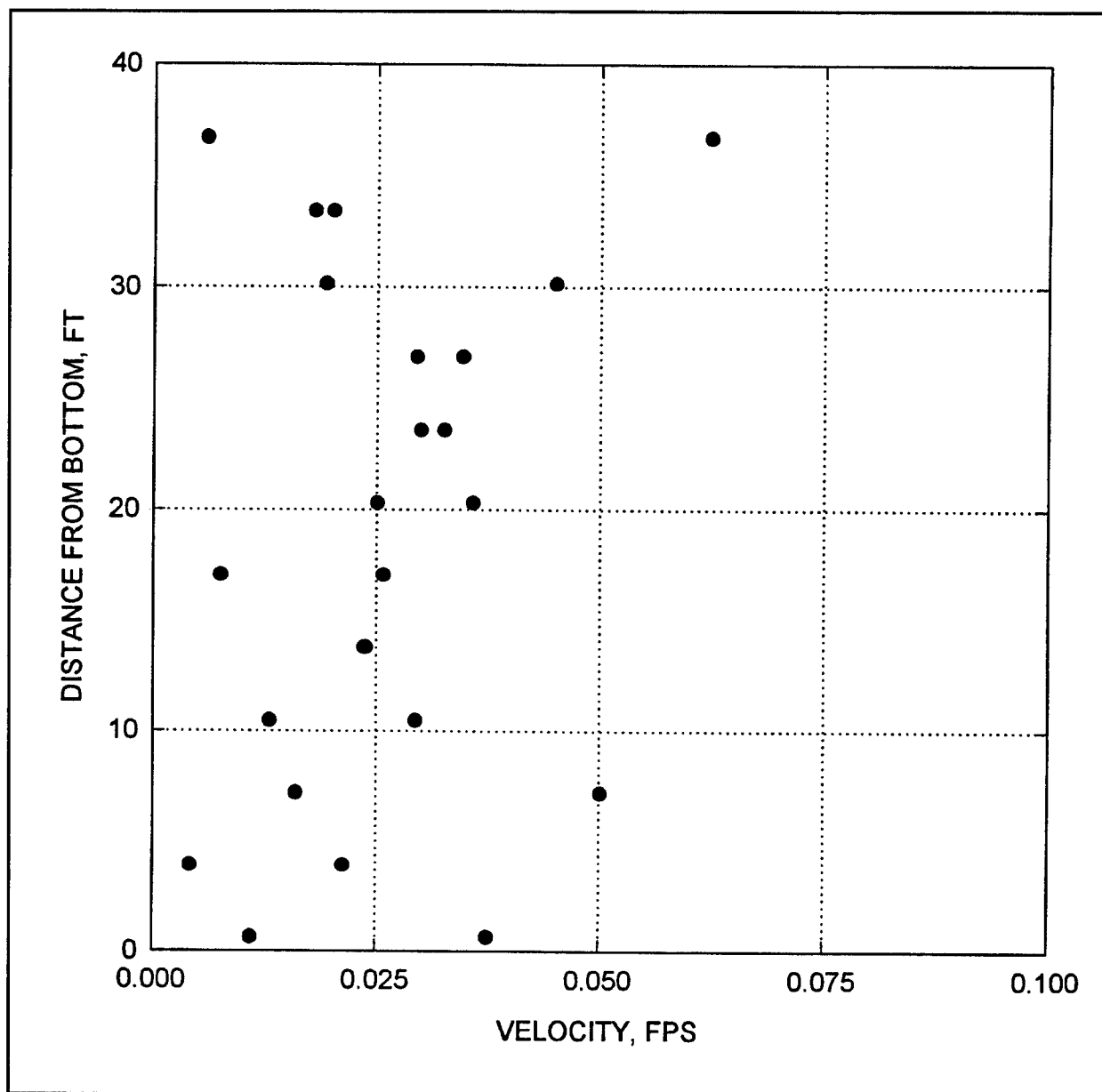
Figure 29.   Background velocity magnitude (●) for single-diffuser tests (no airflow)
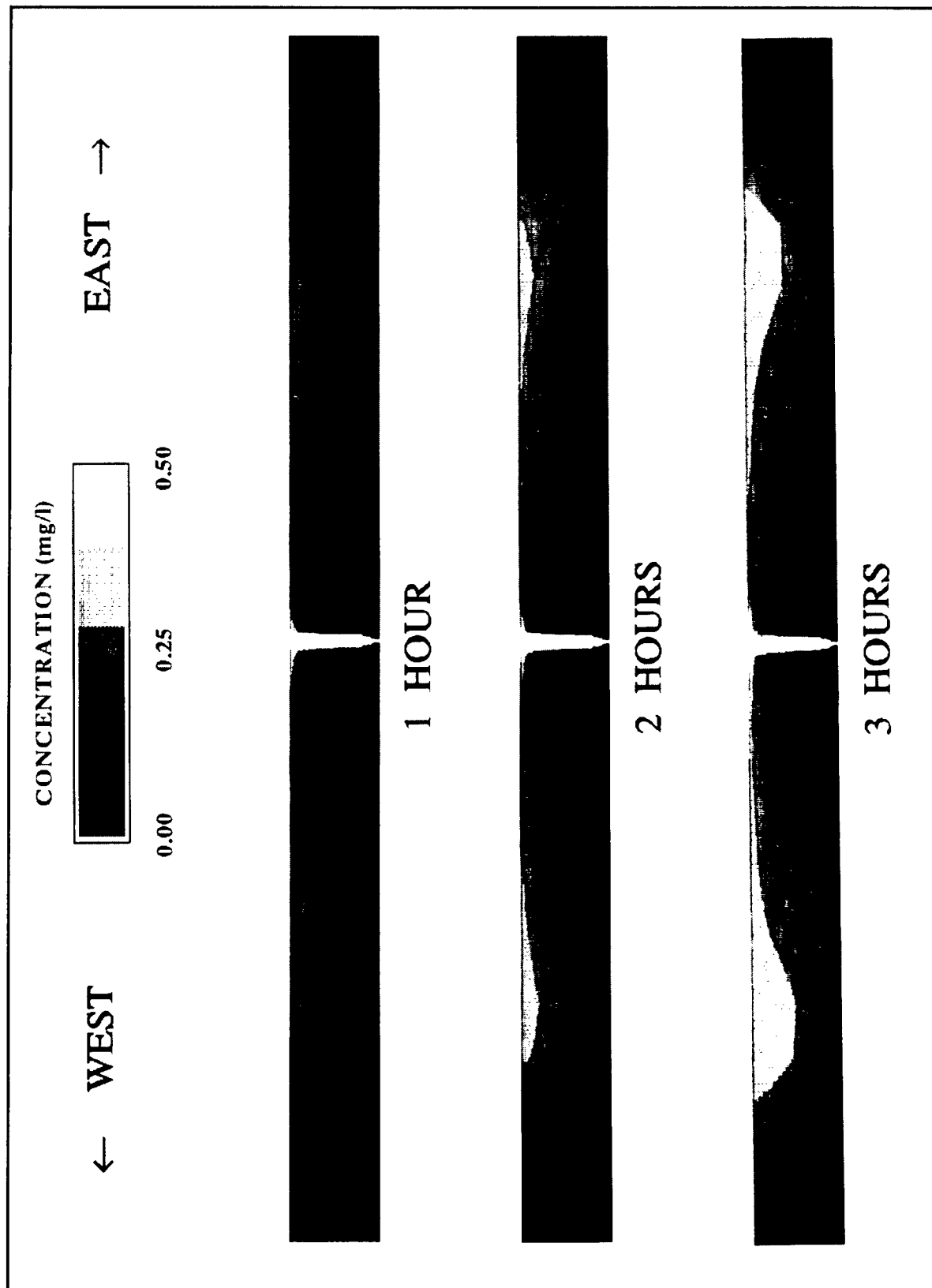
Figure 30.   Predicted concentration of dissolved oxygen for single diffuser in Egan Quarry with initial condition assumed anaerobic
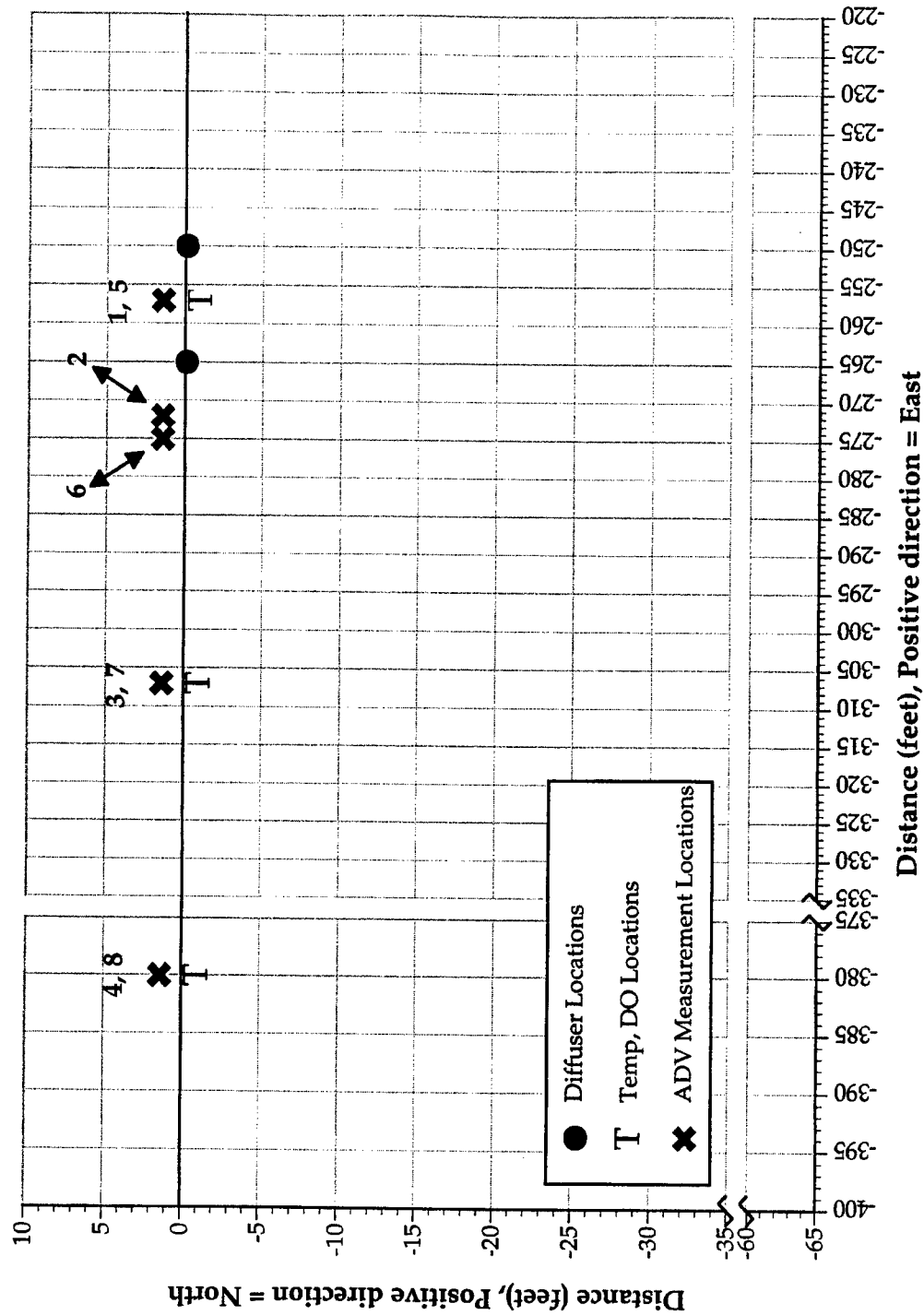
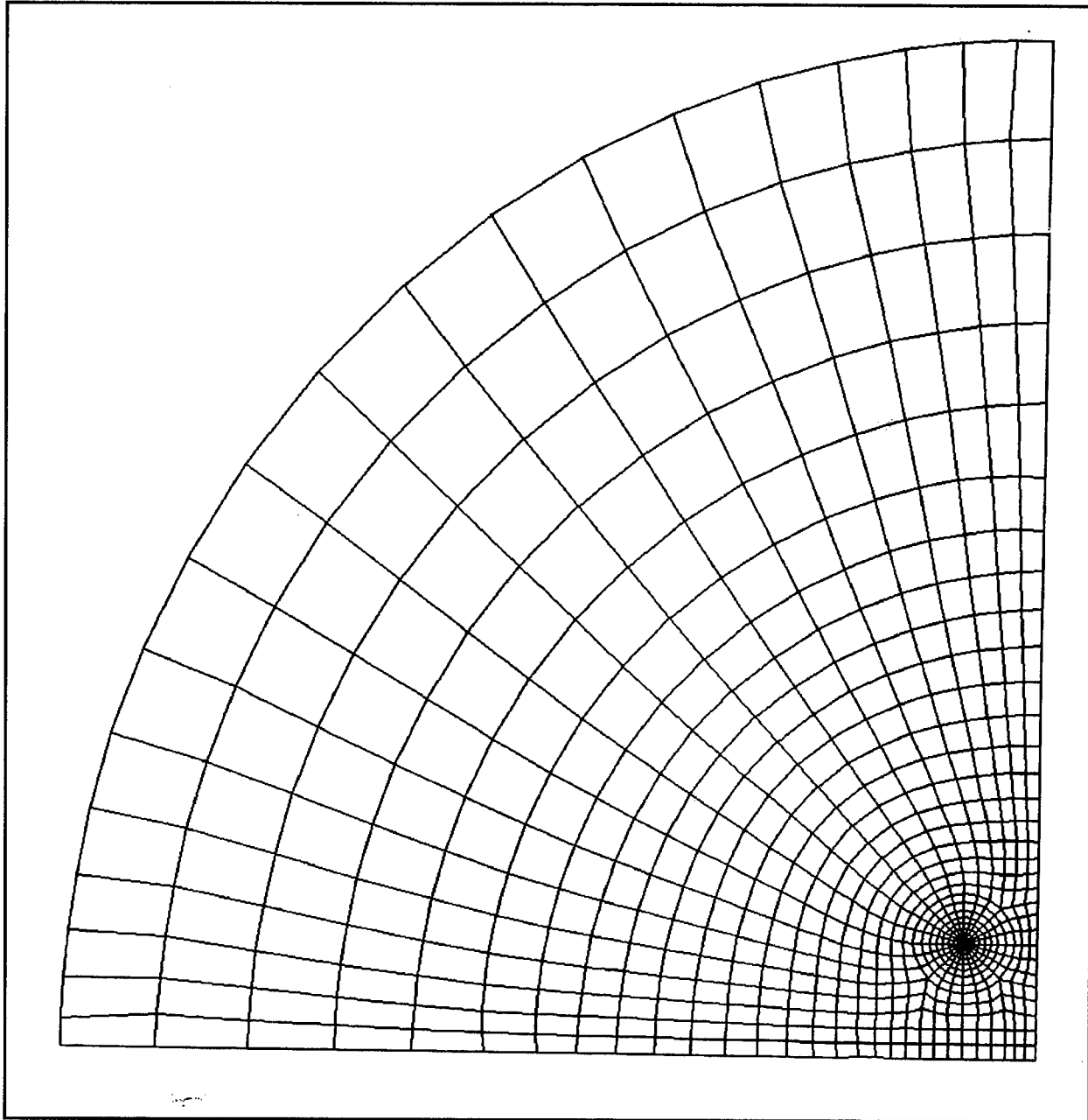Figure 31. Experimental data stations for two-diffuser field test, 15-ft spacing, Egan Quarry
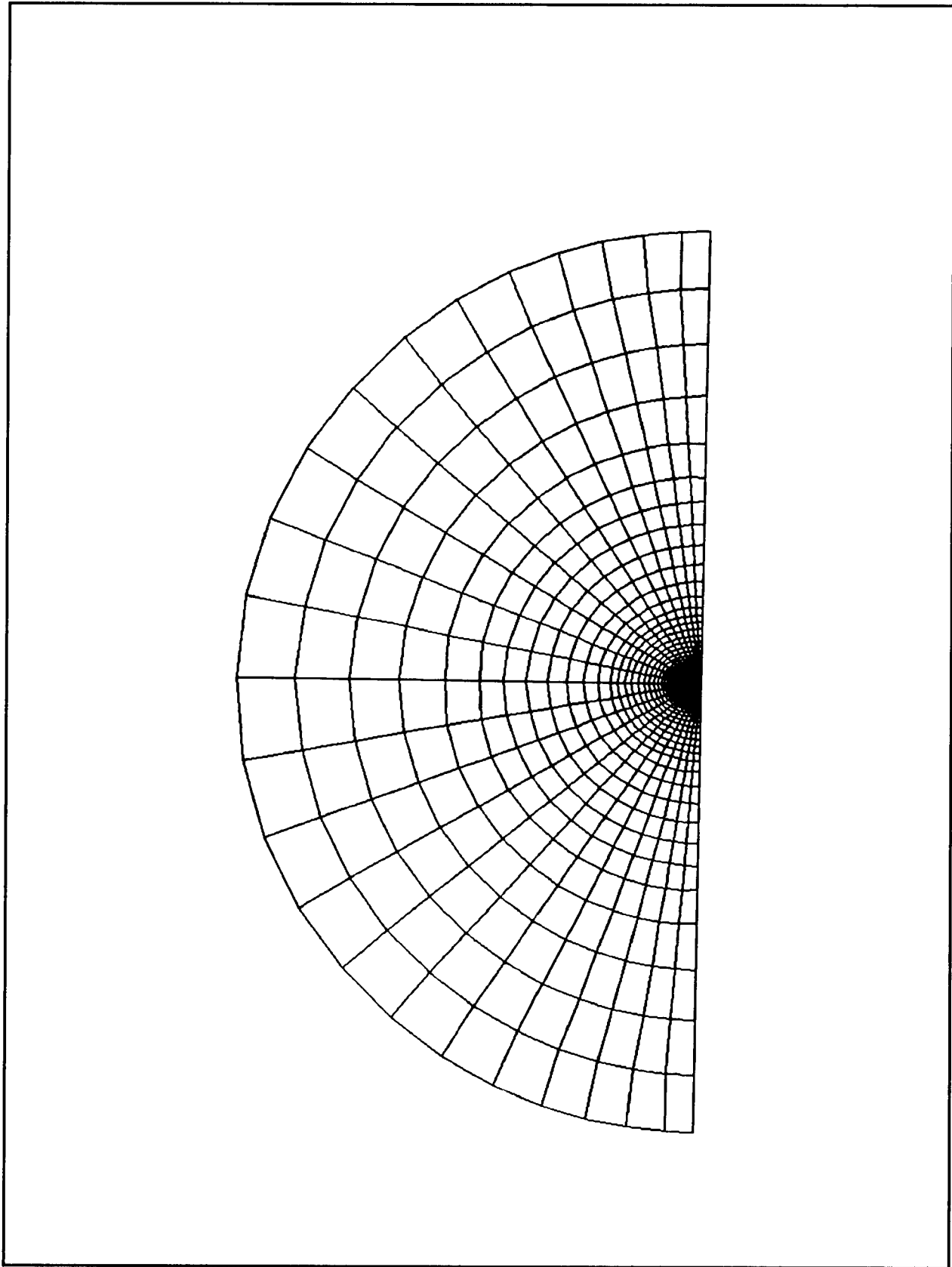
Figure 32. Half-plane computational grid for two-diffuser simulation, 15-ft spacing, Egan Quarry
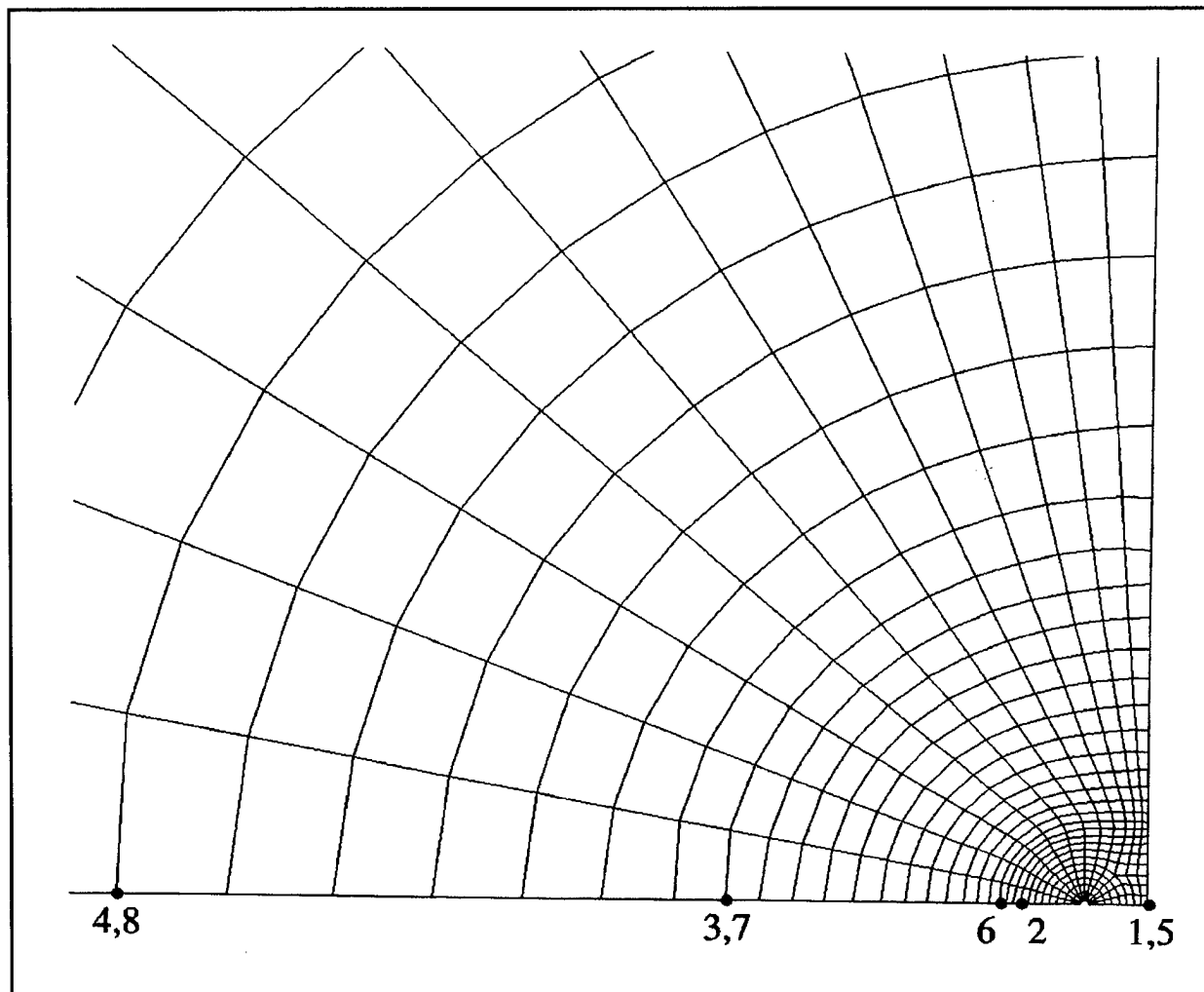
Figure 33. Grid detail with computational data stations for two-diffuser simulation, 15-ft spacing
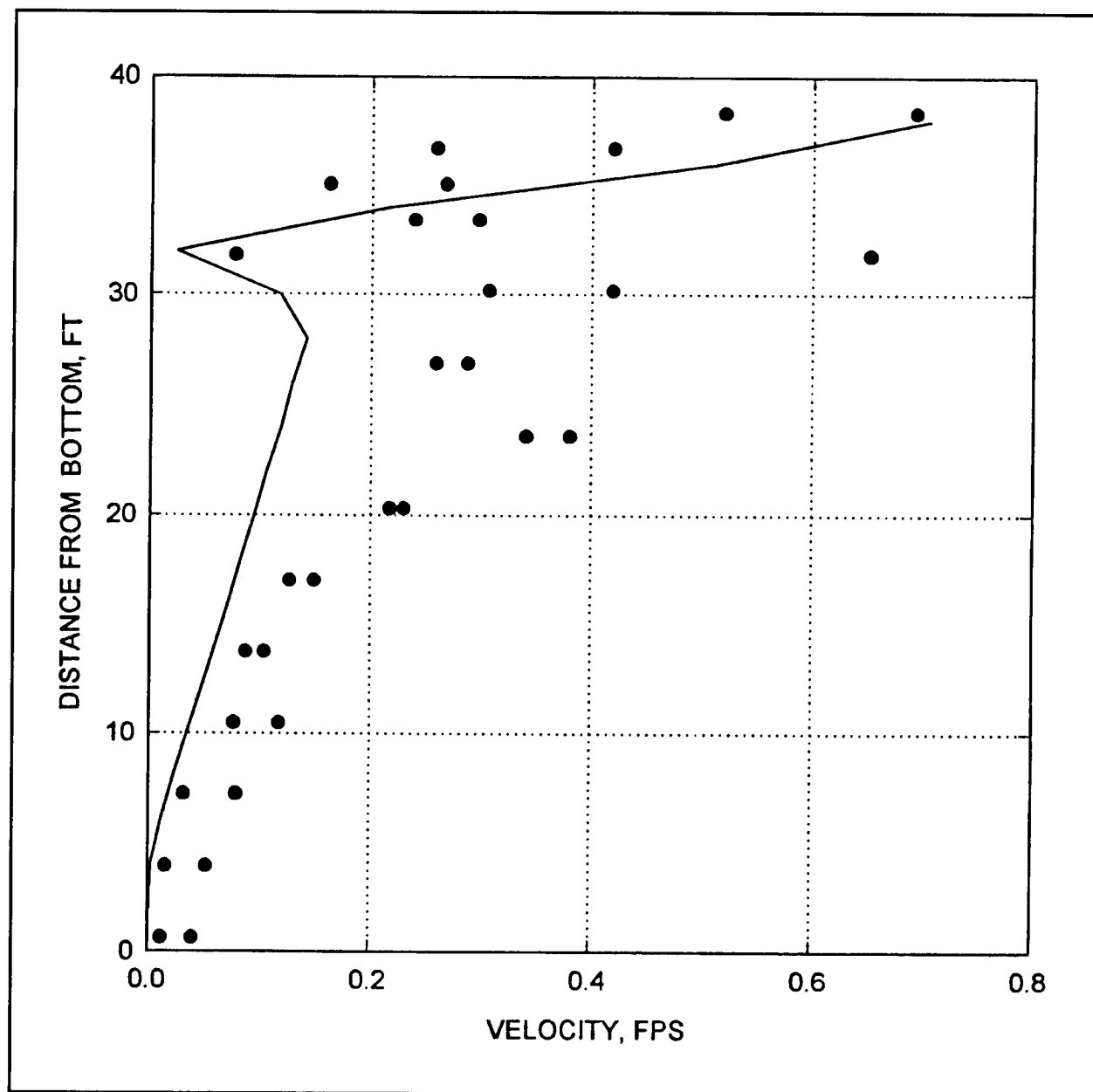
Figure 34. Predicted velocity magnitude (—) and 46-scfm experimental data (●) for two-diffuser test
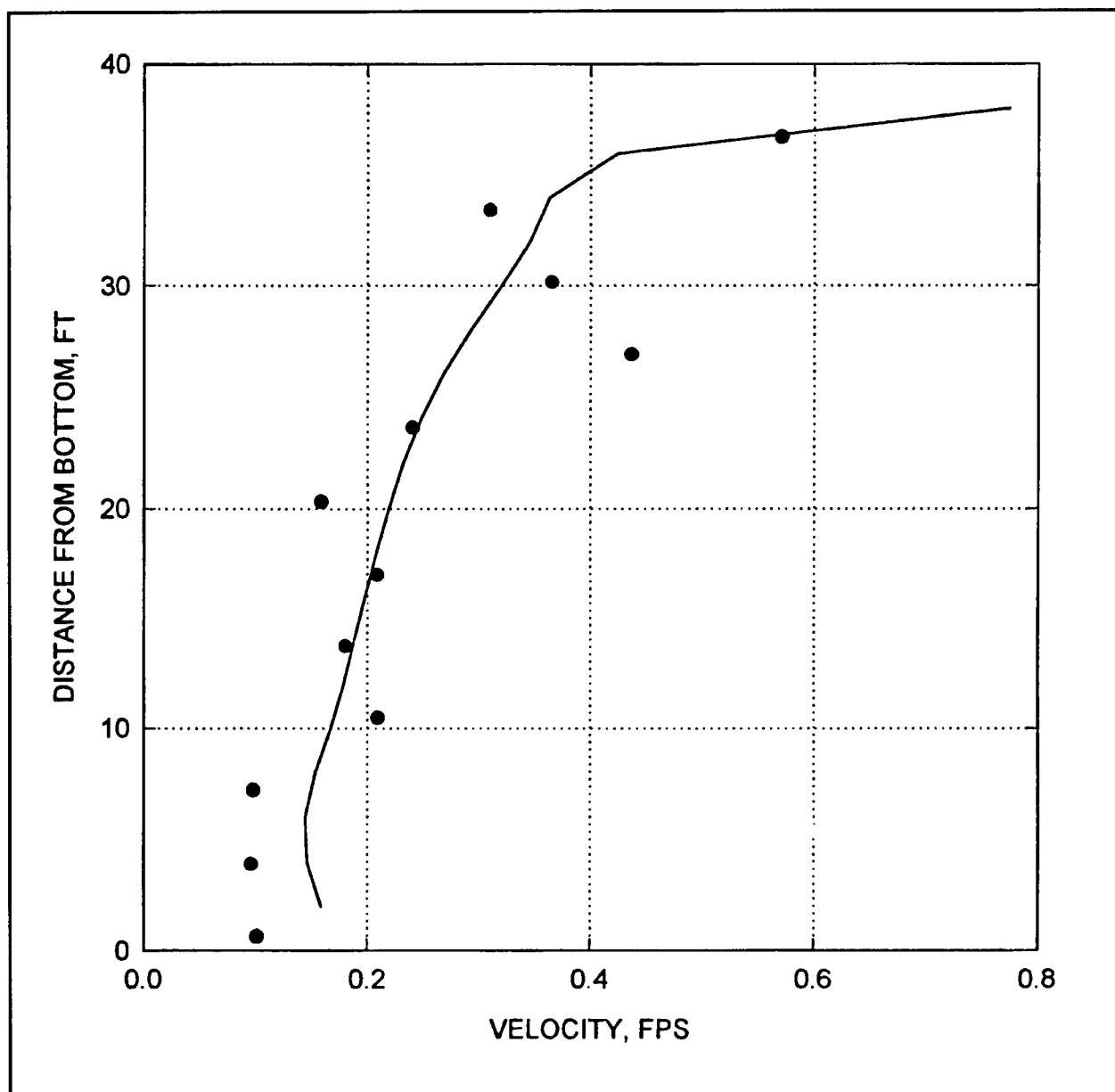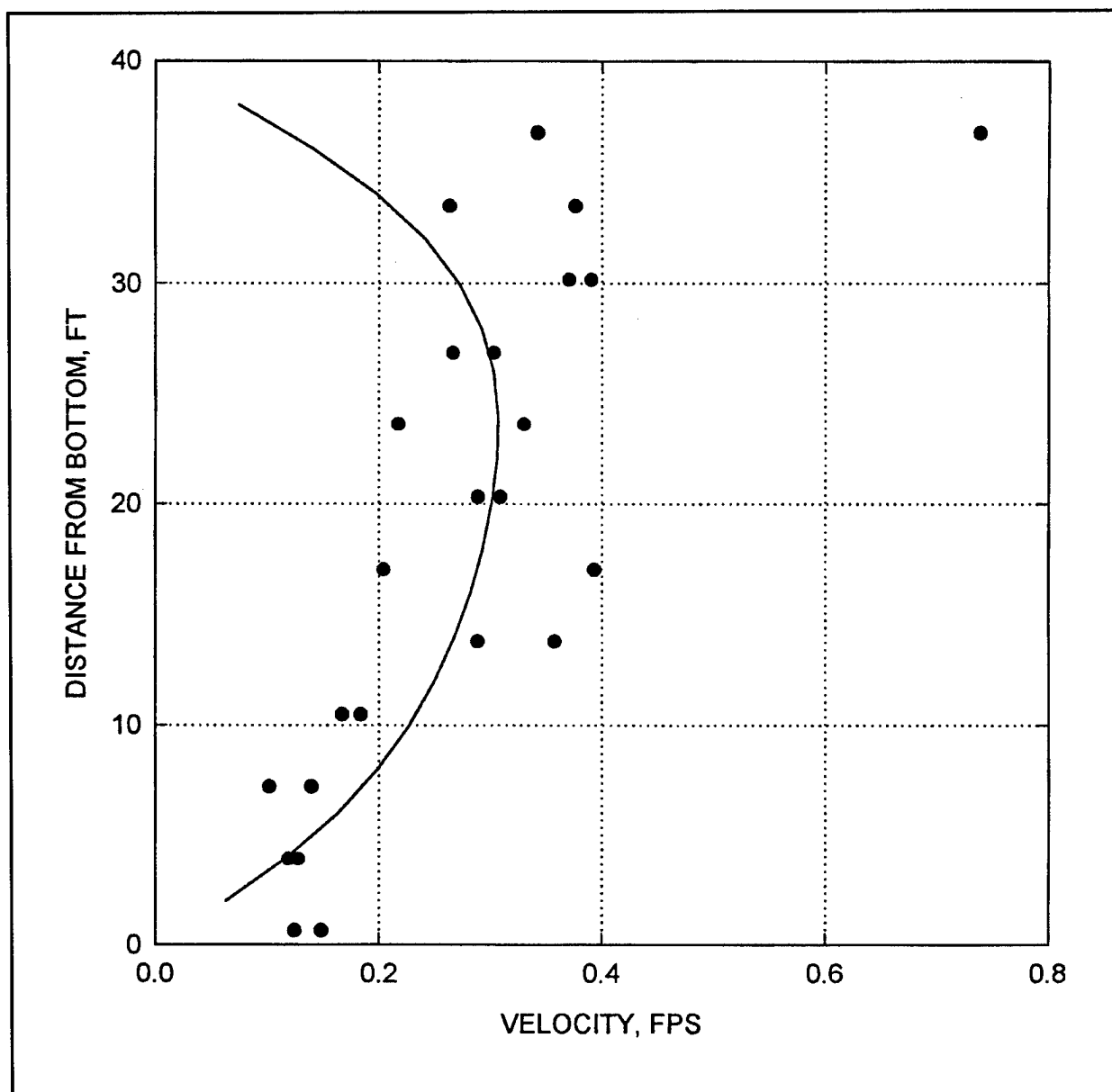with 15-ft spacing, Egan Quarry, Stations 1, 5
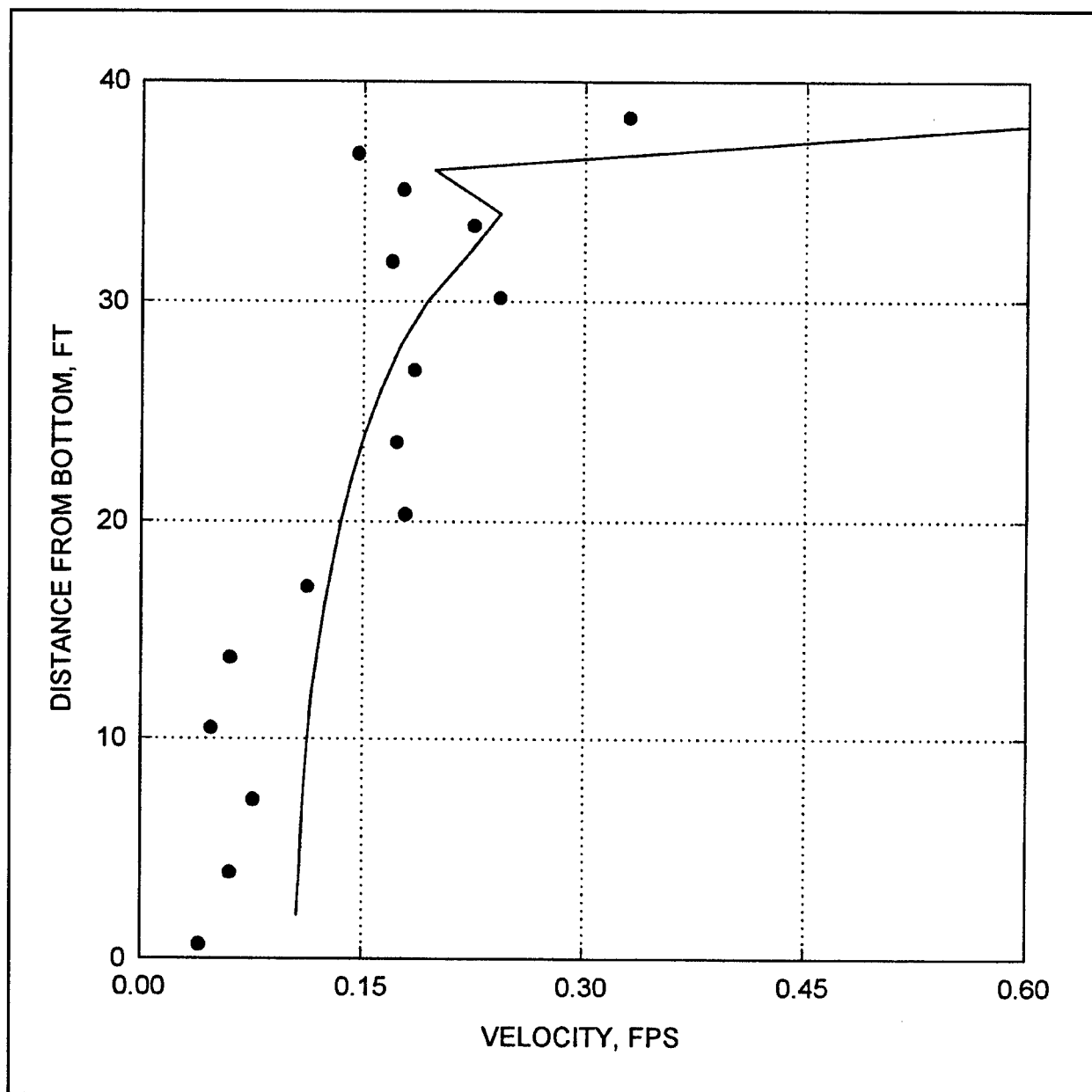
Figure 35. Predicted velocity magnitude (—) and 46-scfm experimental data (●) for two-diffuser test with 15-ft spacing, Egan Quarry, Station 2
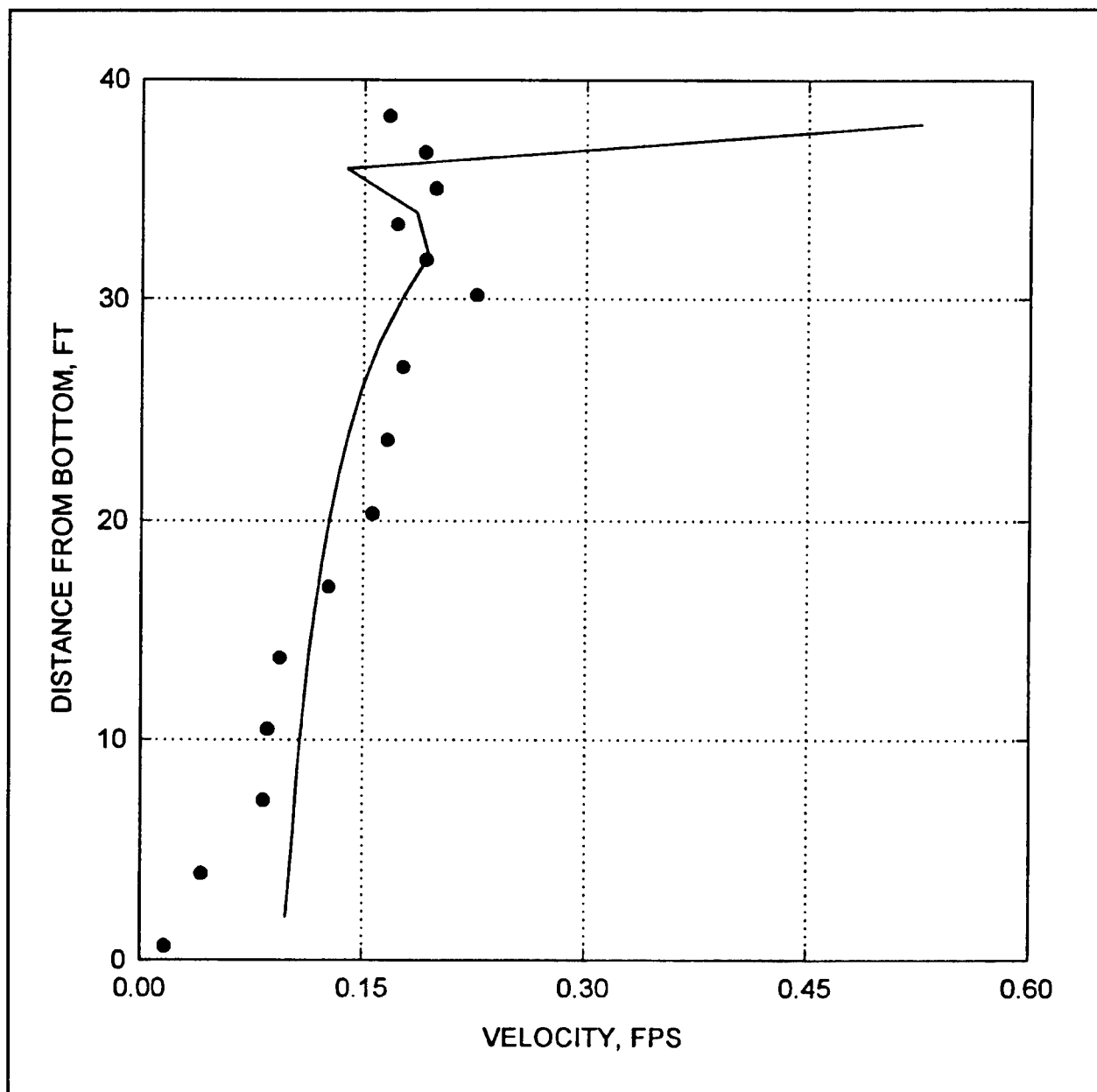
Figure 36. Predicted velocity magnitude (—) and 46-scfm experimental data (●) for two-diffuser test with 15-ft spacing, Egan Quarry, Station 6
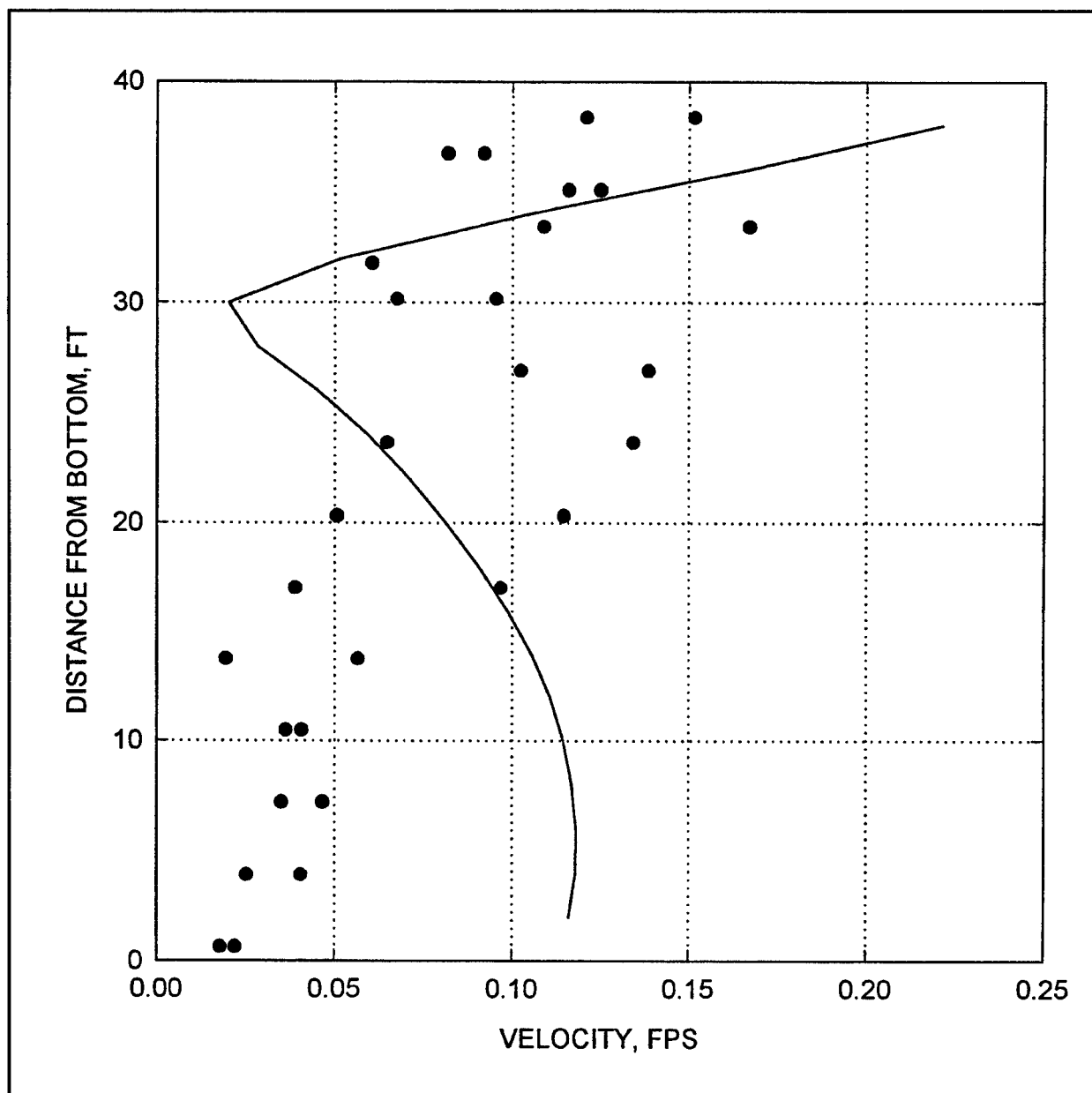
Figure 37. Predicted velocity magnitude (—) and 46-scfm experimental data (●) for two-diffuser test with 15-ft spacing, Egan Quarry, Stations 3, 7
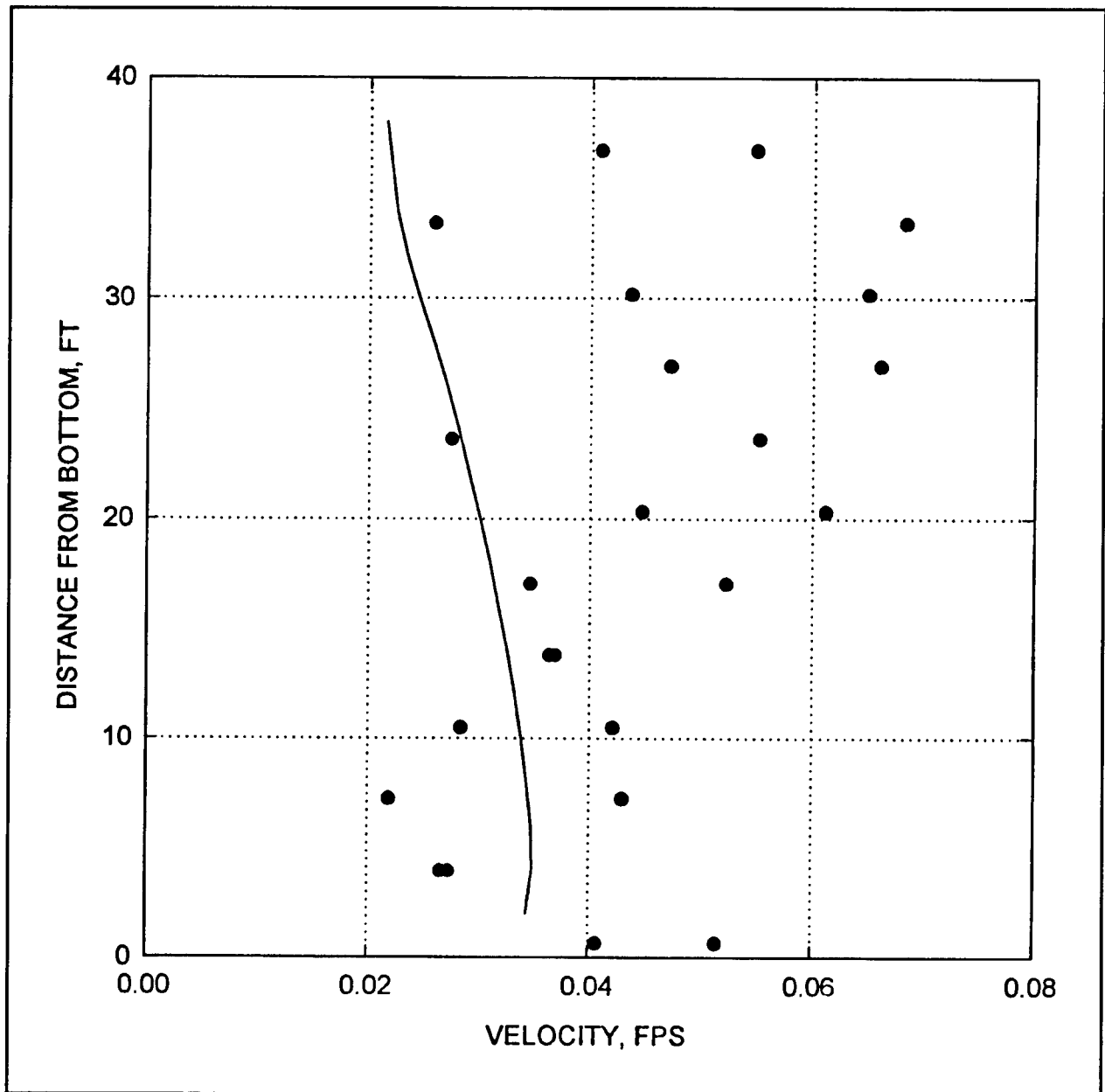
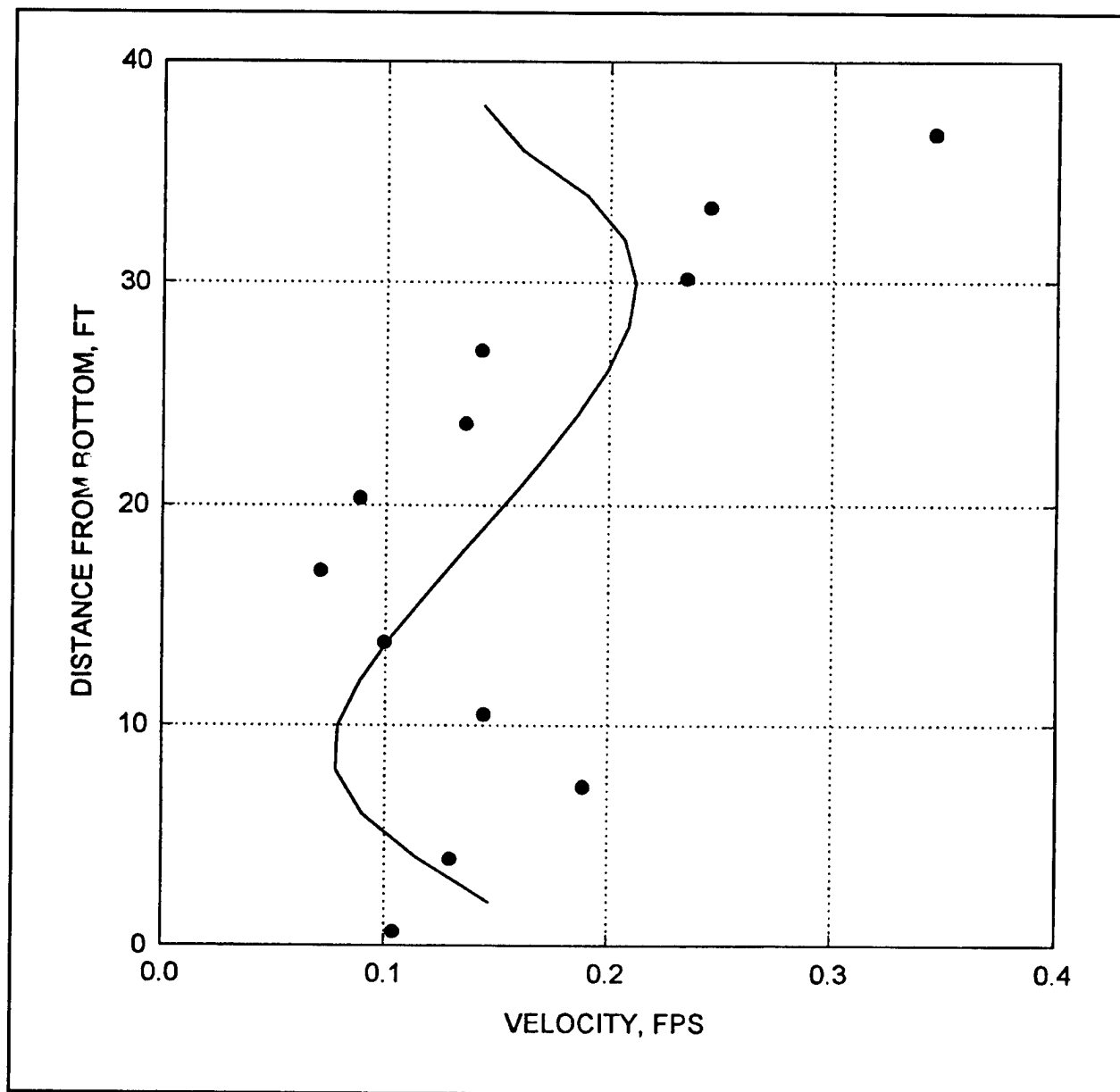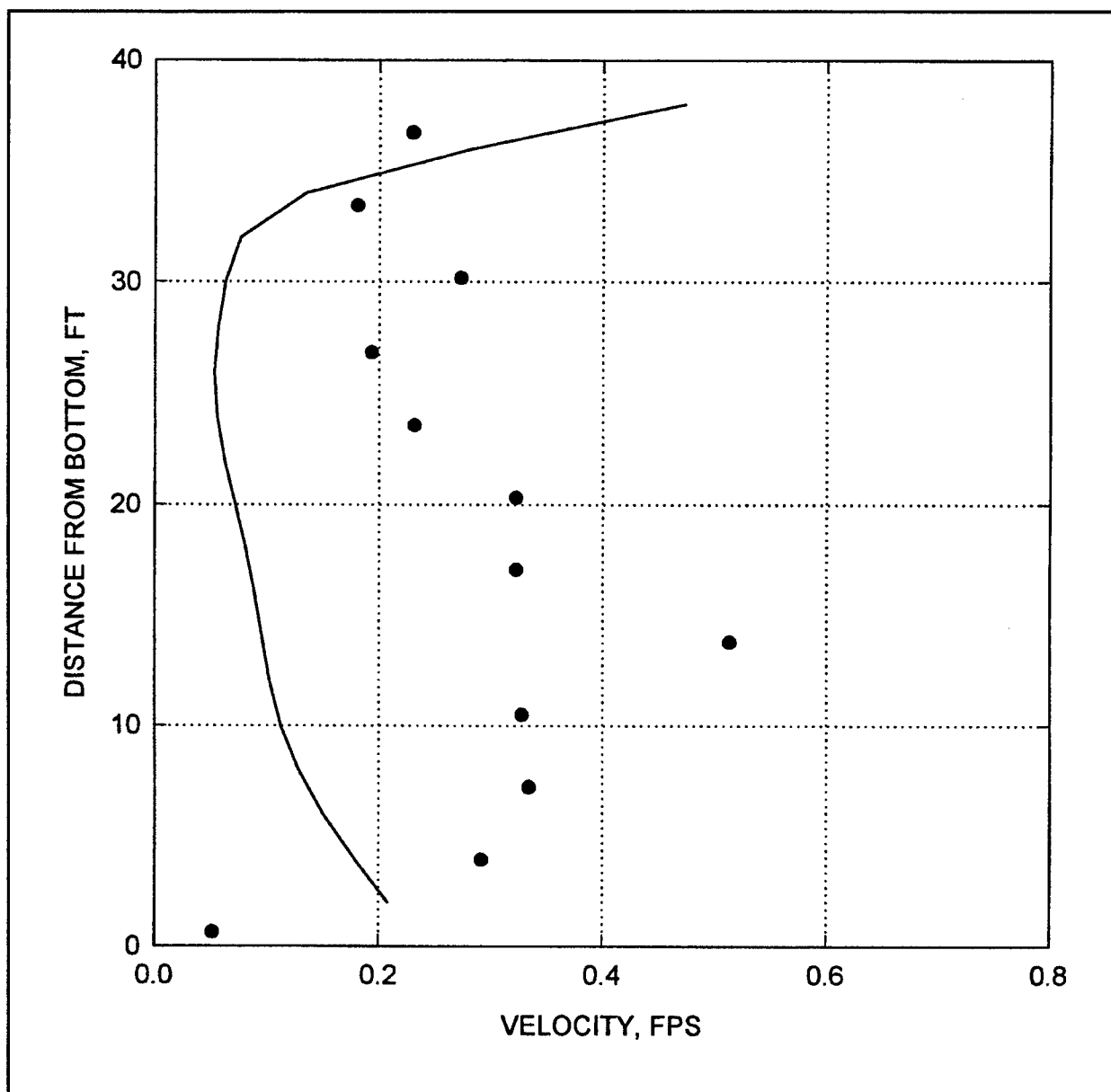Figure 38. Predicted velocity magnitude (—) and 46-scfm experimental data (●) for two-diffuser test with 15-ft spacing, Egan Quarry, Stations 4, 8
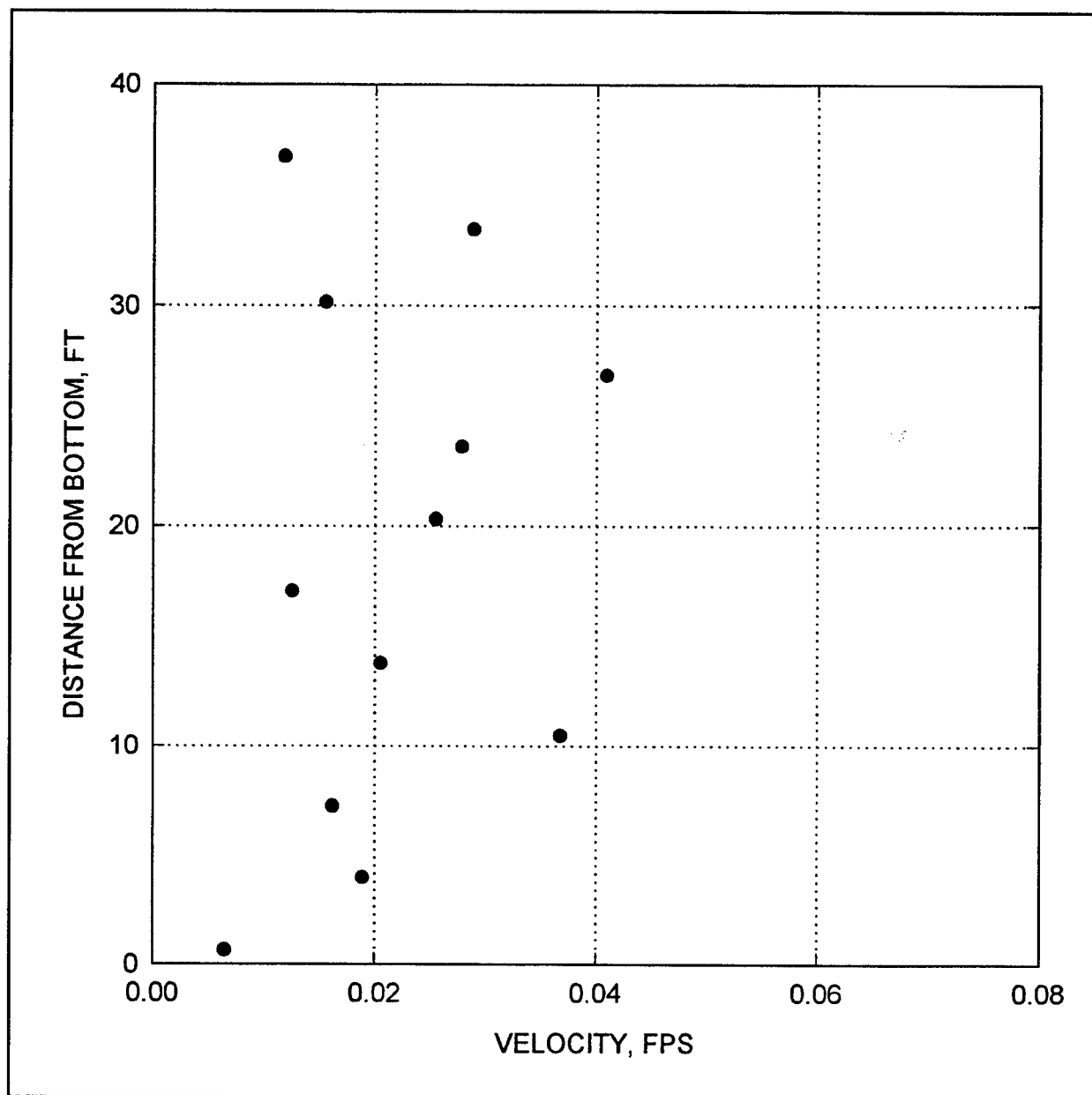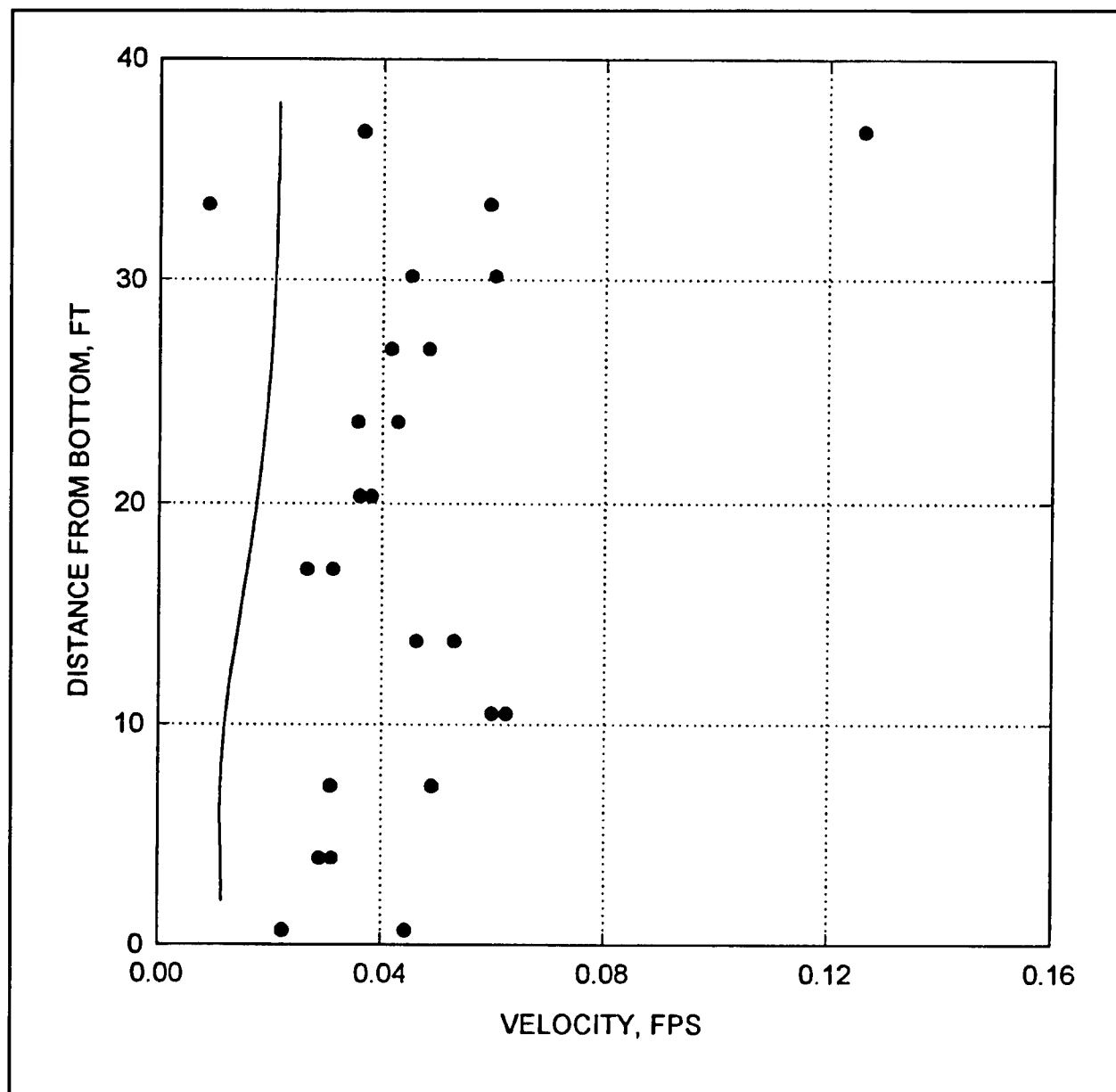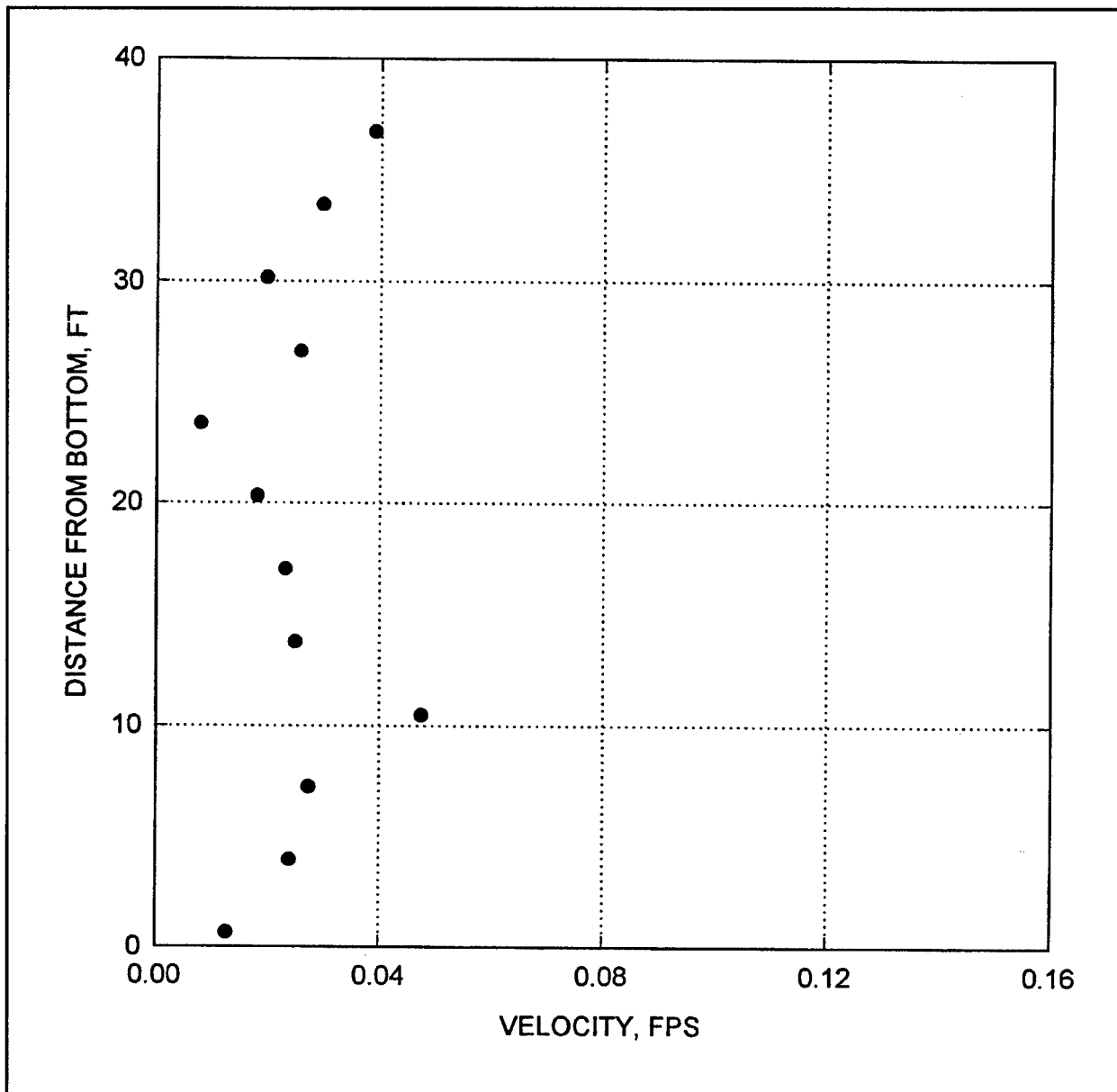
Figure 39. Background velocity magnitude (●) for two-diffuser test, 15-ft spacing (no airflow)
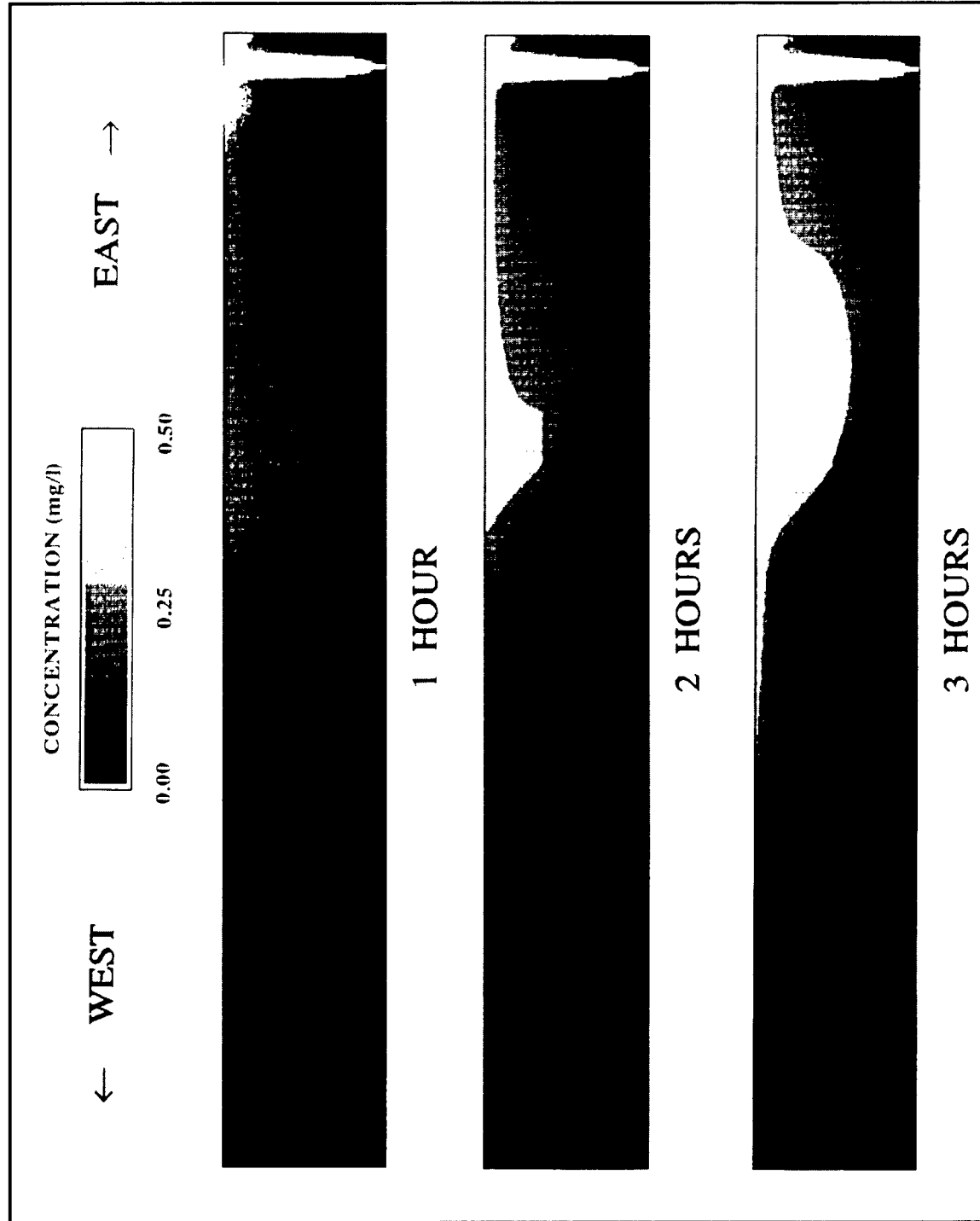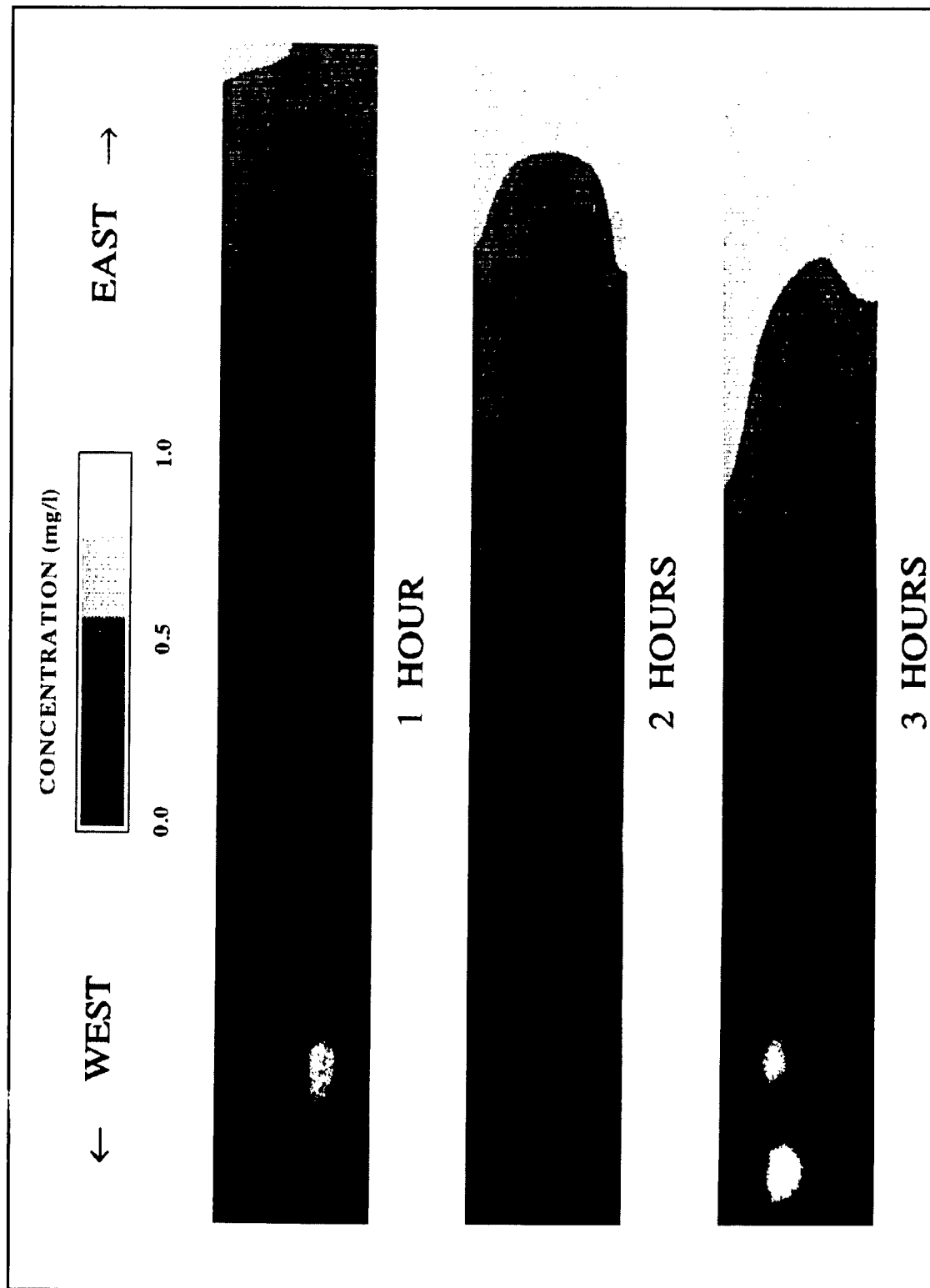
Figure 40.   Predicted concentration of dissolved oxygen in east-west plane of symmetry for two diffusers, 15 ft apart, in Egan Quarry with initial condition assumed anaerobic
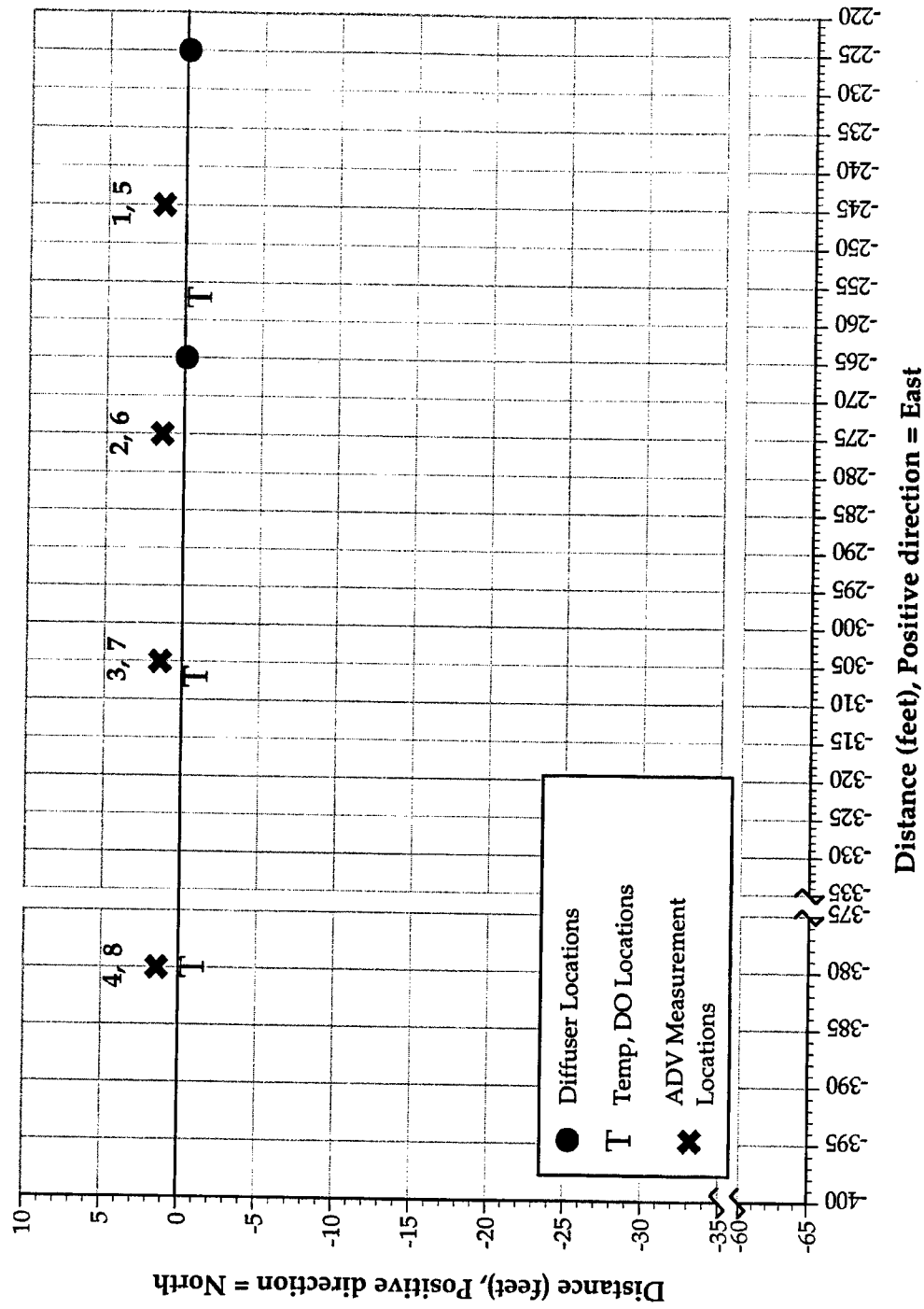
Figure 41.   Experimental data stations for two-diffuser field test, 40-ft spacing, Egan Quarry
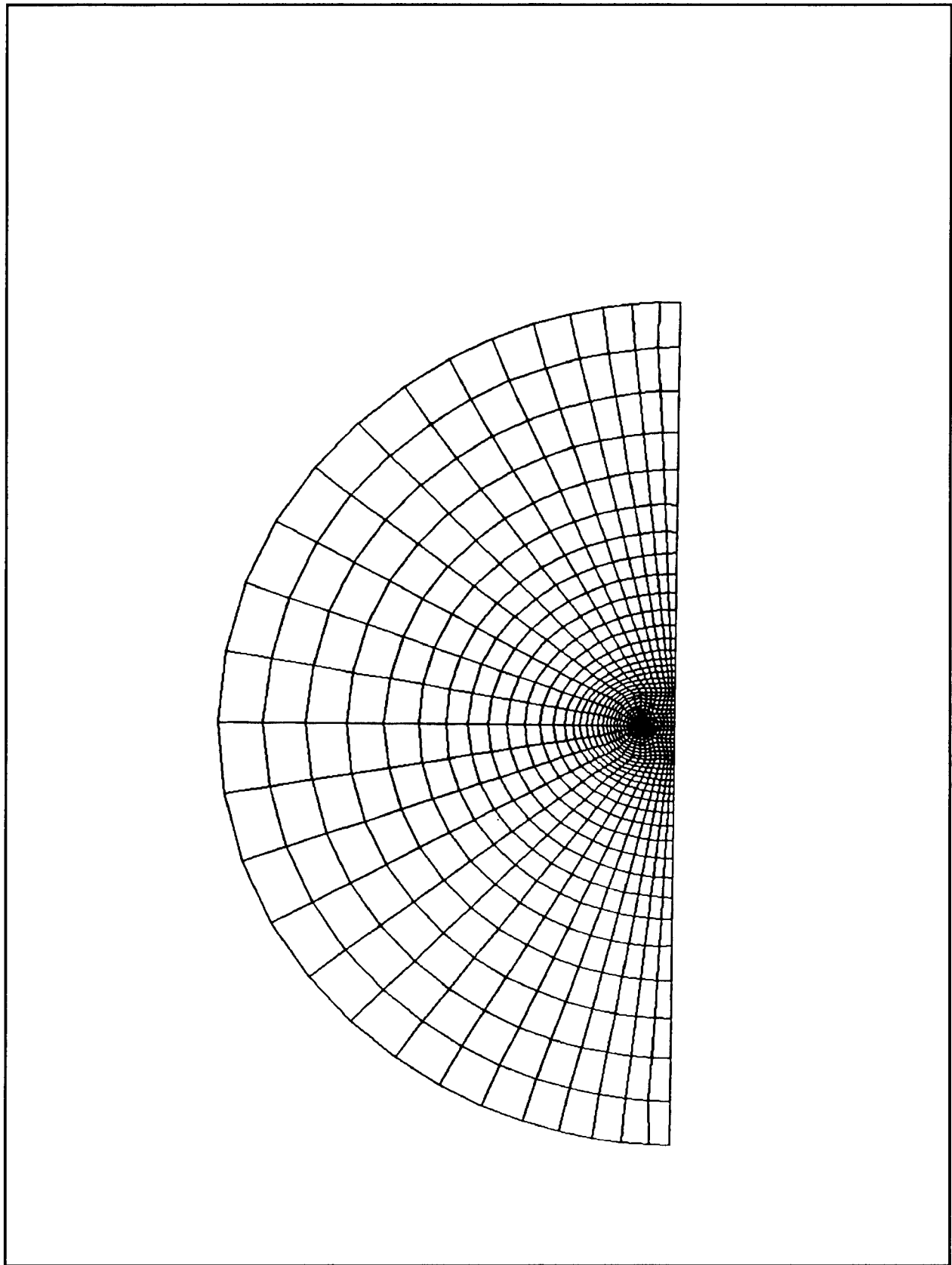
Figure 42.   Half-plane computational grid for two-diffuser simulation, 40-ft spacing, Egan Quarry
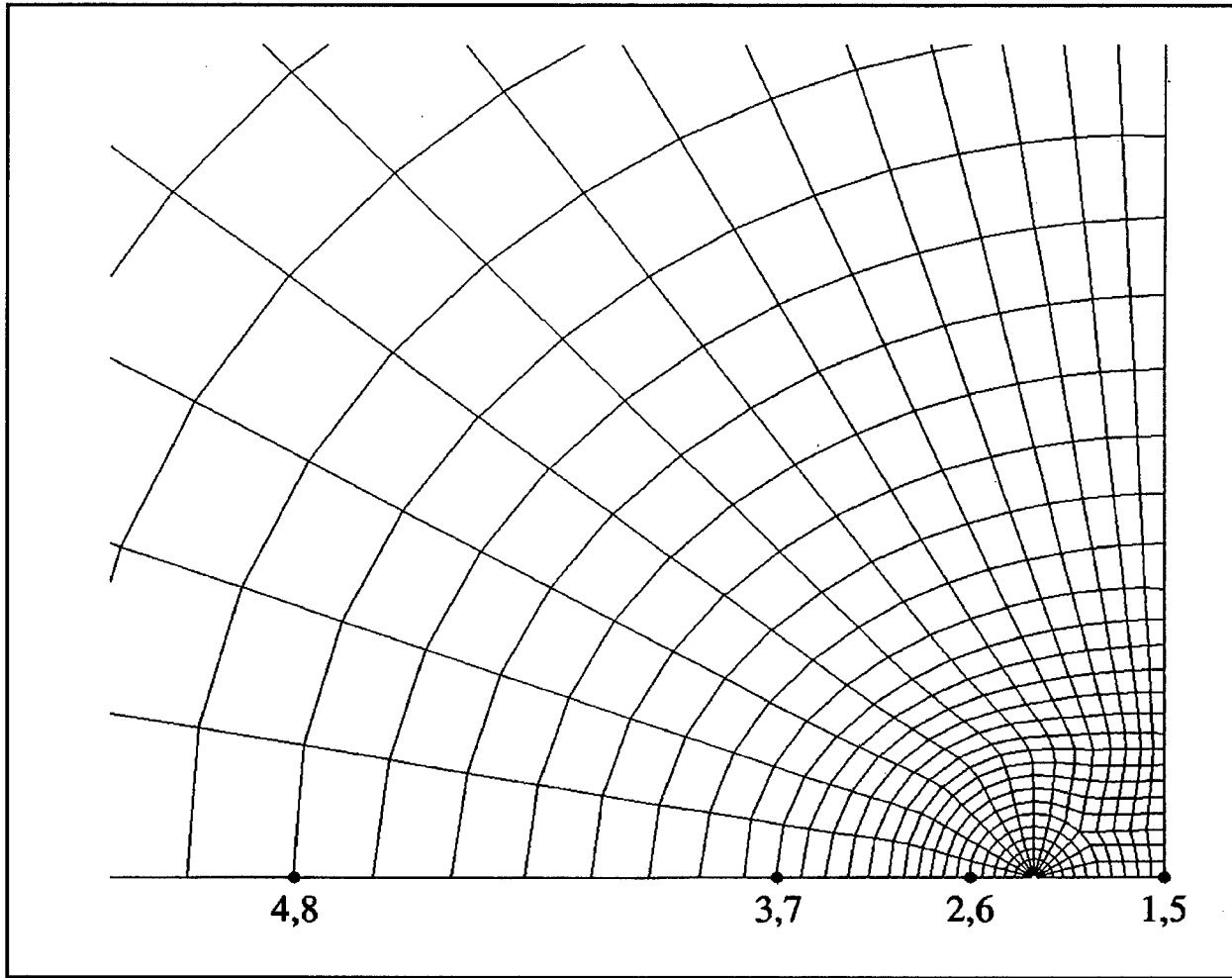
Figure 43.   Grid detail with computational data stations for two-diffuser simulation, 40-ft spacing
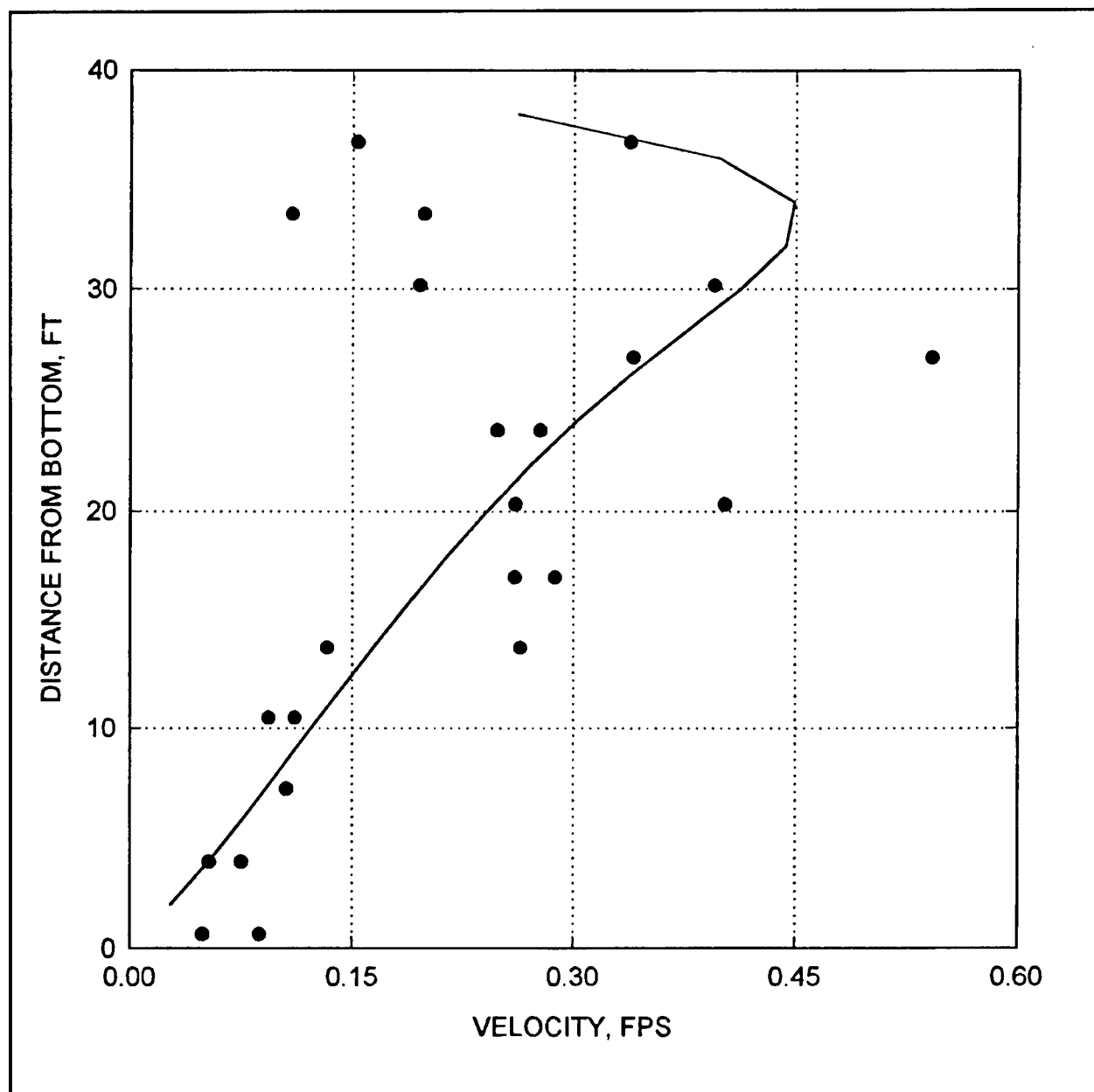
Figure 44. Predicted velocity magnitude (—) and 46-scfm experimental data (●) for two-diffuser test with 40-ft spacing, Egan Quarry, Stations 1, 5
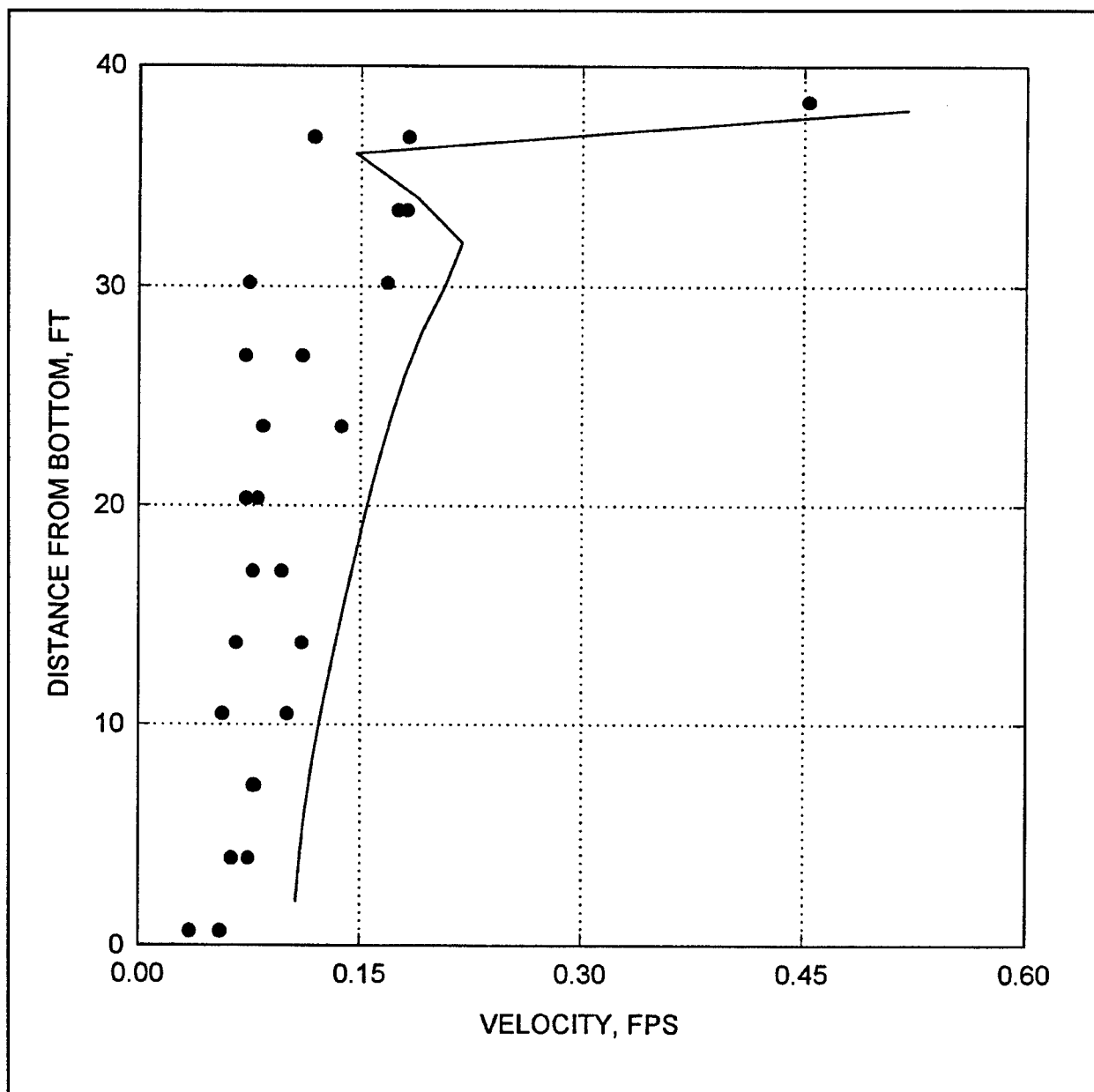
Figure 45.   Predicted velocity magnitude (—) and 46-scfm experimental data (●) for two-diffuser test with 40-ft spacing, Egan Quarry, Stations 2, 6
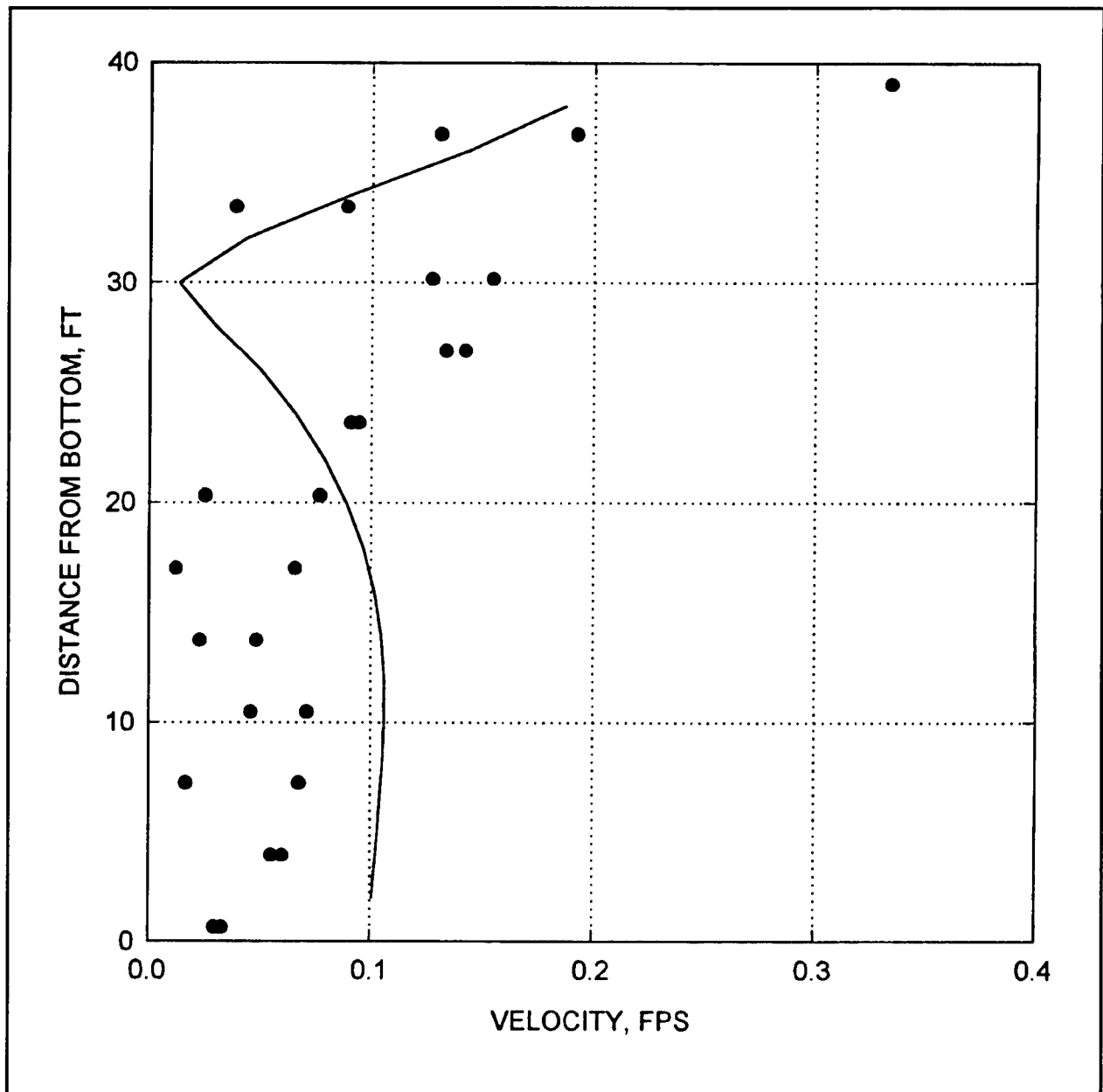
Figure 46. Predicted velocity magnitude (—) and 46-scfm experimental data (●) for two-diffuser test with 40-ft spacing, Egan Quarry, Stations 3, 7
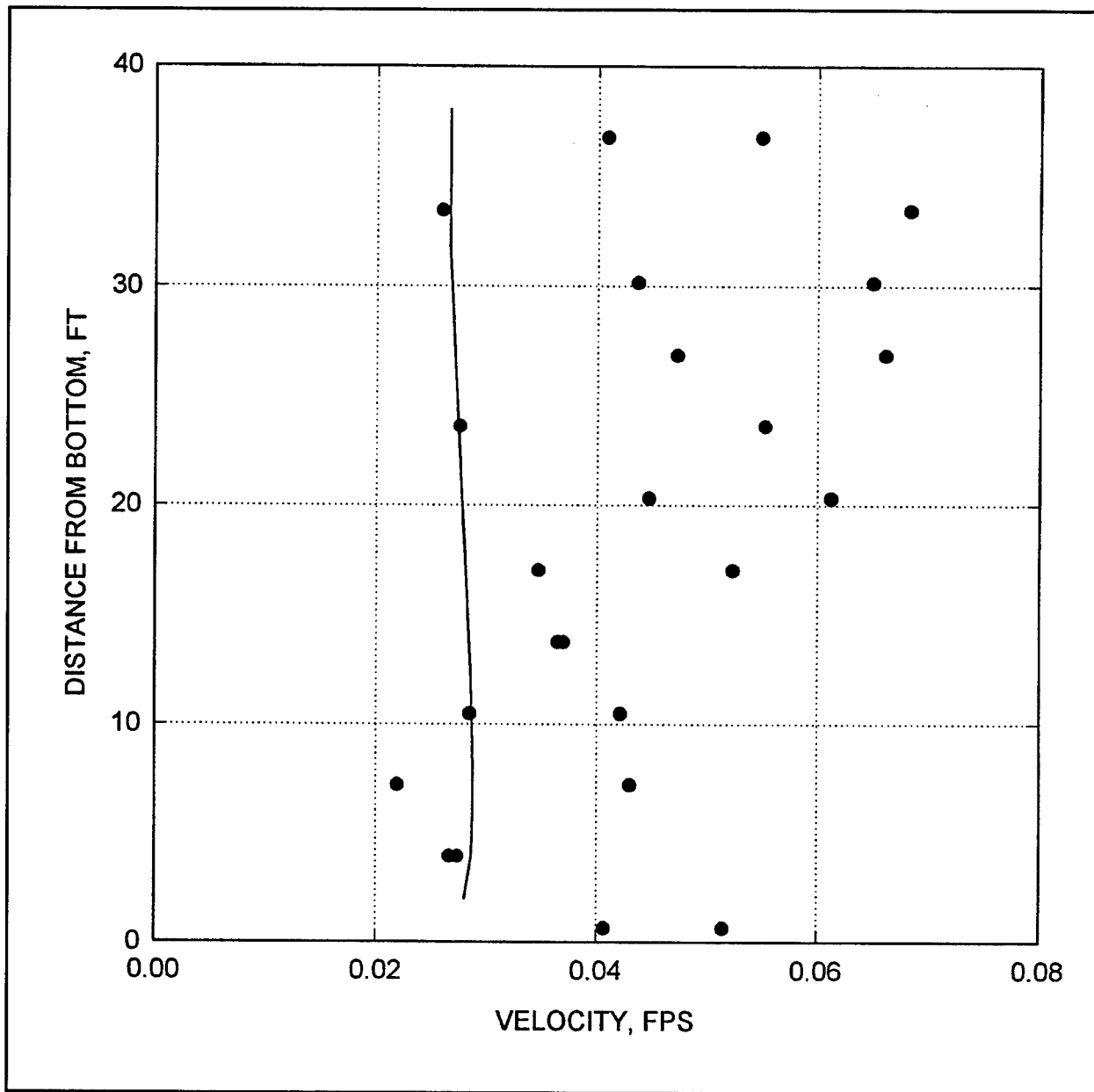
Figure 47.   Predicted velocity magnitude (—) and 46-scfm experimental data (●) for two-diffuser test with 40-ft spacing, Egan Quarry, Stations 4, 8

Figure 48. Background velocity magnitude (●) for two-diffuser test, 40-ft spacing (no airflow)
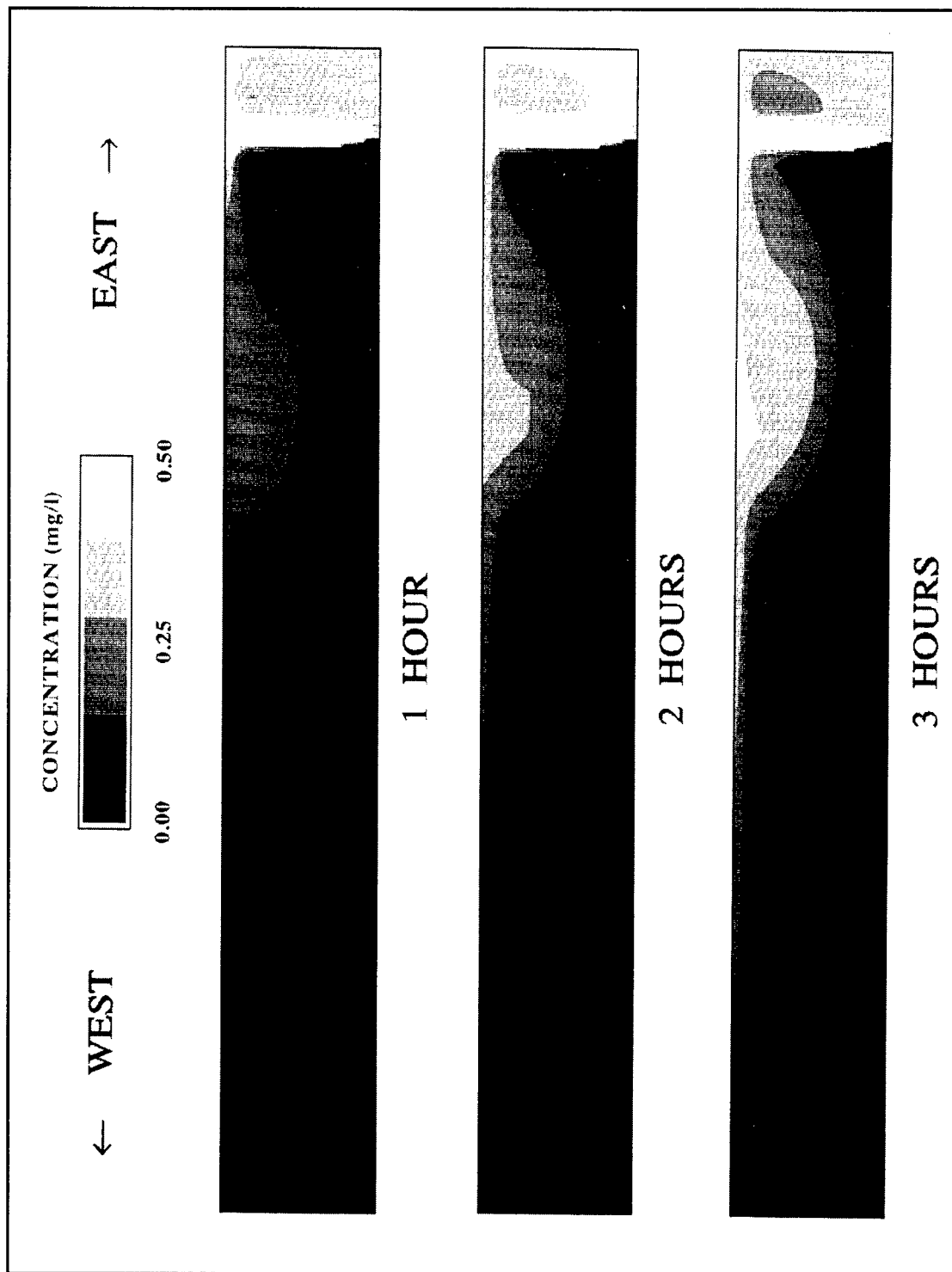
Figure 49.   Predicted concentration of dissolved oxygen in east-west plane of symmetry for two diffusers, 40 ft apart, in Egan Quarry with initial condition assumed anaerobic

Figure 50. Experimental data stations for four-diffuser field test, Egan Quarry

Figure 51. Quarter-plane computational grid for four-diffuser simulation, Egan Quarry
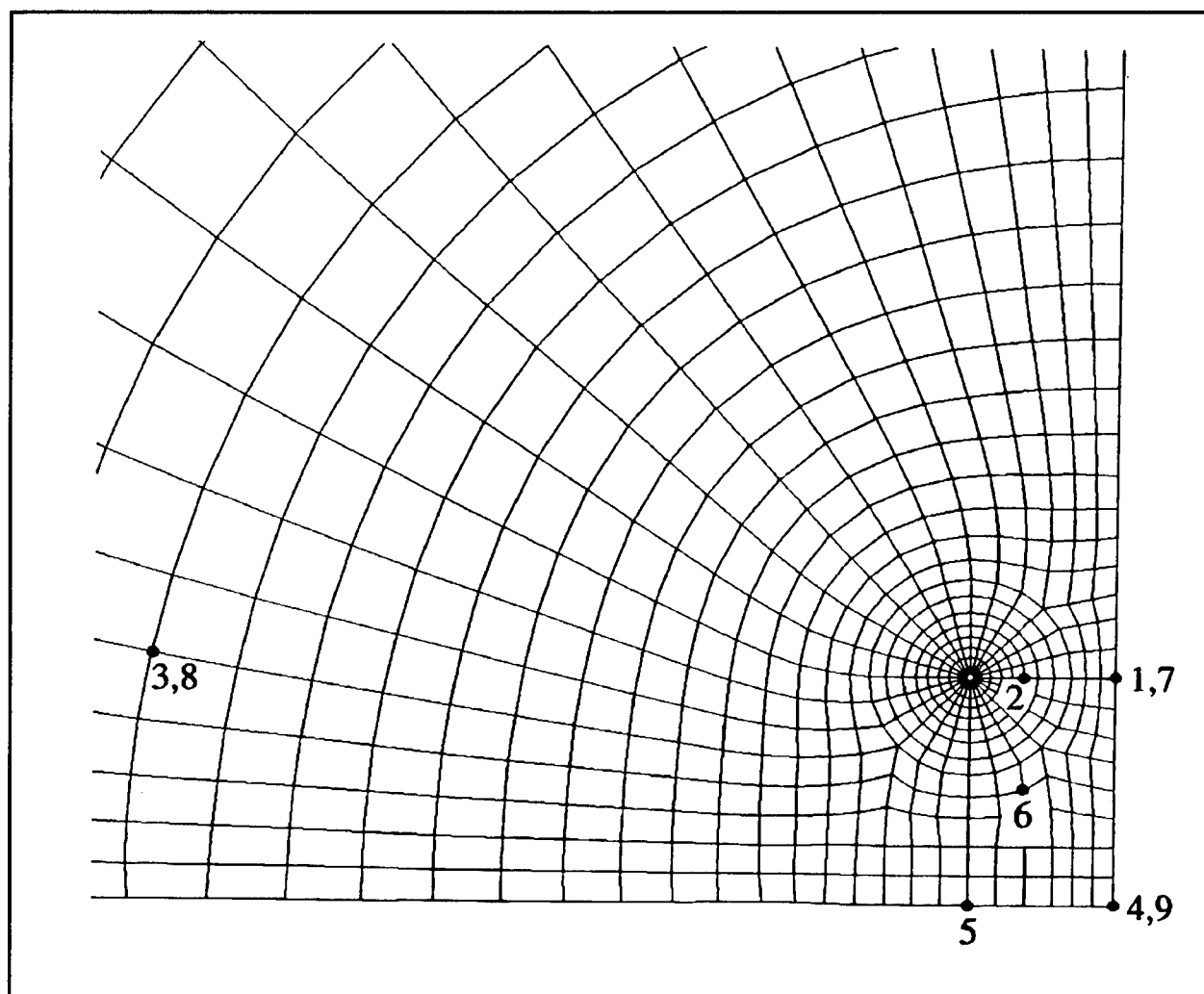
Figure 52. Grid detail with computational data stations for four-diffuser simulation
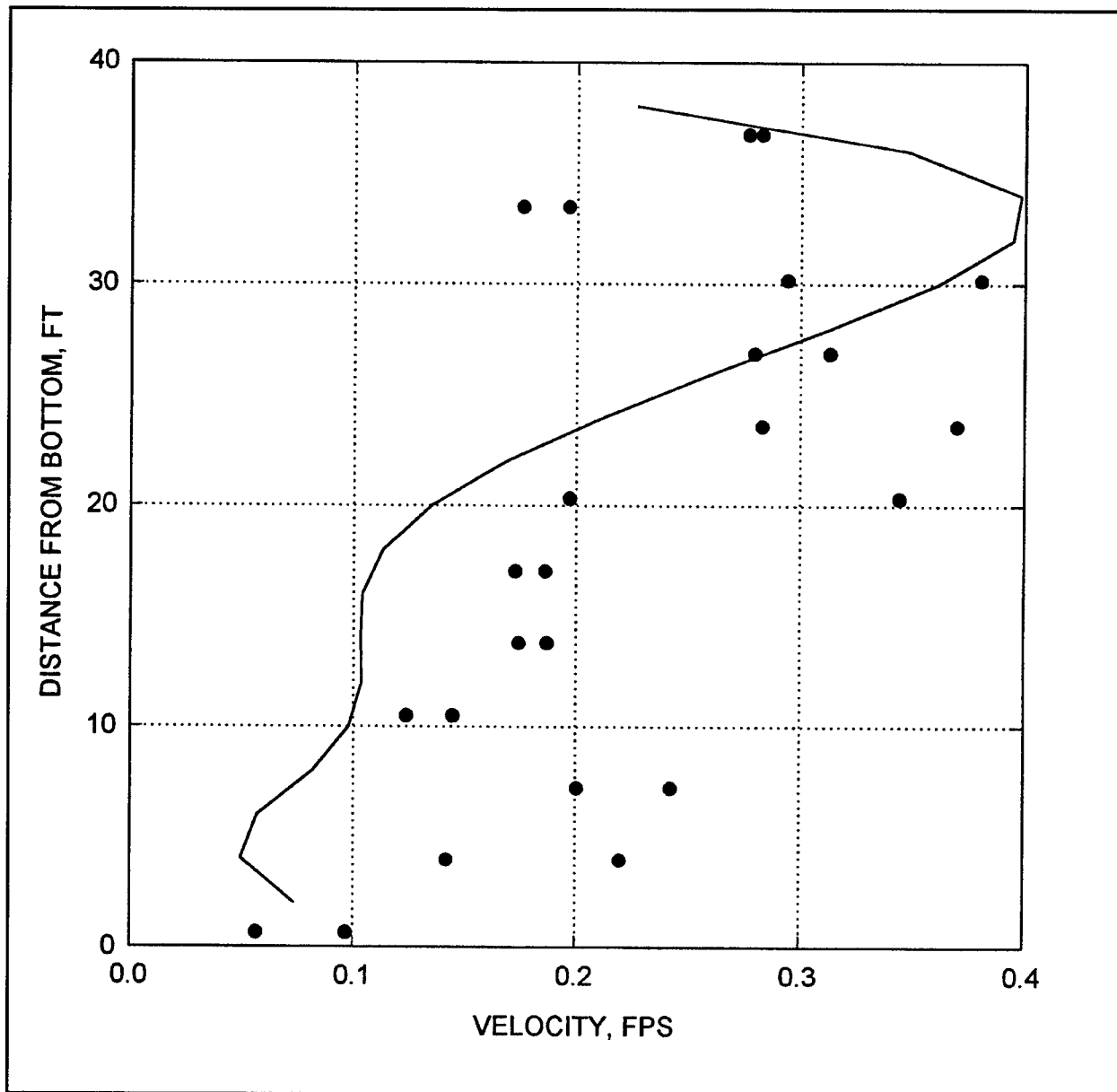
Figure 53. Predicted velocity magnitude (—) and 46-scfm experimental data (●) for four-diffuser test, Egan Quarry, Stations 1, 7

Figure 54. Predicted velocity magnitude (—) and 46-scfm experimental data (●) for four-diffuser test, Egan Quarry, Station 2

Figure 55. Predicted velocity magnitude (—) and 46-scfm experimental data (●) for four-diffuser test, Egan Quarry, Stations 4, 9

Figure 56. Predicted velocity magnitude (—) and 46-scfm experimental data (●) for four-diffuser test, Egan Quarry, Station 5

Figure 57. Predicted velocity magnitude (—) and 46-scfm experimental data (●) for four-diffuser test, Egan Quarry, Station 6

Figure 58. Predicted velocity magnitude (—) and 46-scfm experimental data (●) for four-diffuser test, Egan Quarry, Stations 3, 8

Figure 59. Background velocity magnitude (●) for four-diffuser test (no airflow)

Figure 60. Predicted concentration of dissolved oxygen in east-west plane of symmetry for four diffusers, 40 × 65 ft apart, in Egan Quarry with initial condition assumed anaerobic
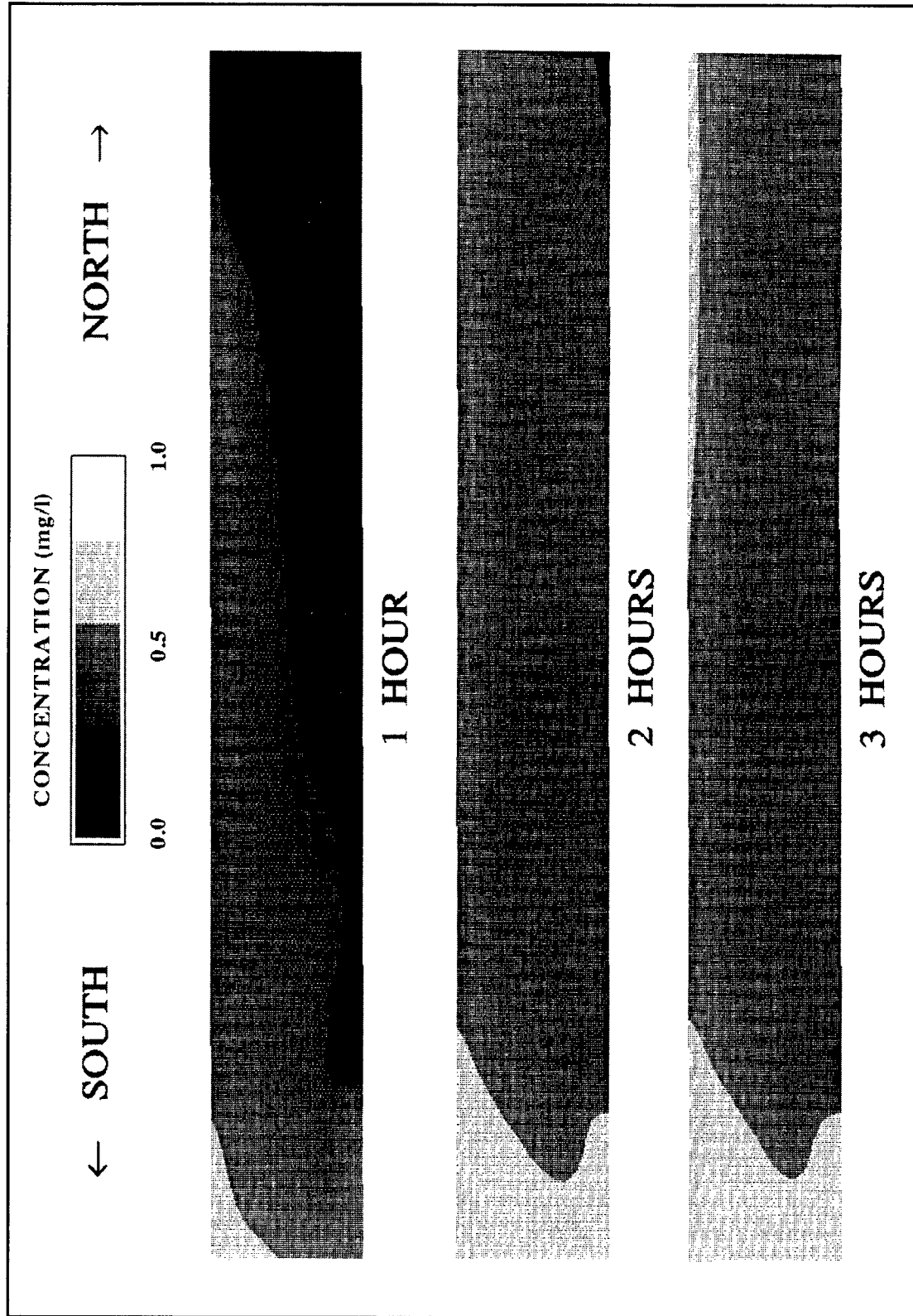
Figure 61. Predicted concentration of dissolved oxygen in north-south plane of symmetry for four diffusers, 40 × 65 ft apart, in Egan Quarry with initial condition assumed anaerobic
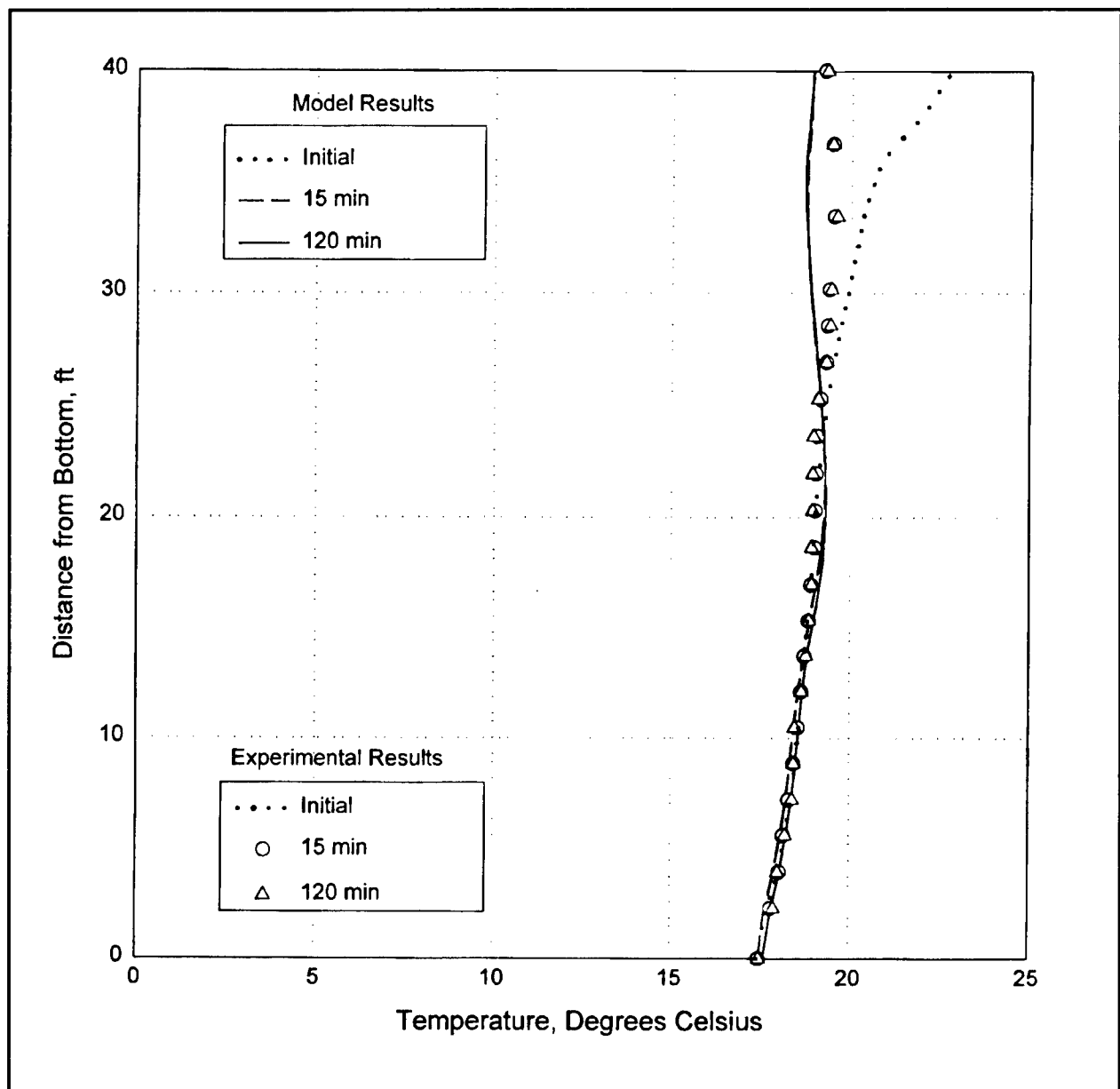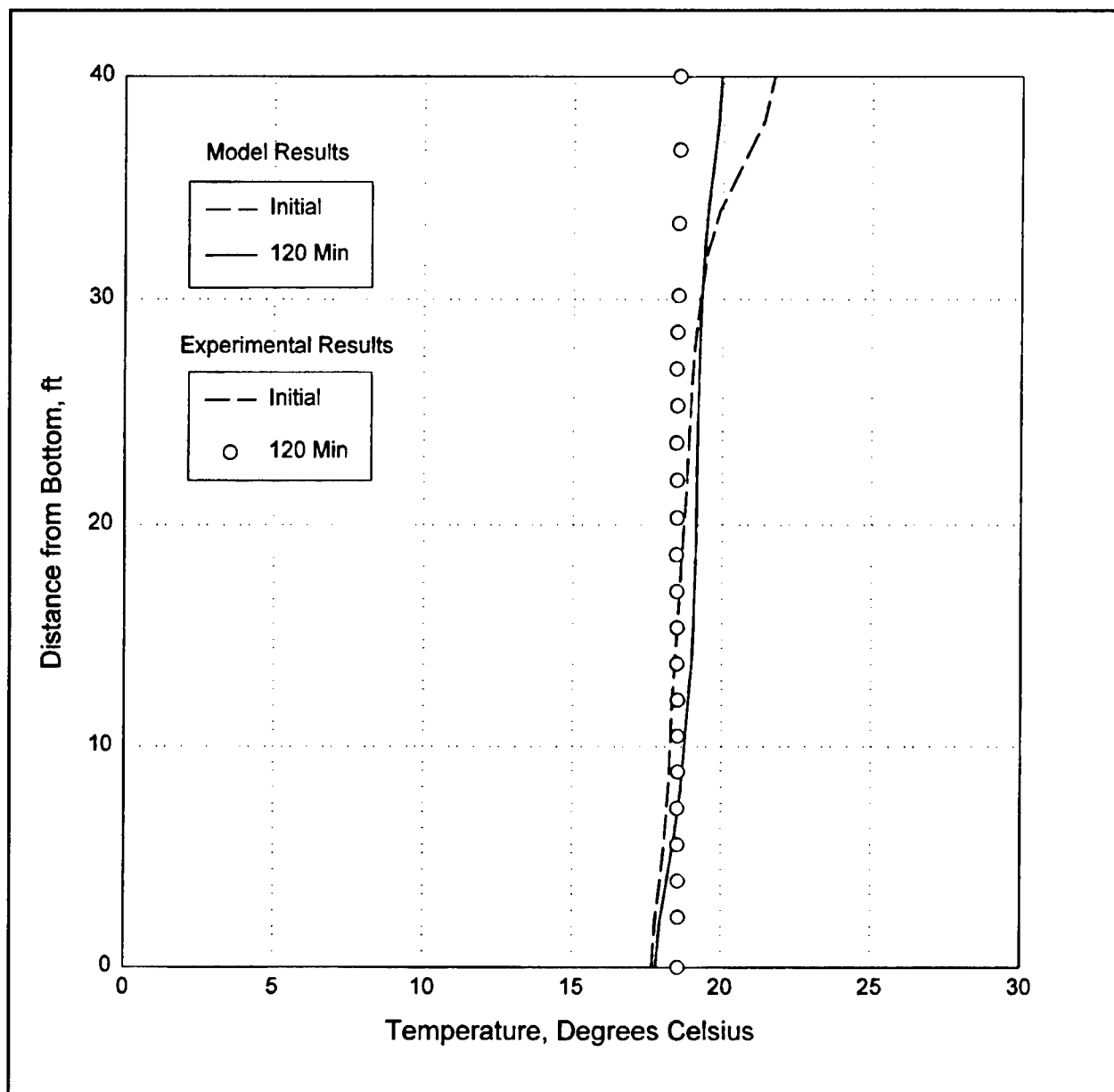
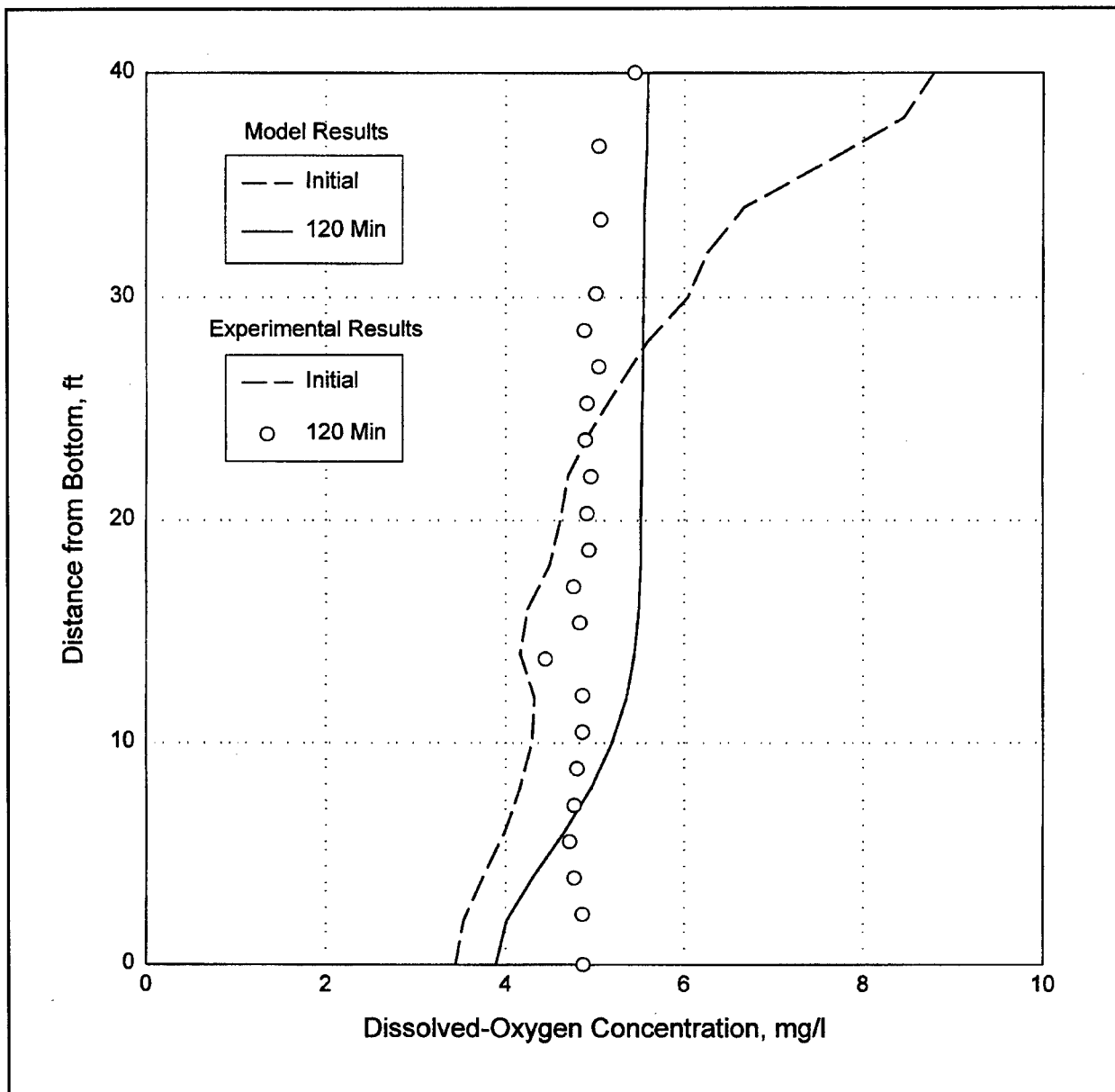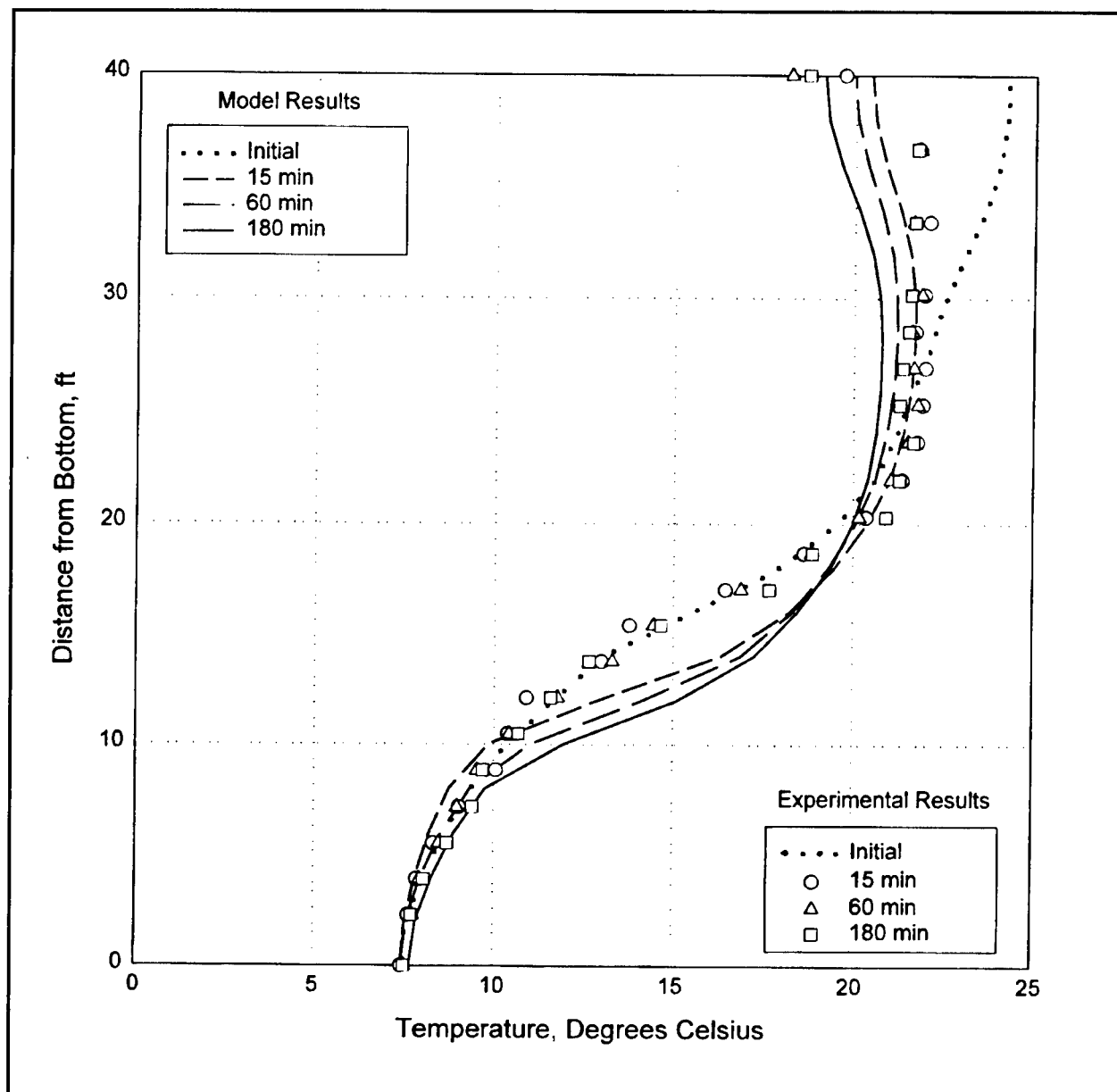Figure 62. Comparison of temperatures, 10 ft from single diffuser, in Egan Quarry with weak initial stratification
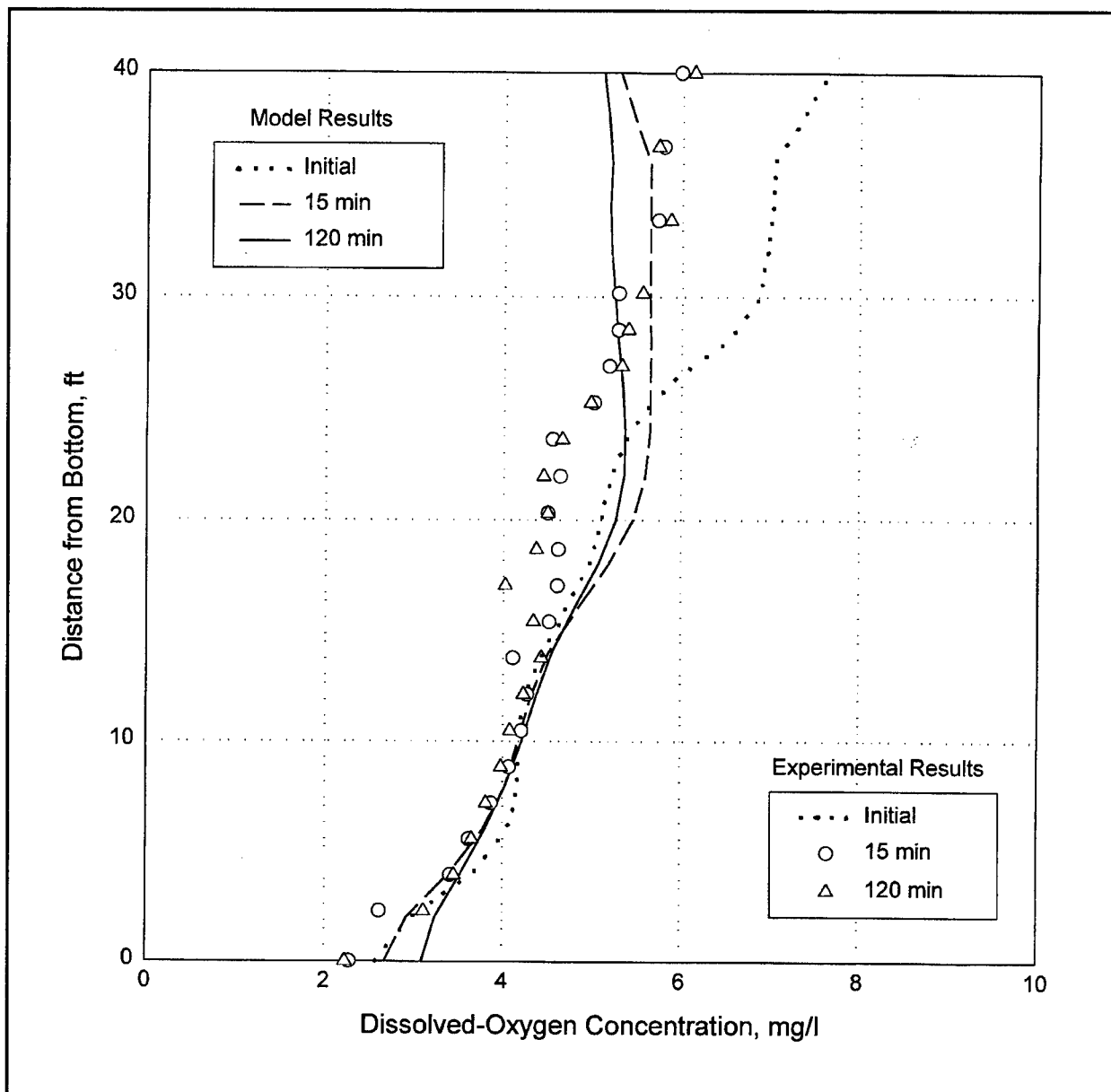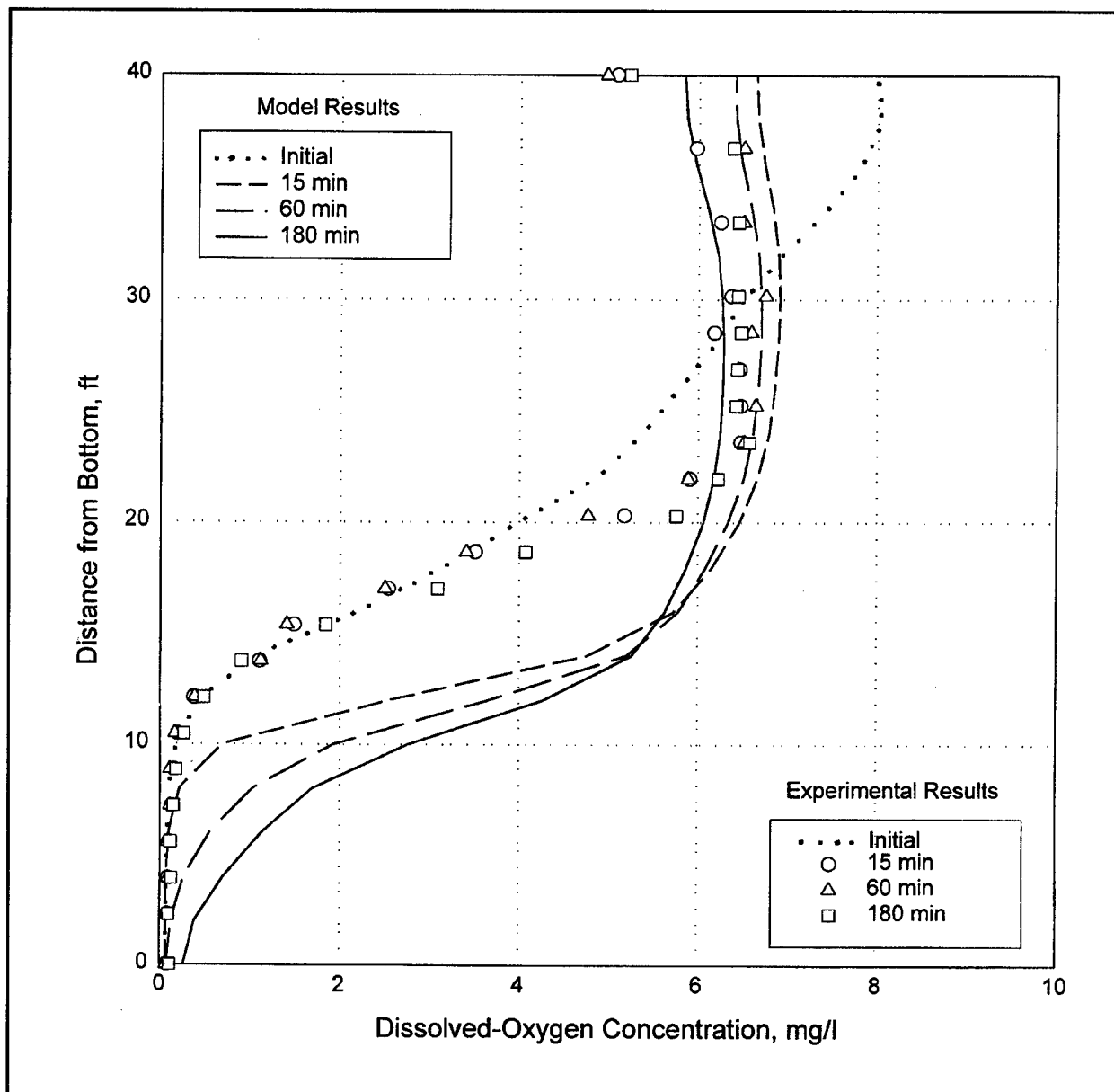
Figure 63. Comparison of dissolved-oxygen concentrations, 10 ft from single diffuser, in Egan Quarry with weak initial stratification
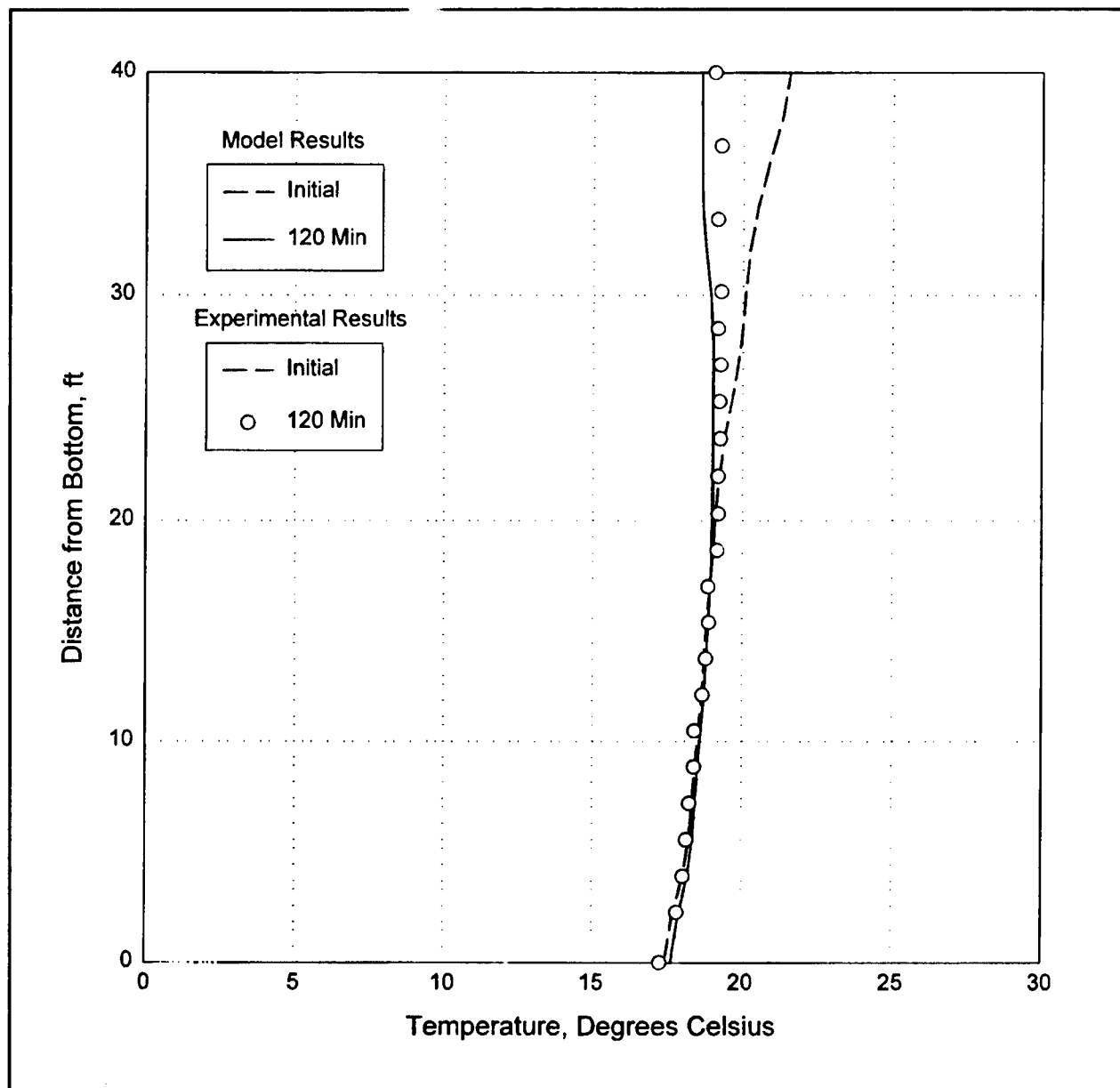
Figure 64. Comparison of temperatures halfway between two diffusers (set 15 ft apart) in Egan Quarry with weak initial stratification
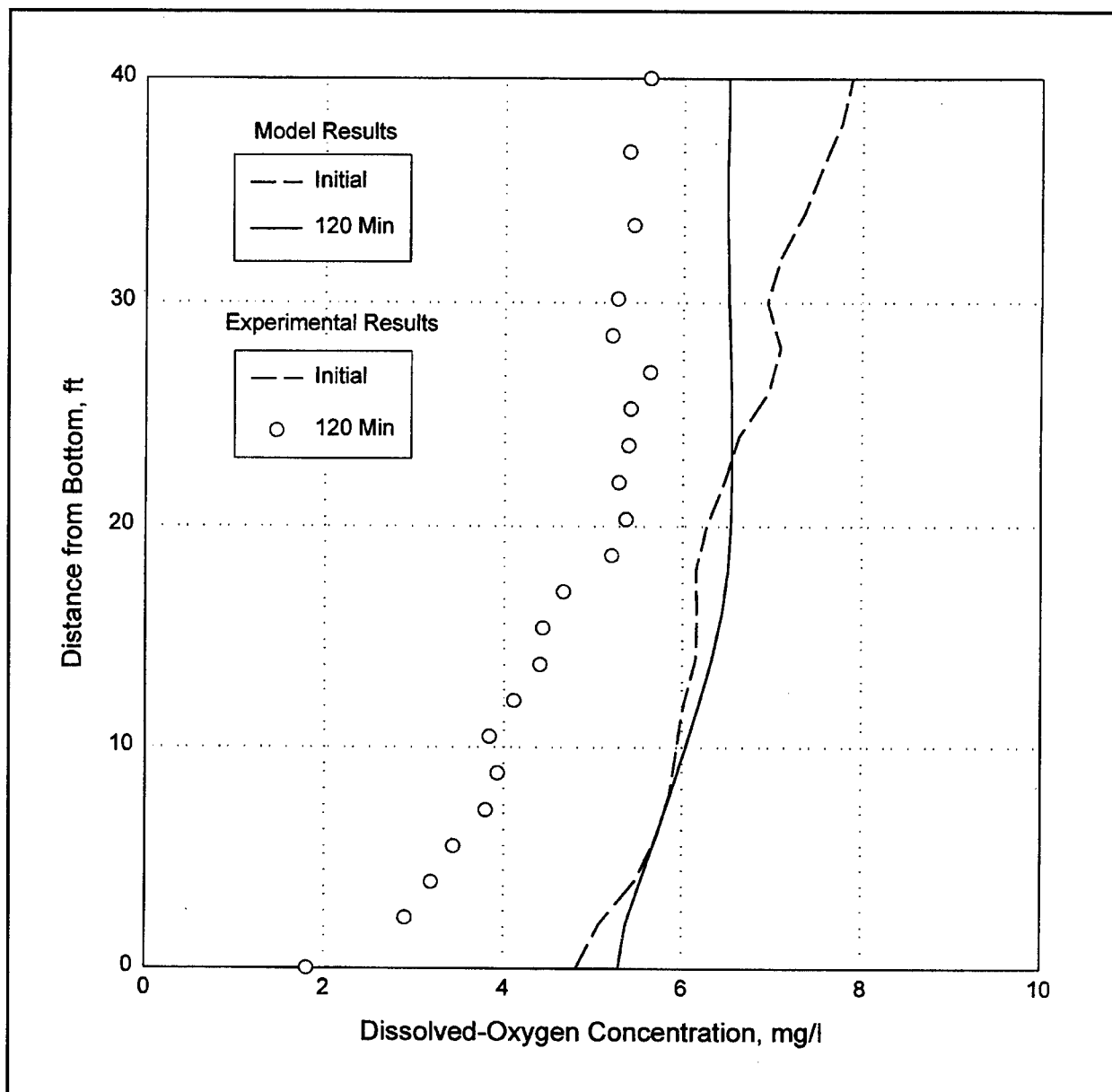
Figure 65. Comparison of dissolved-oxygen concentrations halfway between two diffusers (set 15 ft apart) in Egan Quarry with weak initial stratification
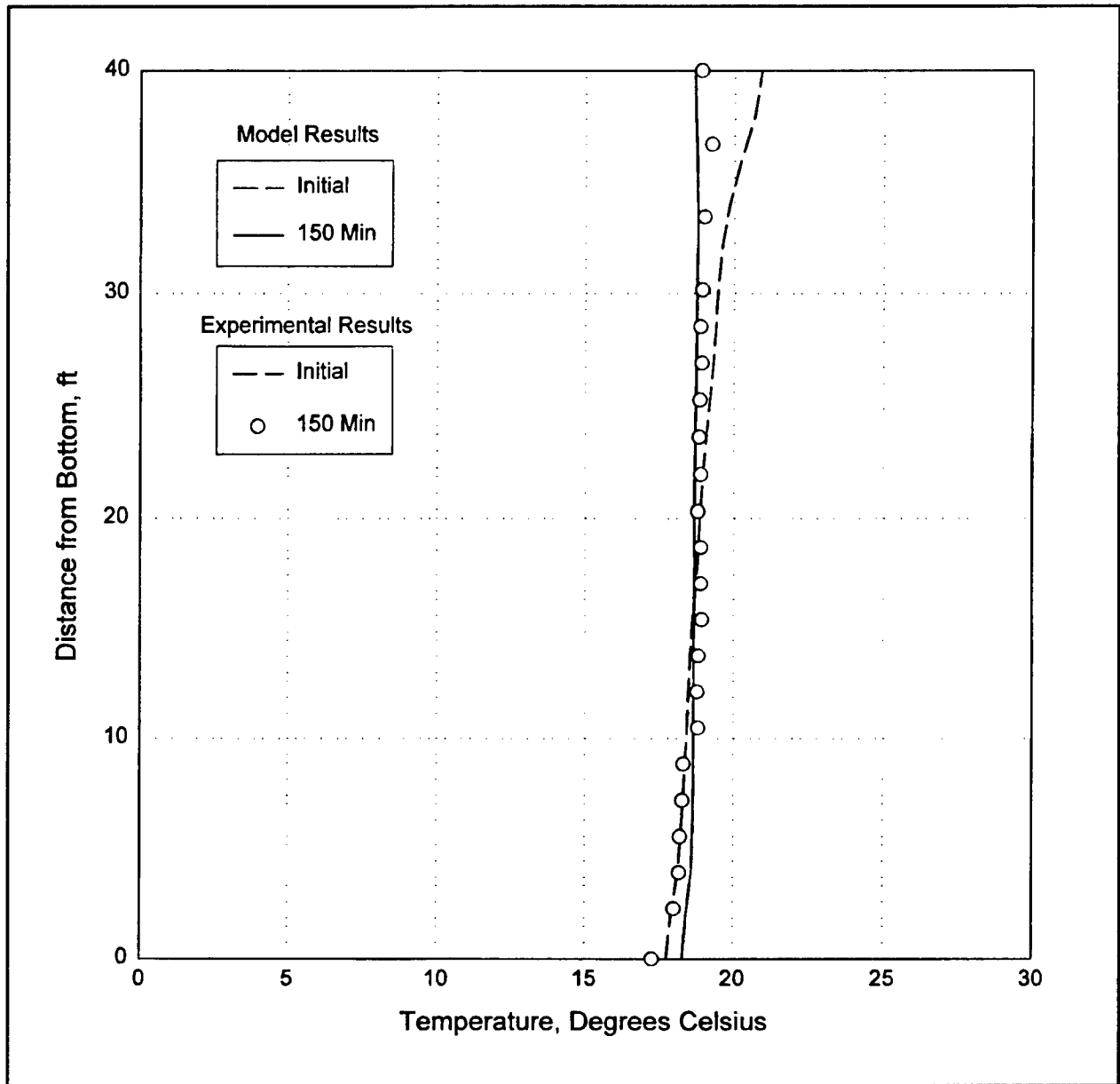
Figure 66. Comparison of temperatures, 10 ft east of west diffuser, for two diffusers (set 40 ft apart) in Egan Quarry with weak initial stratification
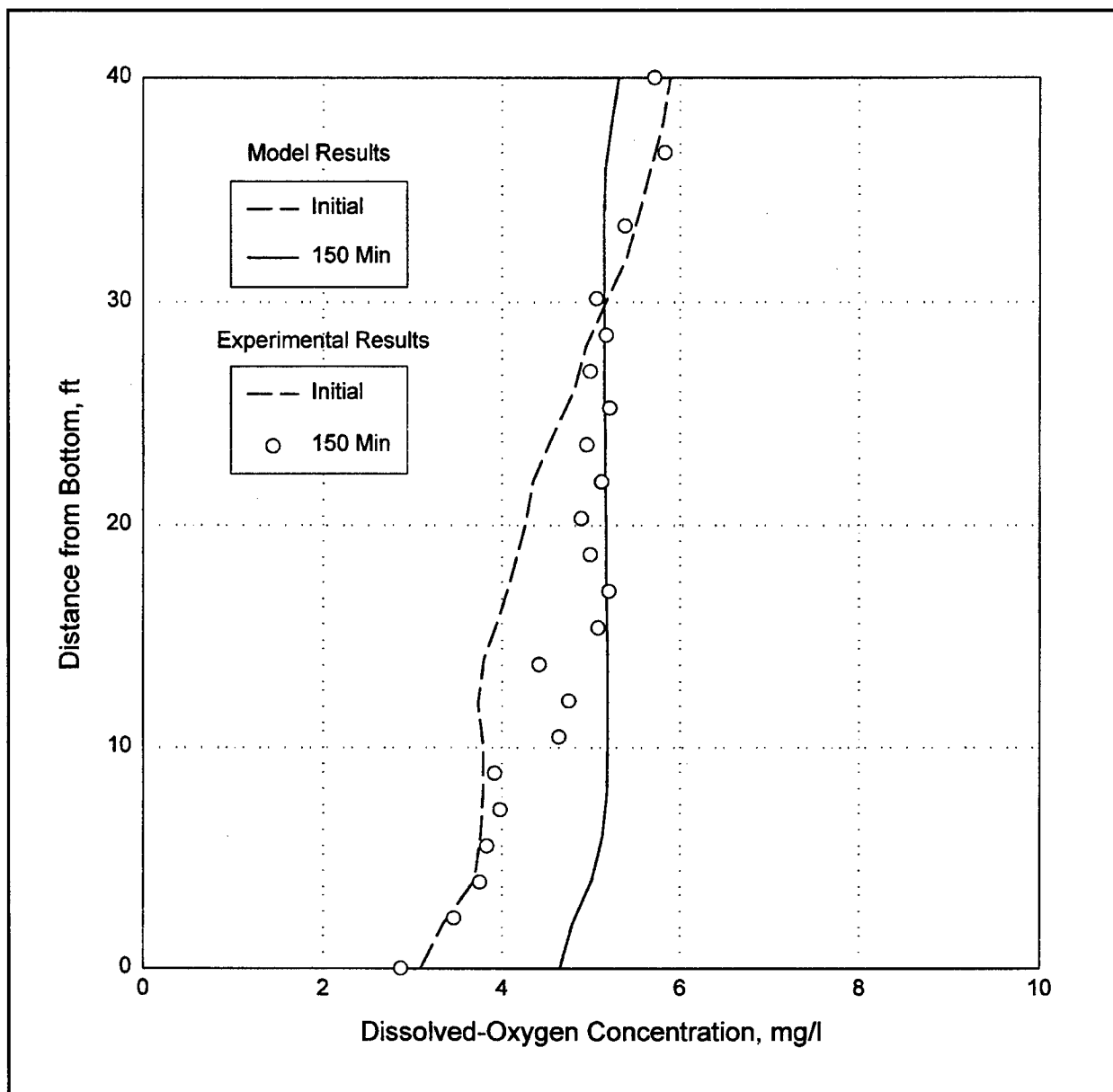
Figure 67. Comparison of dissolved-oxygen concentrations, 10 ft east of west diffuser, for two diffusers (set 40 ft apart) in Egan Quarry with weak initial stratification

Figure 68. Comparison of temperatures at center of four-diffuser array in Egan Quarry with weak initial stratification

Figure 69. Comparison of dissolved-oxygen concentrations at center of four-diffuser array in Egan Quarry with weak initial stratification

Figure 70. Comparison of temperatures, 10 ft from single diffuser, in Egan Quarry with strong initial stratification

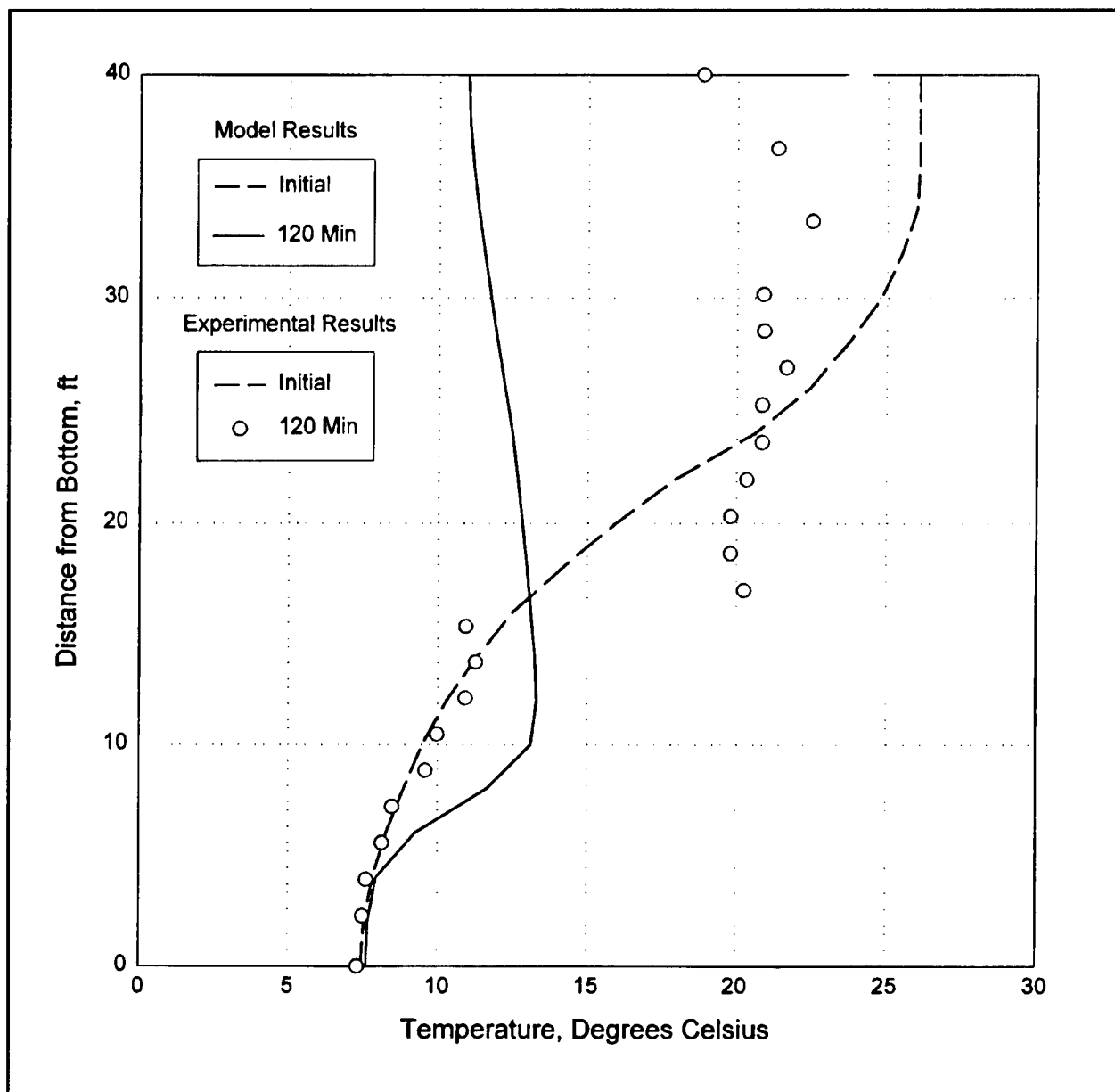Figure 71. Comparison of dissolved-oxygen concentrations, 10 ft from single diffuser, in Egan Quarry with strong initial stratification

Figure 72. Comparison of temperatures halfway between two diffusers (set 15 ft apart) in Egan Quarry with strong initial stratification
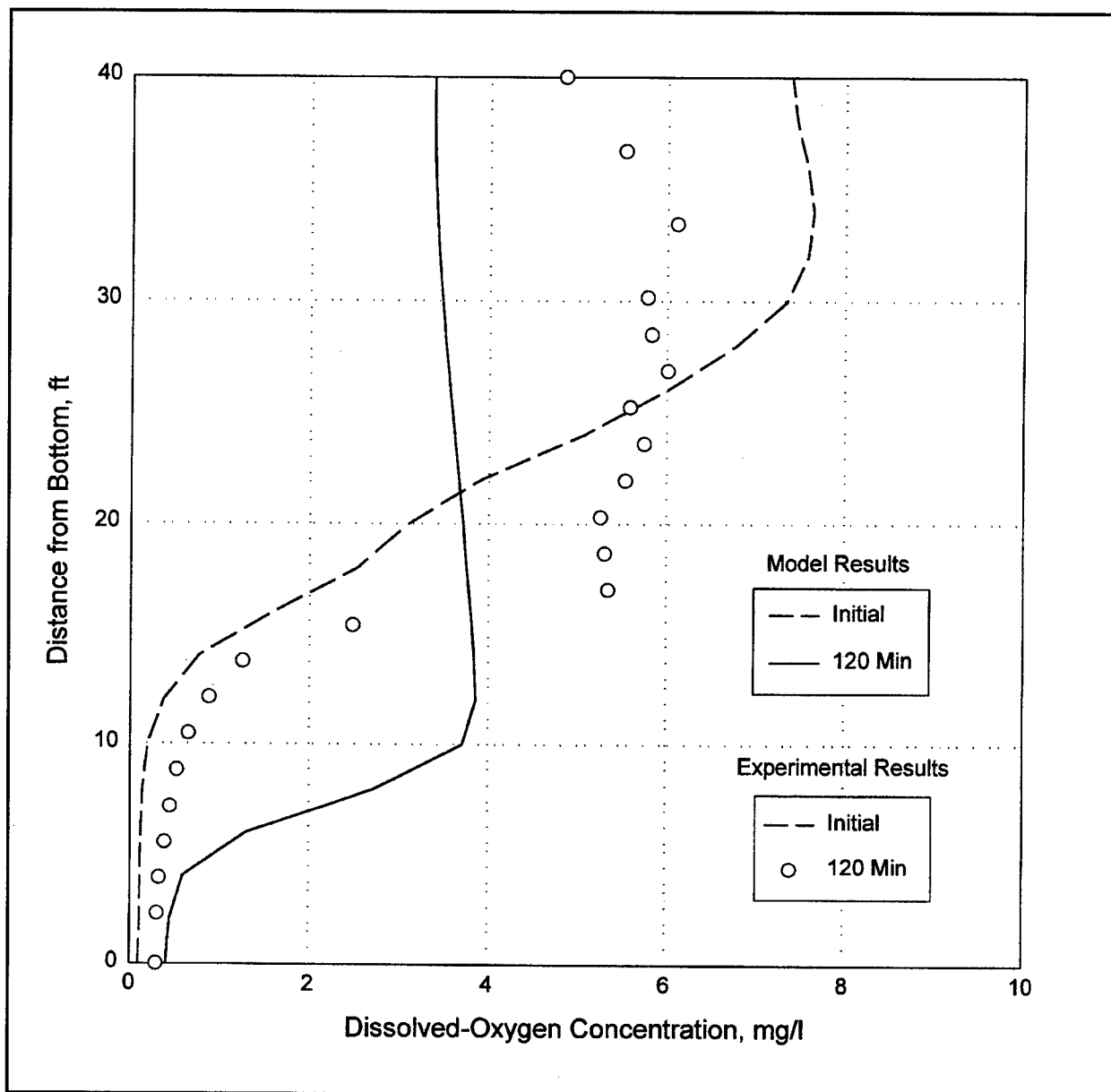
Figure 73. Comparison of dissolved-oxygen concentrations halfway between two diffusers (set 15 ft apart) in Egan Quarry with strong initial stratification
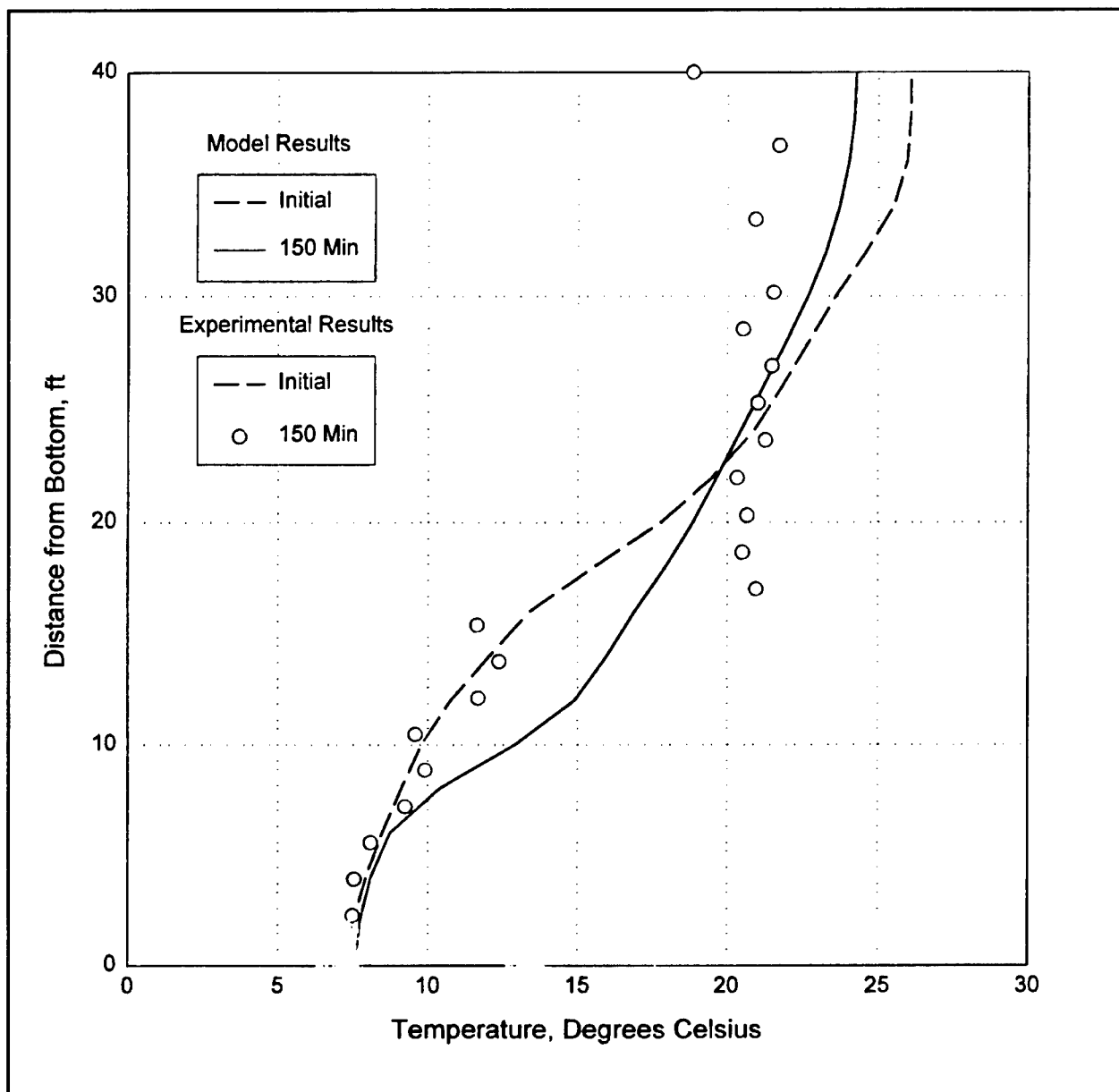
Figure 74. Comparison of temperatures, 10 ft east of west diffuser, for two diffusers (set 40 ft apart) in Egan Quarry with strong initial stratification
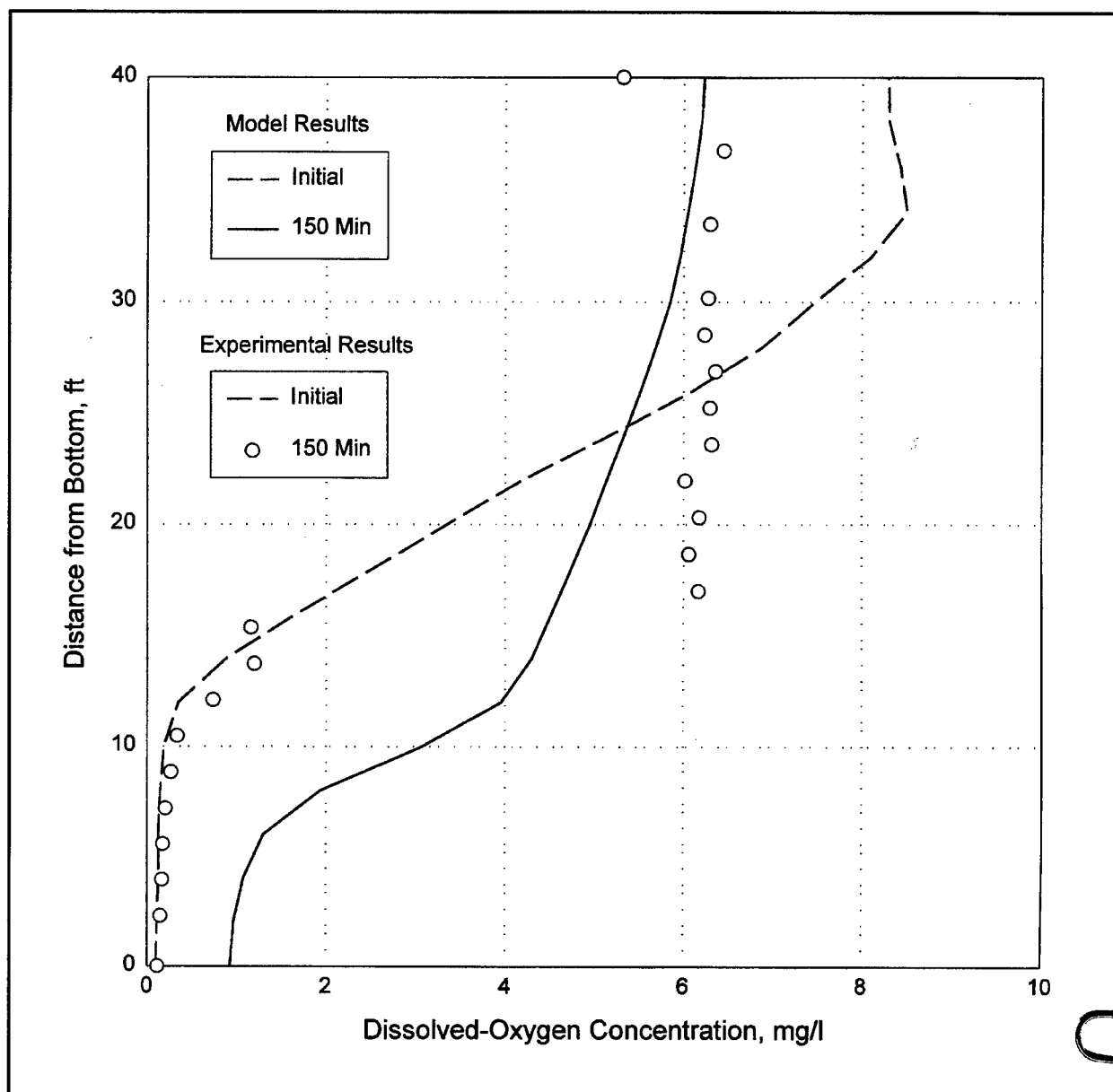
Figure 75. Comparison of dissolved-oxygen concentrations, 10 ft east of west diffuser, for two diffusers (set 40 ft apart) in Egan Quarry with strong initial stratification
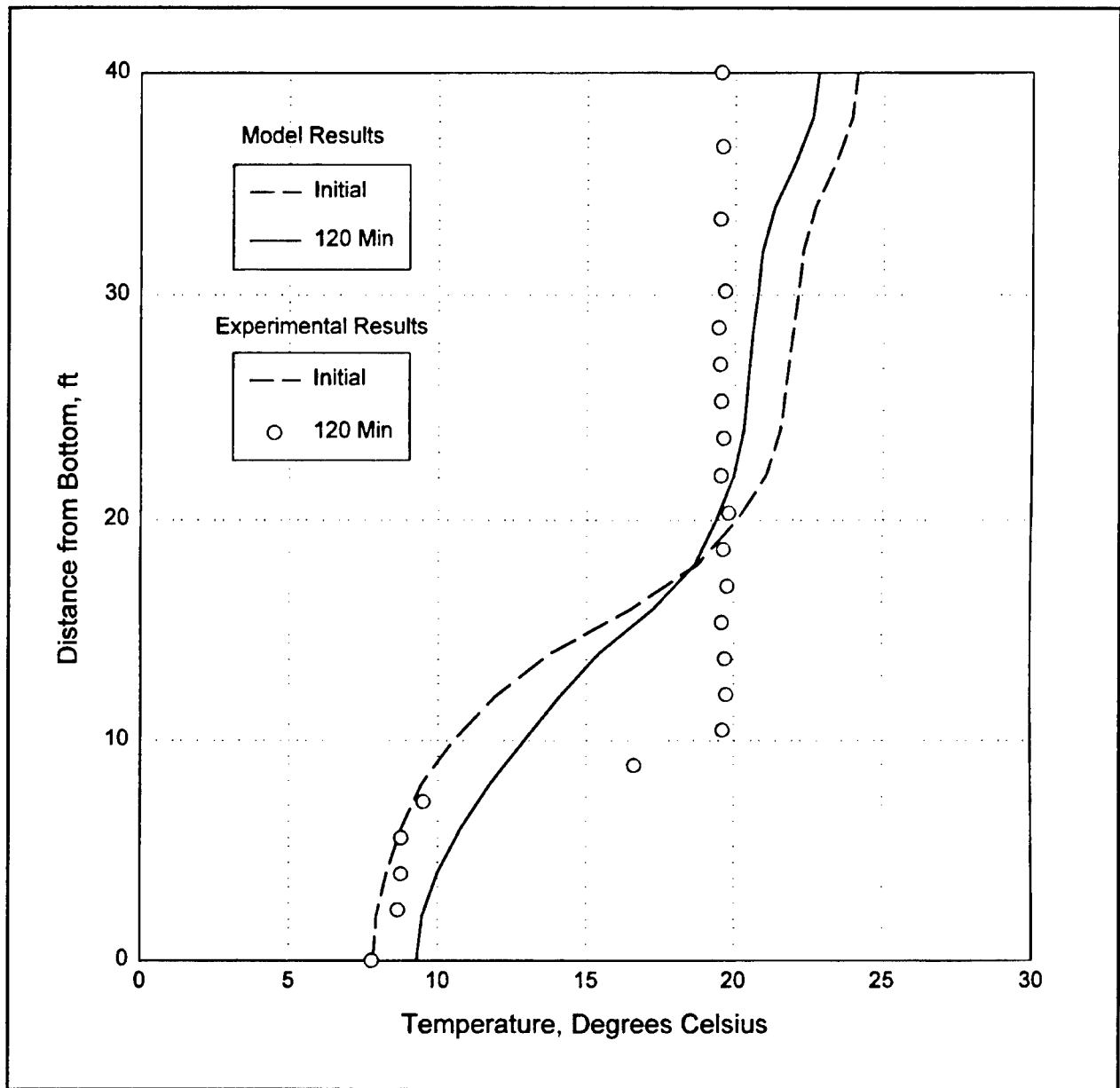
Figure 76. Comparison of temperatures at center of four-diffuser array in Egan Quarry with strong initial stratification
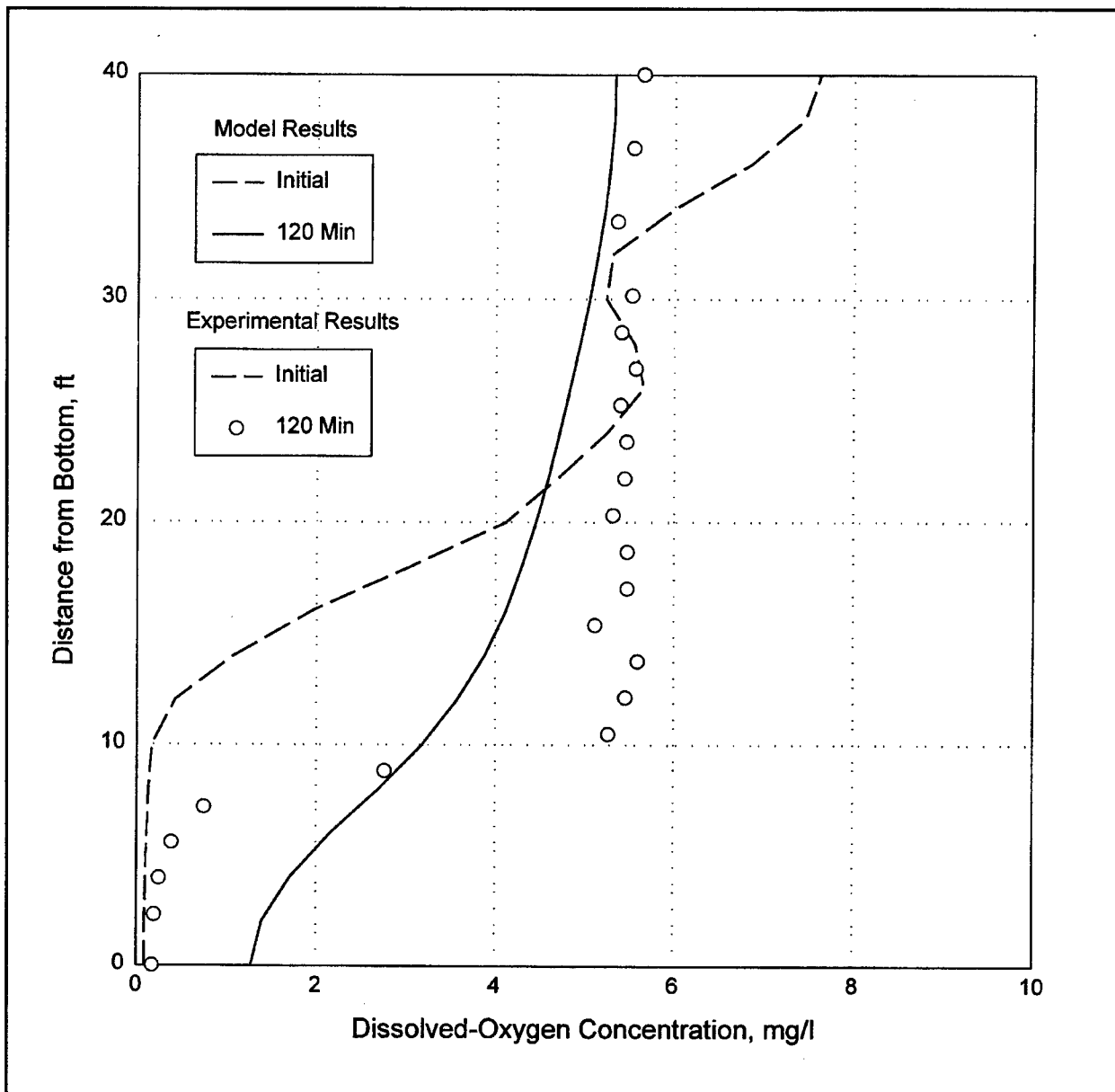
Figure 77. Comparison of dissolved-oxygen concentrations at center of four-diffuser array in Egan Quarry with strong initial stratification

REPORT DOCUMENTATION PAGE

Form Approved
OMB No. 0704-0188

1. AGENCY USE ONLY *(Leave blank)*	2. REPORT DATE July 1998	3. REPORT TYPE AND DATES COVERED Final report

4. TITLE AND SUBTITLE
MAC3D: Numerical Model for Reservoir Hydrodynamics with Application to Bubble Diffusers

5. FUNDING NUMBERS

6 .AUTHOR(S)
Robert S. Bernard

7. PERFORMING ORGANIZATION NAME(S) AND ADDRESS(ES)
U.S. Army Engineer Waterways Experiment Station
3909 Halls Ferry Road, Vicksburg, MS 39180-6199

8. PERFORMING ORGANIZATION REPORT NUMBER
Technical Report CHL-98-23

9. SPONSORING/MONITORING AGENCY NAME(S) AND ADDRESS(ES)
U.S. Army Engineer District, Chicago
111 North Canal Street, Suite 600
Chicago, IL 60606-7206

10. SPONSORING/MONITORING AGENCY REPORT NUMBER

11. SUPPLEMENTARY NOTES
Available from National Technical Information Service, 5285 Port Royal Road, Springfield, VA 22161.

12a. DISTRIBUTION/AVAILABILITY STATEMENT
Approved for public release; distribution is unlimited.

12b. DISTRIBUTION CODE

13. ABSTRACT *(Maximum 200 words)*

The MAC3D numerical model, a three-dimensional flow solver initially developed for reservoir hydrodynamics, has been extended to account for the flow and gas transfer induced by bubble plumes. The latter are represented as buoyant columns in which dissolved gas is transferred to or from surrounding water. The local transfer rate is proportional to the dissolved gas concentration, and the resulting flow and gas transport are computed by solving discrete equations for the conservation of mass and momentum. The upward force imposed by a bubble column is directly proportional to the airflow rate through the associated bubble diffuser, and inversely proportional to the local depth and the bubble rise velocity. Gas-transfer coefficients are empirical quantities that have to be inferred from laboratory experiments, but eddy viscosity and diffusivity are obtained directly from a k-$\in$ turbulence model. In the numerical solution of the governing equations, the (previously used) explicit MacCormack scheme has been replaced by an implicit upwind scheme that improves stability and reduces execution time by a factor of five to ten. In this report, the model is validated for unstratified or weakly stratified water bodies by comparing predicted velocities and gas-transfer rates with data from laboratory experiments and field tests using coarse- and fine-bubble diffusers.

14. SUBJECT TERMS

Bubble plumes	Incompressible flow
Computational fluid dynamics	Turbulence model
Gas transfer	

15. NUMBER OF PAGES
112

16. PRICE CODE

17. SECURITY CLASSIFICATION OF REPORT UNCLASSIFIED	18. SECURITY CLASSIFICATION OF THIS PAGE UNCLASSIFIED	19. SECURITY CLASSIFICATION OF ABSTRACT	20. LIMITATION OF ABSTRACT